BRNO UNIVERSITY OF TECHNOLOGY

VYSOKÉ UČENÍ TECHNICKÉ V BRNĚ

FACULTY OF MECHANICAL ENGINEERING

FAKULTA STROJNÍHO INŽENÝRSTVÍ

INSTITUTE OF SOLID MECHANICS, MECHATRONICS AND BIOMECHANICS

ÚSTAV MECHANIKY TĚLES, MECHATRONIKY A BIOMECHANIKY

COMPUTATIONAL SIMULATION OF PASS ROLLING

VÝPOČTOVÁ SIMULACE VÁLCOVÁNÍ V KALIBRU

MASTER'S THESIS
DIPLOMOVÁ PRÁCE

AUTHOR   Bc. Samuel Hacek
AUTOR PRÁCE

SUPERVISOR   prof. Ing. Jindřich Petruška, CSc.
VEDOUCÍ PRÁCE

BRNO 2020

Specification Master's Thesis

Department: Institute of Solid Mechanics, Mechatronics and Biomechanics

Student: **Bc. Samuel Hacek**

Study programme: Applied Sciences in Engineering

Study branch: Engineering Mechanics and Biomechanics

Supervisor: **prof. Ing. Jindřich Petruška, CSc.**

Academic year: 2019/20

Pursuant to Act no. 111/1998 concerning universities and the BUT study and examination rules, you have been assigned the following topic by the institute director Master's Thesis:

Computational simulation of pass rolling

Concise characteristic of the task:

Design of the right sequence of profiles in pass rolling is a complicated problem, solved traditionally by a combination of industrial experience and simple computationally–experimental procedures. The topic of this thesis is to compare these traditional procedures with modern computational tools and to illustrate it on a selected pass rolling example.

Goals Master's Thesis:

1. Study of traditional methods of pass rolling analysis.
2. Computational simulation of material flow through a selected sequence of passes by a 3D FEM model, including the material and frictional nonlinearity.
3. Comparation of the results with experimental solution.
4. Evaluation of the efficiency and predictive reliability of the modern procedure.

Recommended bibliography:

MACURA, P., PETRUŠKA, J.: Numerical and experimental simulation of pass rolling, J. Mat. Proc. Tech. 60, 1996, 55.

MACURA. P., ELFMARK, J. and STANĚK, P.: Hut. listy, 48, 1993, No. 9,17.

PETRUŠKA, J., MACURA, P.: Pass rolling and material formability - numerical and experimental analysis, Stroj. čas. 48, 1997, 1-12.

HAJDUK, M., KONVIČNÝ, J.: Silové podmínky při válcování oceli za tepla, SNTL Praha, 1983.

Deadline for submission Master's Thesis is given by the Schedule of the Academic year 2019/20

In Brno,

L. S.

....
prof. Ing. Jindřich Petruška, CSc. doc. Ing. Jaroslav Katolický, Ph.D.
Director of the Institute FME dean

Abstract

This master's thesis reviews possibilities of finite element modelling of pass rolling. Motivation and problem formulation may be found at the beginning of the thesis, followed by definition of system of essential variables.

Next chapter describes various methods of rolling as well as the rolling process itself. An emphasis is put mainly on pass roll design. The following part deals with material behavior and its modelling in finite element software Abaqus, which is used in the computational part of the thesis. Multiple models of plasticity are introduced here, as well as damage criteria, used to assess material formability or simulate propagation of ductile damage through the material. Next part is focused on finite element method, specifically its explicit algorithm, later employed in the computational part of the thesis. In the last theoretical chapter, basic principles of photoelasticimetry, a traditional experimental method, are described.

These chapters also contain description of simplified finite element analysis and photoplastic experimental analysis of a specific pass rolling problem. Computational model used there served as a basis for the new finite element model, creation of which is the purpose of the following chapter. Two variants of the simplified, previously used computational model were recreated as well.

Structural analyses were carried out using the three created models and various results were evaluated. Summary of obtained results and their comparison to original computational and experimental results follows. Discussion of the results and evaluation of usability and reliability of individual computational models form conclusion of the thesis.

Keywords

pass rolling, bulk forming, photoelasticimetry, ductile damage, structural analysis, explicit finite element method, Abaqus

Rozšírený abstrakt

Táto diplomová práca sa zaoberá možnosťami výpočtového modelovania valcovania v kalibroch pomocou metódy konečných prvkov a porovnáva moderný výpočtový model so zjednodušeným výpočtovým modelom, použitým v predošlom výskume.

Práca sa začína vyjadrením motivácie pre písanie práce, formuláciou problémovej situácie a súhrnom cieľov, ktoré majú byť v práci dosiahnuté. Nasleduje zostavenie systému podstatných veličín pre úlohu riešenú vo výpočtovej časti práce.

Ďalšia kapitola je venovaná technológii valcovania. Začína opisom rôznych spôsobov valcovania, rozdelených podľa viacerých kritérii a tiež opisuje rôzne druhy polotovarov a vývalkov. Ďalej je rozobratý samotný valcovací proces - trecie sily na rozhraní valcov a prevalku, tok materiálu a jednotlivé časti deformačnej zóny. Nasleduje popis návrhu kalibrov. Ide o komplexný proces, založený na viacerých experimentálnych a analytických procedúrach. Postupne je opísaný výpočet pracovného polomeru, trecieho uhla a ďalších parametrov, potrebných na určenie určenie maximáleho úberu a valcovacej sily.

Nasledujúca kapitola sa zaoberá plastickou deformáciou materiálu, jej popisom a modelovaním v konečnoprvkových programoch, najmä v prostredí Abaqus, ktoré je neskôr využité vo výpočtovej časti práce. V úvode je rozobratá inkrementálna teória plasticity, ktorá je kľúčová pre správne modelovanie elasto–plastickej odozvy materiálu. Postupne sú opísané jednotlivé jej piliere - podmienka plasticity, podmienka tečenia a podmienka spevňovania. Následne sú predstavené dva frekventovane využívané modely plasticity

s možnosťou zahrnutia vplyvu teploty a rýchlosti deformácie, ktoré sú dôležité pri simuláciách procesov tvárnenia. Ďalej sú predstavené možnosti predikcie vzniku tvárnej trhliny a jej simulácie. Sú predstavené viaceré kritéria porušovania, založené na princípe, že k vzniku tvárneho lomu dôjde, keď kumulované plastické pretvorenie dosiahne svojej limitnej hodnoty, tzv. lomového pretvorenia. Jeho hodnota závisí na rôznych premenných, ako napríklad faktore triaxiality napätia či Lodeho uhle, v závislosti od konkrétneho kritéria.

Predmetom ďalšej kapitoly je metóda konečných prvkov, hlavne jej explicitná formulácia, ktorá je použitá vo výpočtovej časti práce. Jej použitie je najviac rozšírené v prípade rýchlych, dynamických dejov, silne nelineárnych úloh, či úloh zahŕňajúcich porušovanie materiálu, ktoré môžu pre klasický implicitný algoritmus predstavovať výrazné problémy, alebo sú preň neriešiteľné. V prípade komplexných kontaktných podmienok pri valcovaní v kalibroch jej použitie podstatne uľahčuje riešenie úlohy. Kapitola začína popisom metódy centrálnych diferencii a získavania hodnôt jednotlivých veličín v časových prírastkoch. Objasnená je závislosť časového kroku a celkovej dĺžky výpočtového času na rozmere najmenšieho prvku v modeli a stým spojené možnosti škálovania hmotnosti. Ide o funkciu, ktorej použitím je možné zvýšením hustoty materiálu znížiť výpočtový čas potrebný na vykonanie analýzy. Popísané sú aj úskalia často používanej redukovanej integrácie prvkov, ktorá je spojená s problematikou hourglassingu. Ide o deformačný mód, ktorý nezodpovedá skutočnosti, a jeho prítomnosť môže skresliť a teda znehodnotiť výsledky analýzy.

Ďalšia časť je venovaná popisu základných princípov fotoelasticimetrie, tradičnej experimentálnej metódy, ktorou je možné získať rozloženia napätí a pretvorení v experimentálnom modeli, vyrobenom z fotoelastického materiálu a zaťaženom v podobnom duchu, ako skutočná súčasť. V minulosti bola táto metóda hojne využívaná v rôznych sférach priemyslu, v stavebníctve či dokonca zubárstve. Valcovanie je možné analyzovať deformáciou tenkého vzorku s prierezom zhodným so skutočným prevalkom. V tomto prípade ide o fotoplastickú analýzu - model prevalku je vyrobený z materiálu schopného plastickej deformácie.

Opis nastavenia a výsledkov štrukturálnej konečnoprvkovej analýzy aj experimentálnej fotoplastickej analýzy konkrétneho prípadu valcovania v kalibri, ktoré boli vykonané v predošlom výskume, je taktiež súčasťou predošlých dvoch kapitol. Ide o prechod štvorhrannej tyče oválnym a neskôr kruhovým kalibrom, nadobúdajúc kruhový prierez. Prechody jednotlivými kalibrami sú analyzované oddelene, čiže nie je rešpektovaná história zaťažovania. Pôvodný výpočtový model, v ktorom sú tenké modely prevalku zaťažované nedeformovateľnými modelmi oboch kalibrov, podobne ako pri spomínanom fotoplastickom experimente, slúži ako základ pre nový výpočtový model, zahŕňajúci skutočnú geometriu prevalku a kalibrov. Jeho tvorbe je venovaná nasledujúca kapitola a ďalej bude označovaný ako plný model.

Okrem plného modelu, ktorý je základom výpočtovej časti práce, sú vytvorené aj dve varianty podobné pôvodného modelu. V prvej z nich sú analyzované prechody jednotlivými kalibrami osobitne, pričom v druhej je model prevalku postupne zaťažený oboma kalibrami, rešpektujúc históriu zaťažovania. Tie sú ďalej nazývané ako separátny a sekvenčný zjednodušený model. Pre všetky modely sú použité okrajové podmienky pre dvojitú symetriu a teda je modelovaná len štvrtina prevalku a kalibrov. Tiež platí, že modely kalibrov sú definované ako nedeformovateľné skořepiny a teda nemajú pridelené žiadne materiálové parametre. Pre prevalok je použitý elasto–plastický model materiálu,

definovaný krivkou tečenia pre určenú referenčnú teplotu a rýchlosť deformácie. Teplotná ani časová závislosť materiálu nie je uvažovaná.

Pre vytvorené modely je použitá rovnaká sieť konečných prvkov, ako v pôvodnom výpočtovom modeli. Naviac sú vytvorené viaceré zjemnené varianty, pomocou ktorých je vykonaná analýza hustoty siete pre zistenie jej prípadného dopadu na získané výsledky. Táto analýza dokazuje, že v miestach vyhodnocovania výsledkov je vplyv hustoty siete zanedbateľný, a pôvodná varianta siete je ďalej považovaná za vyhovujúcu.

Keďže nie je uvažovaná časová závislosť materiálu, a informácie o rýchlosti zaťažovania pri pôvodnom výpočtovom modeli nie sú dostupné, sú vybrané primerané hodnoty. V prípade plného modelu je zvolená hodnota otáčok prvého kalibra. Otáčky druhého kalibra sú určené zo zákona zachovania objemu, aby bol zaistený plynulý tok materiálu. Aby bolo zabezpečené, že výsledky analýzy nebudú ovplyvnené dynamickými účinkami ani hourglassingom, je vykonané porovnanie hodnoty celkovej energie napätosti, kinetickej energie a energie hourglassingu. Na základe tohto porovnania je vplyv spomínaných javov považovaný za zanedbateľný.

Ďalej sú vykonané štrukturálne analýzy s použitím vytvorených modelov a získané rôzne výsledky. Ako prvé sú vyhodnotené rozloženia napätia a pretvorenia na priereze prevalku, následne porovnané s pôvodnými výpočtovými a experimentálnymi výsledkami. Z dôvodu významného rozdielu v hodnote redukovaného pretvorenia sú vyhodnotené jeho jednotlivé zložky. Ako bolo očakávané, rozdiely spočívali v normálovom a dvoch šmykových pretvoreniach, ktoré sú výrazne ovplyvnené použitím zjednodušenej geometrie. Priebehy napätí po rovinách symetrie modelu prevalku sú vyhodnotené a porovnané s experimentálnymi výsledkami. Ako bolo predpokladané, výsledky získané z analýzy s použitím zjednodušeného modelu bližšie odpovedali experimentu. V súlade s pôvodným článkom sú vyhodnotené a porovnané aj hodnoty faktoru triaxiality v troch bodoch na priereze prevalku. Rozdielny tok materiálu pri plnom a zjednodušenom modeli mal na priebeh hodnôt faktoru triaxiality značný vplyv.

Nakoniec je vykonané posúdenie tvárniteľnosti materiálu, resp. vyhodnotenie možnosti vzniku tvárneho porušovania. Oba použité prístupy sú definované krivkou závislosti lomového pretvorenia na faktore triaxiality, prebranou z pôvodného článku. Rovnako je prebratý aj prvý použitý prístup, založený na pomere aktuálneho ku limitnému plastickému pretvoreniu. Druhý prístup je založený na kumulatívnom kritériu tvárneho porušovania, ponúkané v prostredí Abaqus. Odstraňovanie prvkov z analýzy pri vzniku tvárneho porušenia nie je povolené. Kľúčovým rozdiel medzi týmito prístupmi je fakt, že hodnota kritéria tvárneho porušovania pre svoj rast vyžaduje rast plastického pretvorenia, kdežto pomer aktuálneho ku limitnému plastickému pretvoreniu nie. Tento jav je najvýraznejší pri odľahčovaní, resp. pri výstupe z valcovacej medzery, kedy bez rastu plastickej deformácie hodnoty pomeru aktuálneho ku limitnému plastickému pretvoreniu mnohokrát prekračujú hranicu iniciácie tvárneho porušovania, kým hodnota druhého kritéria zostáva nemenná. Takéto správanie nie je v súlade so skutočnosťou a preto podiel aktuálneho ku limitnému plastickému pretvoreniu nemôže byť správne použitý ako kritérium porušovania.

Hodnoty kritéria tvárneho porušovania, ako aj určené nebezpečné miesto prierezu prevalku pre prechod oboma kalibrami je podobné pri plnom a sekvenčnom zjednodušenom modeli. Plný model naviac odhaľuje lokálne maximum na okraji stykovej plochy prevalku a kalibra, ktoré pri zjednodušenom modeli nie je indikované. Nebezpečné miesto pri prechode druhým kalibrom pri separátnom modeli neodpovedá predošlým modelom. Rov-

nako je to aj v prípade maximálnej hodnoty kritéria tvárneho porušovania, ktorá je omnoho nižšia z dôvodu zanedbania plastického pretvorenia kumulovaného pri prechode prvým kalibrom. Avšak, výsledná hodnota po sčítaní hodnôt kritéria tvárneho porušovania v nebezpečnom mieste z oboch analýz takmer úplne odpovedá hodnote získanej pri sekvenčnom modeli. V závere práce sú tiež uvedené vplyvy, ktoré by do použitého výpočtového modelu mohli byť v prípade dostupnosti potrebných dát zahrnuté.

Kľúčové slová

valcovanie v kalibroch, objemové tvárnenie, fotoelasticimetria, tvárne porušovanie, štrukturálna analýza, explicitná metóda konečných prvkov, Abaqus

I hereby declare that I have written my master's thesis by the title *Computational simulation of pass rolling* by myself, using advice provided by my supervisor, Prof. Ing. Jindřich Petruška, CSc. and the sources listed near the end of the thesis.

. . . .
Samuel Hacek
June 26, 2020

Contents

1 Introduction

It can be assumed that all metalworking operations known today evolved from activities as simple as forming naturally-formed metal objects into convenient shapes, using tools as primitive as rocks. Over the millenia, these tools were replaced by more precise, man-made tools and by the time of the industrial revolution, machines were used to carry out most of the tasks. Machinery further evolved, becoming more powerful, precise and able to perform a wide variety of tasks. Obviously, with the improvement of the tools and machines, various requirements grew stricter than ever, such as accuracy, quality and economic value. In order to optimize the processes and therefore satisfy the requirements, they needed to be properly described and in-depth understanding needed to be achieved.

At first, basic knowledge was acquired by observation and realization of simple experiments, utilizing trial and error approach. Upon these basics, many of more or less complex empirical approaches were invented. Traditional empirical approaches often involved a vast amount of experimental testing, which proved too costly without proper prediction of the results. Analytical approaches could scarcely be applied to complex cases which needed to be solved. To deal with this, new numerical variational methods were invented, FEM (Finite Element Method) being probably the most well-known and used among them. Their usage, however, was limited because of insufficient computational power. Due to this, heavy simplifications took place to ensure that the problems could be solved and desired results would be available within acceptable time horizons.

Analyses of rolling or similar metalworking technologies were no exception. They were carried out to evaluate relevant parameters during the process, such as stress within therolls or plastic deformation of the workpiece, values of which could be used to optimize the process and improve the quality of the product. Other purpose was evaluation of the possibility of material damage occurence, which would render the product or the tools useless, by employing various more or less advanced criteria. Due to large deformation, complex contact conditions and material flow at high temperatures, finite element analysis of pass rolling is a highly complicated, nonlinear problem, which could only be carried out in a simplified manner. In an attempt to validate the obtained results, simple experiments were devised, one of them being photoplastic analysis of a slice of epoxy resin capable of plastic deformation.

In recent decades, with computing technology skyrocketing, FEM simulations quickly became an essential tool in engineers' arsenal. In addition to being able to develop far more complex computational models to solve problems previously beyond their capability, engineers could now look back and review the previously used methods, determine the impact of the simplification on the obtained data and judge their sufficiency and effectivity when compared to the most recent tools at their disposal.

1.1 Motivation

Due to large deformation, complex contact conditions and material flow at high temperatures, computational modelling of pass rolling is a highly complex, nonlinear problem, which, with limited computational power at disposal, could only be solved with heavy simplifications taking place. Using current means of computational modelling, it is possible to create computational models far more accurate at describing real conditions. The output of this thesis should be an assessment of the impact of simplification in previous, simpler computational models based on comparison with results acquired with modern computational model.

1.2 Problem formulation

As stated in this thesis' specification, designing an appropriate sequence of profiles in pass rolling is a complex problem which was traditionally solved employing industrial experience, experimental procedures and simple computational modelling. The objective of this thesis was to choose an appriopriate modern-day finite element software to create a computational model of certain pass rolling problem, which was analysed in previous research using simplified computational model and experiment, assess credibility of the obtained results, evaluate its efficiency and compare it to the simplified computational and experimental solution.

1.3 Goals of the thesis

Following goals are supposed to be fulfilled in the thesis:

- Study of traditional methods of pass rolling analysis

- Computational simulation of material flow through a selected sequence of passes by a 3D finite element model, including the material and frictional nonlinearity.

- Comparison of the results with both experimental and previous, simplified computational solution.

- Evaluation of the efficiency and predictive reliability of the modern procedure

2 System of essential variables

According to information found in [1], a system of essential variables was defined for the pass rolling problem which was solved in the computational part of the thesis.

Environment

Temperature of the workpiece is defined by the used flow curve and is considered homogenous, so no heat transfer occurs between the workpiece and the environment throughout the process. The surrounding environment does not influence the assembly in any other way.

Geometry and topology of the rolling assembly

The initial shape of the workpiece is a rectangular rod of initial length and width, filleted at the corners. No impact of previous cutting process on the model is considered as all variables are evaluated on the cental part of the length of the workpiece.

Being much stiffer than the workpiece, both roll passes as well as pusher are considered rigid, with only those surfaces that come into contact with the workpiece are taken into account.

Pairs of roll passes are positioned perpendicularly to each other with central points of both rolling gaps laying in line of the movement of the center of the workpiece, so that it enters and exits both rolling gaps in a straight line. The distance between the rolling gaps is short enough to ensure that the workpiece enters the second before leaving the first one. Pusher is positioned next to the rear end of the workpiece.

Interactions and bonds with the environment

Symmetry boundary conditions are defined for all bodies so that symmetry planes lay perpendicular to the axes of the rolls. Surfaces of the roll passes are fixed and are assigned constant angular velocity throughout the process. Surface of the pusher is assigned a displacement boundary condition to push the workpiece into the rolling gap. Frictional interaction with constant friction coefficient is assumed between rigid surfaces and the workpiece.

Activation of the rolling assembly

The workpiece is pushed into into the first pair of roll passes by the surface of the pusher, then dragged and passed through two rolling gaps, its length increased and cross–sectional area reduced in the process. Initial rectangular cross section is reshaped into oval and then into a circle.

Impact on the the rolling assembly

The assembly is not influenced by the environment in any way.

Properties of the rolling assembly

The material of the workpiece is ČSN 41 7246 stainless steel alloy with elastic–plastic behavior. Elastic component is considered to be linear isotropic and is defined by proper independent variables. The plastic component is defined by a flow curve at reference strain rate and temperature, so no rate or temperature dependency is considered.

Since both roll passes and pusher plate are defined as rigid surfaces, they are not assigned any material parameters.

States and processes of the rolling assembly

Initially, the workpiece is in unloaded state, as no residual stresses are considered at the start of the process. When passing through the rolling gap, the workpiece is subjected to compressive loading and transformed from undeformed to deformed state. If equivalent plastic strain reaches its critical value, ductile damage initiation might occur. After leaving the rolling gap, the deformation load subsides and residual stresses are present in the workpiece.

Consequences

Due to high temperature throughout the process, vast majority of strain is considered plastic and therefore permanent. Rolling process does not influence the surrounding environment in any way.

Overview of usable methods

Since the thesis' appointment directly specifies that Finite element method shall be used to fulfill its goals, no other methods, experimental or computational, were considered viable.

Finite element method is the most widely known variational computational method used to solve a broad range of problems. Depending on the type of the task at hand, either implicit or explicit finite element algorithm may be used. Implicit FEM is commonly employed to solve most of the problems. Compared to explicit, it uses much longer timestep, resulting in shorter computational time. Explicit FEM, thanks to its conditional stability and short time step, is well suited for solving quick, dynamic and/or highly nonlinear problems.

In this case, due to nature of the analysed problem, namely the complex contact conditions, convergence and successful solution would be hard to achieve using implicit algorithm, thus making explicit a more viable choice. Of all commercial softwares that offer explicit solvers, such as LS Dyna, PamCrash, Radioss or Abaqus, the last one was chosen, due to wide variety of analysis tools and options it provides as well as the author's previous experience with the software.

3 Rolling technology

Technology of rolling is one of the most productive and economically efficient methods of metalworking. Since the first known drawing of a rolling mill design, conceived by Leonardo Da Vinci (see Fig. 3.1a) by the end of 15th century, and later introduction to steel production during the Industrial revolution (see Fig. 3.1b), sometimes contributed to british manufacturer and inventor Henry Cort [2], it has become one of the most widely used methods of metal production, with approximately 90 % of all metal products undergoing at least one rolling process.
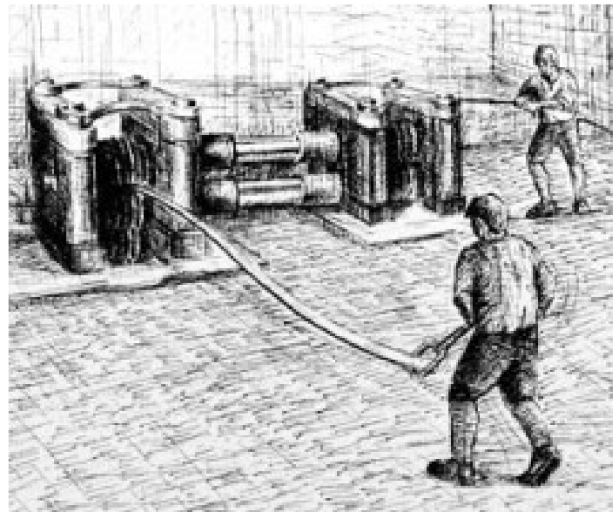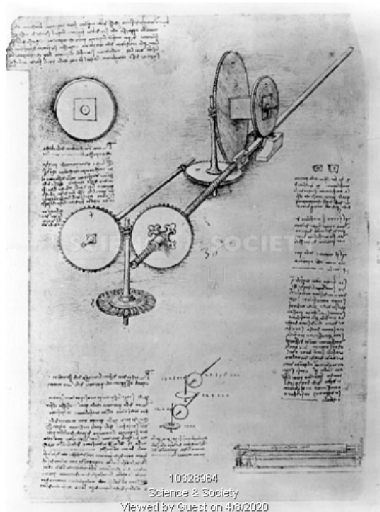
(a) Rolling mill concept by da Vinci [3]   (b) Rolling mill during Industrial revolution [4]

Figure 3.1: Depiction of historical rolling mills

Rolling belongs among bulk metalforming technologies, where severe deformation occurs, resulting in massive shape change. Workpiece is drawn and compressed between a pair of rotating rolls, its thickness reduced or shape altered.

The following chapter serves as an overview of various rolling methods, basic rolling mill configurations, a description of the mechanics of rolling process. Emphasis is put on roll pass design, as pass rolling is the main subject of the thesis.

3.1 Rolling methods

Following paragraphs describe rolling methods distinguished using multiple criteria.

Rolling methods by rolling direction

Depending on the direction the workpiece moves, i.e. the rolling direction, and the position of the rolls, three major methods are distinguished [5, 6, 7]:

- Longitudinal rolling - material is fed to the rolling gap in longitudinal direction (see Fig. 3.2a). Axes of the rolls, which turn in opposite directions, are parallel to each other and perpendicular to the direction of the movement of the workpiece. Usable for a vast majority of products, this method is the most common among the three mentioned.

18

- Transverse rolling - rolls turn in the same direction and their axes are parallel to each other as well as to the axis of the workpiece, which is shaped while turning between the two of them (see Fig. 3.2b). This method is mainly used for shaft production with flat rolls or thread production using grooved rolls [8].

- Skew (slantwise) rolling - analogical to transverse rolling, with the difference being the skewness of the axes of the rolls (see Fig. 3.2c). This method is utilized in seamless piping production, when a small indentation made on the end of the workpiece, which is further propagated by a piercer roll which guides the flow of the material to form the desired pipe shell [9]. Skew rolling is also employed in steel ball production, with the balls shaped and severed by spiral groove rolls [10].
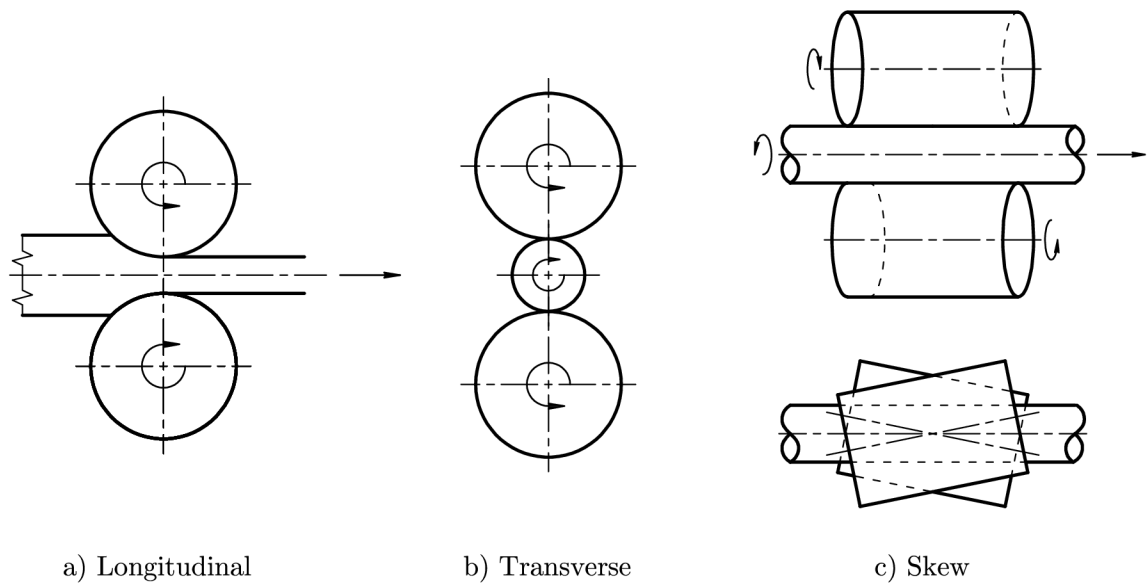

a) Longitudinal   b) Transverse   c) Skew

Figure 3.2: Rolling methods by rolling direction

Rolling methods by roll and product shape

Depending on the shape of the rolls and product, longitudinal rolling is divided into [5, 6]:

- Flat rolling - used for sheet or plate rolling, surface of the rolls is flat, being in contact with the workpiece along the width (see Fig. 3.3a).

- Pass rolling (shape rolling) - used for various shaped products. Rolls contain one or more contoured grooves to guide flow of the material and obtain desired shape of the product (see Fig. 3.3b).
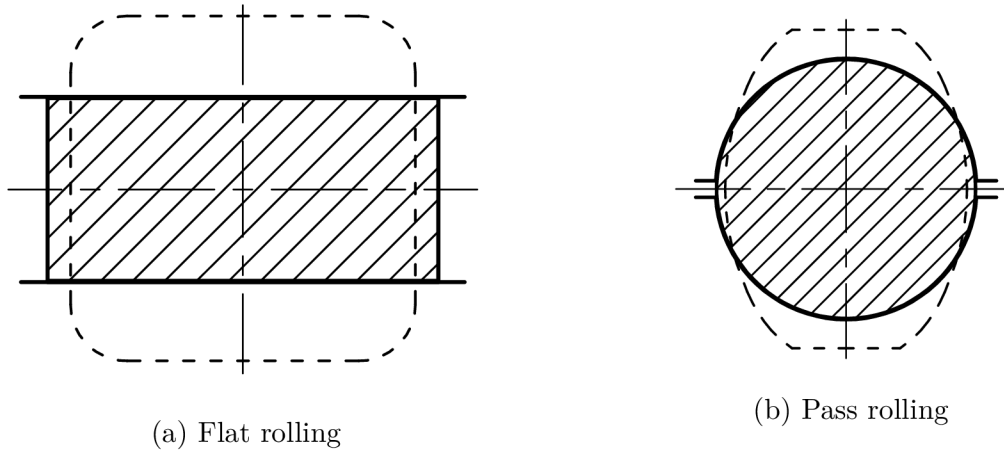
(a) Flat rolling

(b) Pass rolling

Figure 3.3: Cross–sectional views of flat and pass rolling process [5]

Rolling methods by rolling remperature

Depending on whether the temperature during the process is above or below the recrystallization temperature of the material, following rolling types are dinstinguished [6, 7]:

- Cold rolling - With their volume kept contant, material grains are deformed in rolling direction. Since recrystallization and recovery does not occur, conveniently oriented slip systems are depleted and dislocation count grows which, leading to strain hardening.

- Hot rolling - above recrystallization temperature, deformation causes nucleation and growth of new material grain. Being refined, newly grown material grain significantly improves formability of the material.

3.1.1 Rolling mill configurations

Rolling mill stands come in wide variety of configurations, depending on the number of used rolls or reversing capabilities [6, 7]:

- Two–high non–reversing - the simplest type of rolling mill which allows the workpiece to pass in one direction. This configuration is depicted on Fig. 3.2a.

- Two–high reversing - similar to previous configuration, but capable of allowing the workpiece to pass in both directions. The downside is that it has to be stopped and reversed between the passes.

- Three–high rolling - solves the inconvenience of stopping and reversing, but requires a mechanism able of moving the workpiece in vertical direction between the passes (see Fig. 3.4a).

- Four–high and cluster - this configuration utilizes backing rolls for support (see Fig. 3.4c). It is used for rolling of thin workpieces, plates or foils. In these cases, diameter of the rolls is lower, contact length is reduced, resulting in the rolls being subjected to three–point bending, which causes them to flex and may lead to significant variance in product thickness.

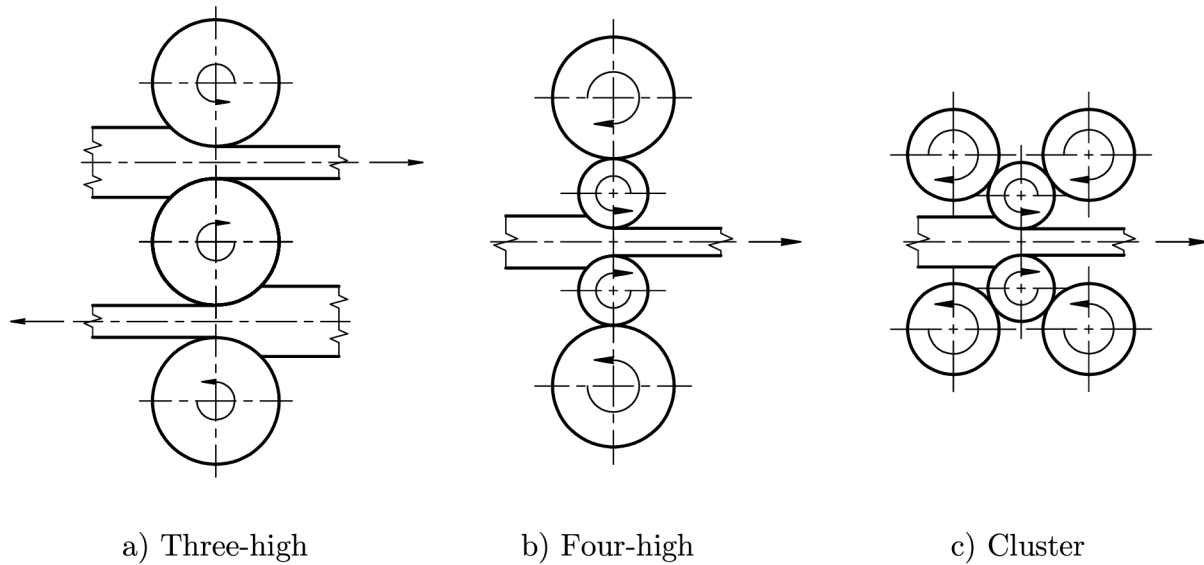a) Three-high   b) Four-high   c) Cluster

Figure 3.4: Basic rolling mill configurations [7]

Rolling mill configurations mentioned above are used for non–continuous rolling, meaning that at a given time, material of a workpiece passes through just one rolling gap. The opposite is tandem rolling, where the back end of the workpiece does not leave the first rolling gap until the front end enters the second. This method is often utilized for pass rolling or wire rolling. Tandem rolling mills employ multiple non–reversing pairs of rolls. When the workpiece passes through multiple rolling gaps at the same time, volume passed in the same amount of time must be equal for each pass. Also, reduction of the cross–sectional area must be equal to velocity increase. Angular velocity of each consecutive pair of rolls must be greater than the previous and correctly calculated. If any pass requires more incoming material than the previous is able to produce, tension is generated, increasing the risk of material damage occurrence. Oppositely, when too much material is produced by a pair of rolls, it accumulates between the passes, causing further problems.
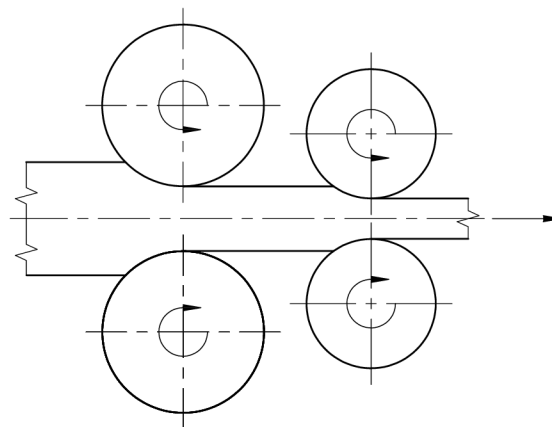

Figure 3.5: Tandem rolling [7]

3.1.2 Stock material

As may be seen on Fig. 3.6, multiple types of stock material are recognized, rolled from ingots or obtained through continuous casting [7]:

- Billet - similar to bloom, but usually thinner. Additionally, it may also possess circular cross section. Billets are often pass–rolled into bars, rods or wires.

- Bloom - square or rectangular profile, with width of at least 15 cm, but not greater than its height. Blooms are usually pass–rolled into finished products, such as structrural shapes or rails. Another variant is semifinished round profiles, some of which can be further processed into seamless tubes.

- Slab - rectangular profile with width at least twice the size of height. Slabs are flat–rolled into plates, sheets or strips, each of which is recognized by its thickness.
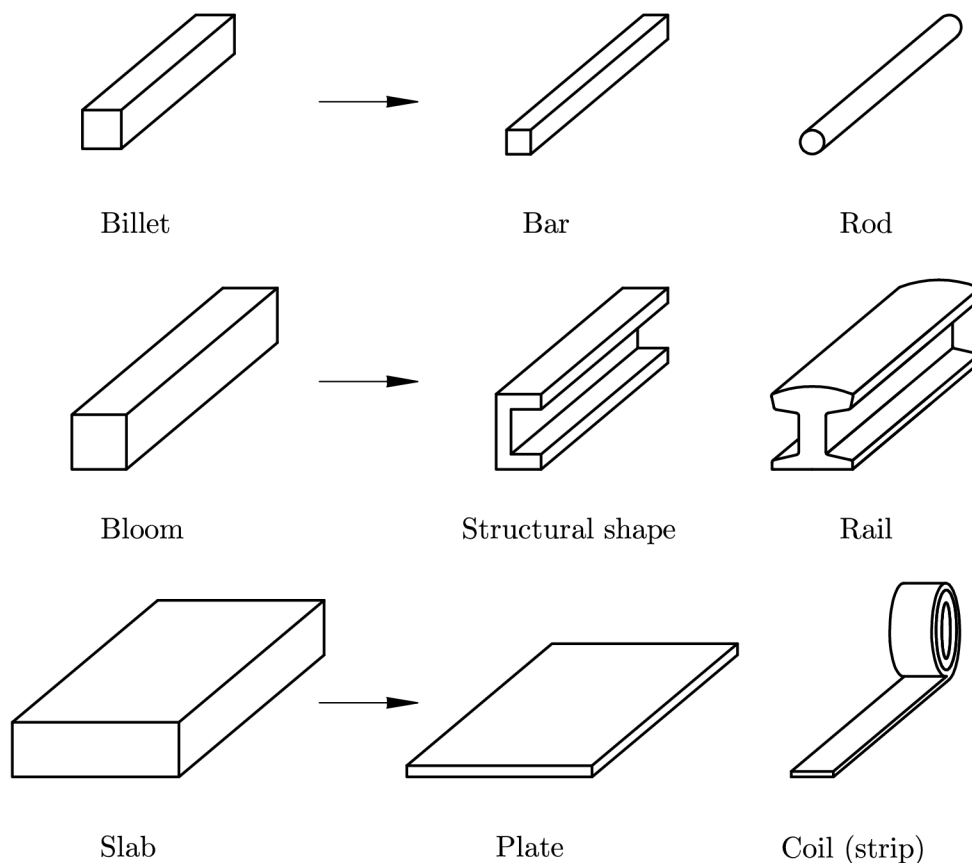

Figure 3.6: Various types of stock material and products [7]

3.2 Rolling process

During rolling process, the workpiece enters and passes through the rolling gap - the space between the rolls with thickness or cross–sectional area smaller than that of the workpiece. Overall deformation of the workpiece may be decomposed into following components [5, 7]:

- Reduction - reduction of the height of the workpiece.

- Elongation - increase of the length of the workpiece.

- Spread - difference between initial and final width of the workpiece.

.

3.2.1 Friction in rolling operations

Since only external friction is usually taken into account for bulk forming operations, friction may be defined as resistance against relative movement of two bodies at their interface, acting in tangential direction [11].

Friction is an important parameter in rolling operations, as it not only affects rolling force values and degradation of the surface of the rolls, but is also directly responsible for successfull commencing of the rolling process [12]. Provided that certain conditions (further described in Sec. 3.17) are satisfied, bite occurs: frictional forces on the interface of the parts cause the workpiece to be pulled into the rolling gap. The state when the entirety of rolling gap is filled with material is called stable rolling. In case of inappropriate rolling conditions, frictional forces fail to bite and pull the workpiece through the rolling gap and the surfaces skid on each other instead. Specific friction coefficient μ_f is associated with each of these stages [5]:

- Bite friction μ_b

- Stable rolling friction μ_r

- Skidding friction μ_s

All of these values depend on multiple parameters, such as lubrication, surface roughness, temperature, chemical composition, contact pressure and their values are often obtained through experiment. Frictional coefficient is always higher during the bite and lowers as the rolling is stabilized, the most common assumption being that its value is twice as high during bite [5].

3.2.2 Material flow

Throughout rolling process, it is assumed that the volume of the formed material remains constant, which means that the law of continuity is obeyed:

$$S_0 \cdot v_0 = S_1 \cdot v_1 \tag{3.1}$$

where S_0 and S_1 stand for initial and final cross–sectional area and v_0 and v_1 for initial and final velocity of the workpiece.

In cases such as tandem rolling, where knowledge of velocity of the workpiece inside each rolling gap is crucial, it is useful to express the law of continuity as

$$S_1^{gap} \cdot v_1^{gap} = S_2^{gap} \cdot v_2^{gap} = S_n^{gap} \cdot v_n^{gap}, \tag{3.2}$$

where S_1^{gap}, S_2^{gap} and S_n^{gap} stand for cross–sectional area and v_1^{gap}, v_2^{gap} and v_n^{gap} stand for velocity of the workpiece during passage through first, second and n-th rolling gap.

Final velocity of the workpiece is always higher than circumferential velocity of the rolls. Relative velocity increase, called forward slip, is defined as:

$$i = \frac{v_1 - v_c}{v_c} \quad [5], \tag{3.3}$$

where i stands for forward slip and v_c for circumferential velocity of the rolls.

In order to secure optimal flow of the material in continuous rolling, correct values of circumferential velocities of the rolls must be used. These values may be obtained by substituting forward slip into eq. 3.2:

$$S_1^{gap} \cdot v_{c1}^{gap} \cdot (1 + i_1^{gap}) = S_2^{gap} \cdot v_{c2}^{gap} \cdot (1 + i_2^{gap}) \quad [5], \tag{3.4}$$

where v_{c1}^{gap} and v_{c2}^{gap} stand for circumferential velocities of the rolls and i_1^{gap} and i_2^{gap} for forward slip in passage through the first and the second rolling gap.

Forward slip depends mainly on neutral angle, which is described in Sec. 3.2.3, and assumes values in range from 2 to 10 %. In case of pass rolling, forward slip is non–homogenous due to neutral angle varying along the cross-section of the workpiece [5].

3.2.3 Deformation zone

Deformation of the workpiece does not occur uniformly throughout the volume, but only in the deformation zone, which may be seen on Fig. 3.8. A substantial parameter used to describe deformation zone is geometric ratio L_r, defined as

$$L_r = \frac{l_s}{h_m} \quad [12], \tag{3.5}$$

where l_s stands for horizontal projection of contact length of the rolls and the workpiece and h_m for mean height of the workpiece in the rolling gap.

For symmetrical pass rolling, i.e. when diameters of both rolls are equal, an example of which may be seen on Fig. 3.7, l_s is acquired from

$$l_s = \sqrt{R_m \cdot \left(\frac{S_i}{w_{i_{max}}} + \frac{S_f}{w_{f_{max}}} \right)} \quad [12], \tag{3.6}$$

where R_m stands for effective roll radius (further described in Sec. 3.3.1), $w_{0_{max}}$ and $w_{1_{max}}$ for initial and final maximum width of the workpiece.

For the same conditions, h_m is defined as

$$h_m = \frac{1}{2} \cdot \left(\frac{S_i}{w_{i_{max}}} + \frac{S_f}{ww_{f_{max}}} \right) \quad [12]. \tag{3.7}$$

Higher values of L_r ($L_r > 0{,}8$) are associated with rolling of thin products, while lower values ($L_r < 0{,}5$) are typical for thick product rolling [5, 12].
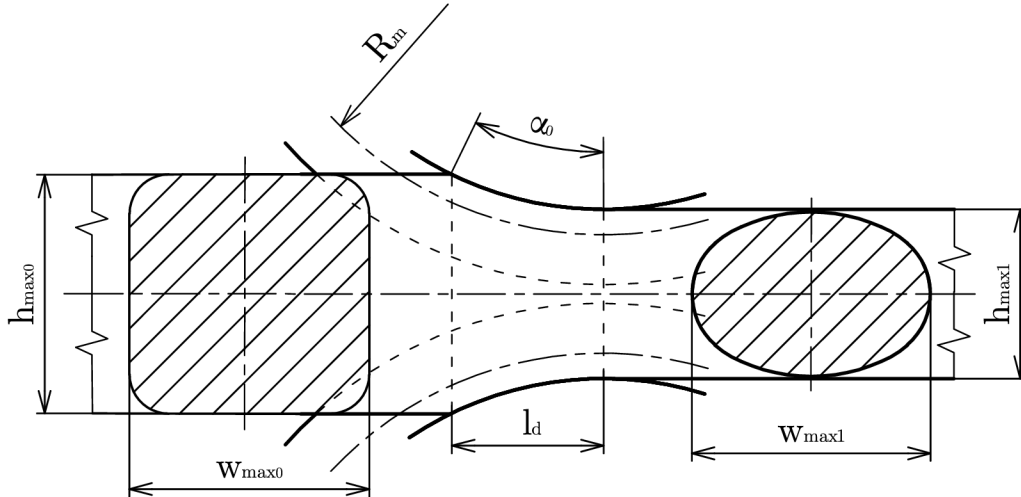
Figure 3.7: An example of pass rolling process [12]

Along deformation zone length l_d, which is also defined by bite angle α_0, velocity of the workpiece continuously increases from initial v_i to final value v_f, eventually surpassing circumferential velocity of the rolls, value of which is higher at the start of the process. When unequal velocity distribution throughout the cross section of the workpiece, notable in case of pass rolling or thick product rolling, is neglected, the workpiece is assumed to move with mean velocity of the workpiece v_m. The position where v_m is equal to horizontal component of circumferential velocity of the rolls v_c is determined by neutral angle α_n:

$$v_m = v_c \cdot cos(\alpha_n) \quad [5]. \tag{3.8}$$

Neutral angle defines position of the neutral plane, which divides the deformation zone into:

- Lagging zone (marked as I on Fig. 3.8) - circumferential velocity of the rolls is higher than of the workpiece. Frictional forces on the interface are oriented in the rolling direction and accelerate the workpiece, which moves at lower velocity.

- Leading zone (marked as II on Fig. 3.8) - velocity of the workpiece has already surpassed circumferential velocity of the rolls. Frictional forces on the interface act against rolling direction and slow down the faster moving workpiece.
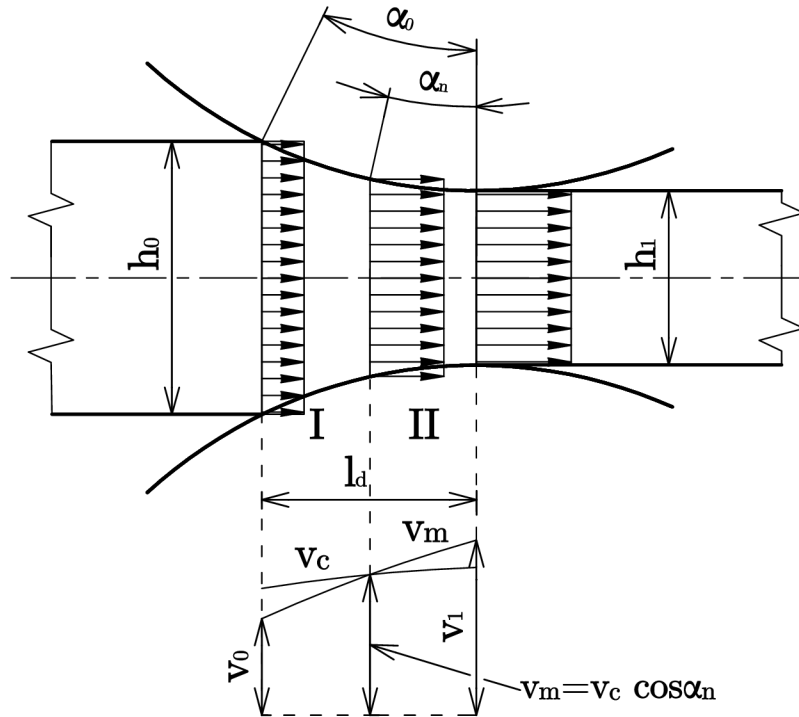
Figure 3.8: Depiction of deformation zone and courses of velocities [5]

Shape of the neutral plane is usually assumed to be planar, which is true only for rolling of thin products. In case of thick products, however, notable inequality of strain and velocity distribution causes it to bend in the rolling direction near the surface of the workpiece, assuming shape of a common surface, described by varying neutral angle. Bent shape of the neutral plane and courses of velocities along the deformation zone, which were previously mentioned, and the newly distinguished velocity of the surface of the workpiece v_s, may be observed on Fig. 3.9.
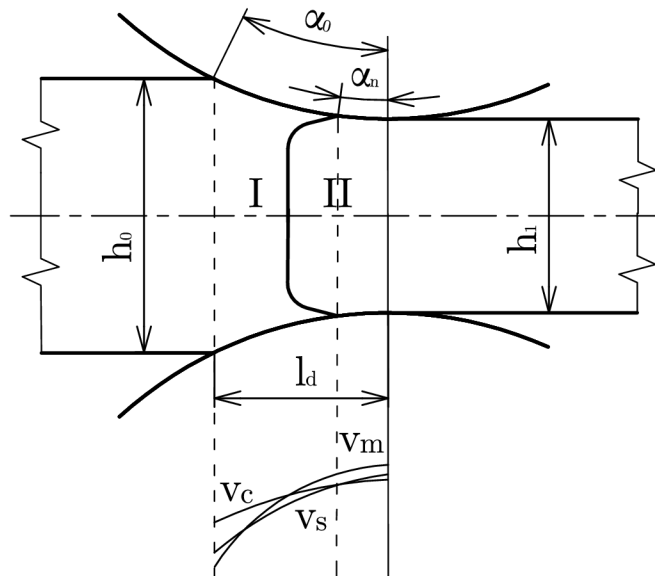

Figure 3.9: Bent shape of neutral plane and courses of velocities [5]

Deformation zone defined by lagging and leading zone corresponds with cold rolling or rolling of thin products. To better capture conditions during hot rolling and pass rolling, an additional zone that surrounds the neutral plane, called sticking zone (marked as III on Fig. 3.10a), is considered. Slipping of the surfaces is neglected within sticking zone, and velocities of the rolls and the workpiece are assumed to be equal throughout its width, instead of just in the neutral plane. Width of sticking zone assumes higher values during hot rolling and rolling of thick products. In case of pass rolling, it usually occupies majority of the deformation zone.

Until now, geometric deformation zone length was assumed, meaning that the deformation occurs only during the contact. In real conditions, however, deformation occurs throughout extended deformation zone, length of which l_d^{ext} depends mainly on height reduction of the workpiece Δh and assumes values 1,2 to 1,7 times greater than l_d [12]. Extended parts on each side of the deformation zone are known as waking deformation (marked as IV on Fig. 3.10a) and subsiding deformation zone (marked as V on Fig. 3.10a). These zones are usually taken into account when thick products are rolled [5].

Another previously omitted phenomenon is the impact of different stress states at both sides of the workpiece, in the spreading zones (marked as VI and VII on Fig. 3.10b). Unlike other zones, where compressive triaxial stress state is present, tensile stress is observed in spreading direction. Since tensile stress reduces formability of the material, spreading is usually regarded as a negative phenomenon, except pass rolling, when spreading is required to fill the rolling gap in order to achieve the desired cross–sectional shape of the product. Borderlines of the spreading zones are determined by the direction of material flow, i.e. whether the material moves in rolling or spreading direction. In pass rolling, spreading always occurs because of non–homogenous height reduction along the width of the workpiece. Spreading is most notable in regions with highest height reduction [5, 12].
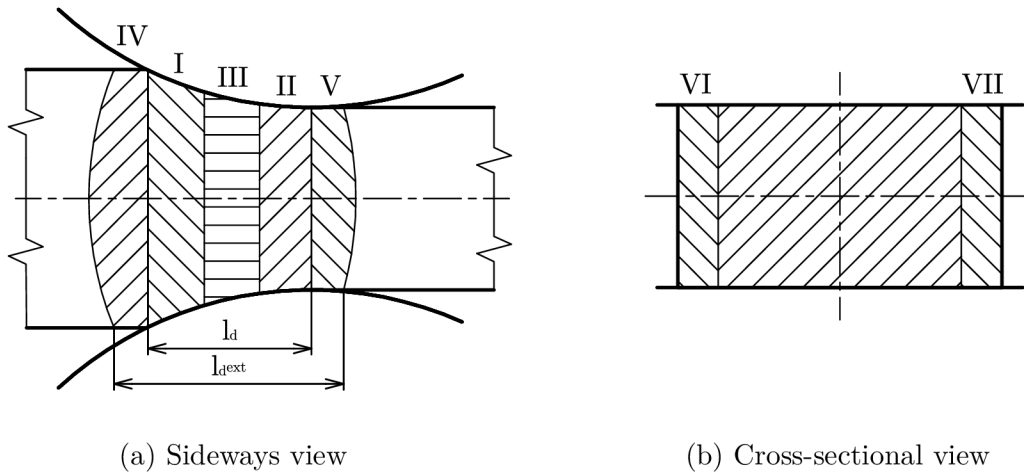

(a) Sideways view   (b) Cross-sectional view

Figure 3.10: Depiction of extended deformation zone [5]

3.2.4 Uneven deformation of the workpiece

If uniform deformation was assumed to occur throughout the rolling process (see Fig. 3.11), width change would assume zero value and following equation would be true:

$$\frac{\mathrm{d}h_0}{h_0} = \frac{\mathrm{d}h_1}{h_1} \quad [5], \tag{3.9}$$

where $\mathrm{d}h_0$ and $\mathrm{d}h_1$ stand for initial and final height of elementary layer of material in the deformation zone and h_0 and h_1 stand for initial and final height of the workpiece.

In real conditions, due to frictional forces, temperature inhomogeneity or roll pass shapes, previous assumption is false. Due to uneven deformation, additional stresses are generated and values of velocity, stress and strain vary throughout the deformation zone.
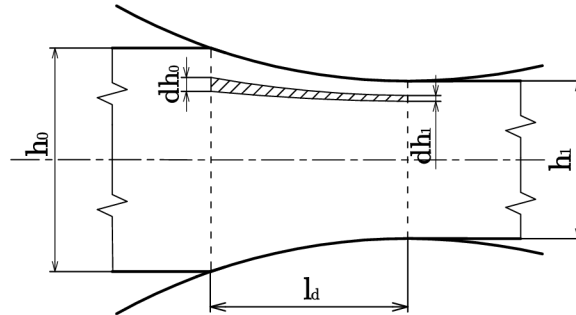

Figure 3.11: Deformation of elementary layer of material in the rolling gap [5]

Due to frictional forces, generation of compressive plastic strain is hindered in the area surrounding the contact surface. Borderlines of this zone assume shape of a cone and is therefore called friction cone zone (marked as I on Fig. 3.12). These zones meet or even overlap at the center when thin products are rolled. For thicker products, impact of frictional forces is less significant and friction cone zones do not reach throughout the whole height. Past friction cone zone lies intense deformation zone (marked as II on Fig. 3.12), where higher amounts of plastic deformation are developed. Compressive stress in vertical direction σ_1 decreases towards the center of the workpiece, which results in lower plastic strain and may utterly prevent plastic strain generation in center of thick products. Plastic strain is therefore concentrated beneath the surface of the workpiece. In case of thin products, plastic strain is more evenly distributed along the height of the workpiece. Possible layouts of plastic deformation zones for both cases may be seen on Fig. 3.12. In addition, waking (marked as III on Fig. 3.12b) and subsiding deformation zone (marked as IV on Fig. 3.12b) are also be considered for rolling of thick products.
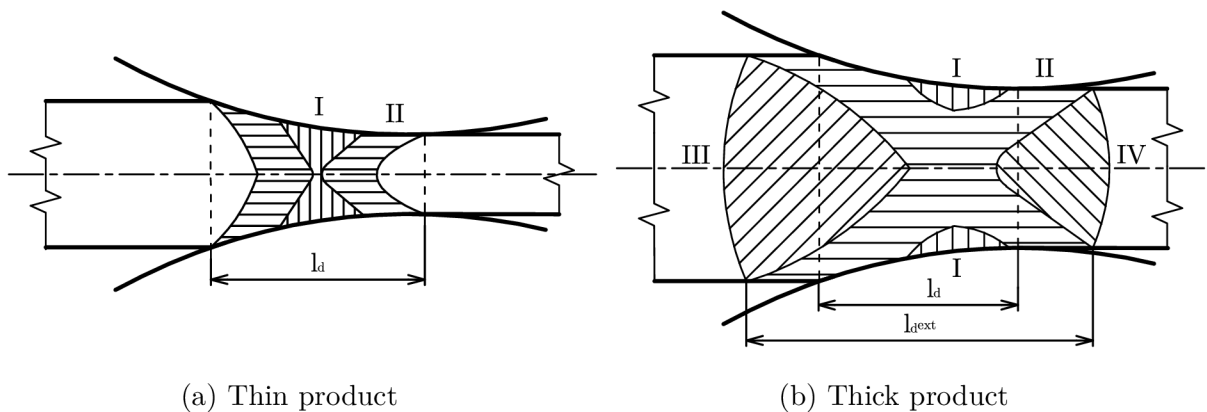
(a) Thin product   (b) Thick product

Figure 3.12: Plastic strain distribution in the deformation zone [5]

3.3 Roll pass design

Proper roll pass design is the cornerstone of shape rolling and rolling mill stand production as well. Thermomechanical conditions, dimensions and material of the rolled stock are among many factors taken into account. Purpose of roll pass design is to devise optimal reduction plan and appropriate number, shape, order and size of used roll passes. These precautions secure that the workpiece is thoroughly formed and undamaged by the process, while the precision of dimensions and cross section shape of the final product fall within required tolerance intervals [12].

Roll pass is defined as the area between the rolls, laying in the plane that contains axes of both rolls, its borders being grooves of the rolls which determine the final shape of the rolled material. Flanges located on both sides of roll pass guide deformation in spreading direction. Fact that height reduction and deformation of the material is not evenly distributed along the width of the workpiece as in case of flat rolling significantly increases complexity of calculations required to properly determine important process parameters [5, 12].

3.3.1 Effective roll diameter

A substantial parameter of pass rolling is effective roll diameter D_m, which is synonymous with roll diameter in case of flat rolling. In pass rolling, however, the diameter of the rolls varies along its width and effective roll diameter has to be used instead. It defines the position where circumferential velocity of the rolls and velocity of the workpiece are equal [12]. Effective working diameter D_m is defined as

$$D_m = 2 \cdot R_m. \tag{3.10}$$

Value of R_m may be determined using multiple available methods, with different formulas used for specific pass roll shapes. R_m of oval pass, possible position of which may be seen on Fig. 3.13a is obtained from:

$$R_m = \frac{r \cdot \varphi_0 \cdot \sqrt{\left(\frac{R_k}{2r} + 1\right) \cdot \frac{R_k}{2r}}}{arctg\sqrt{\left(\frac{2r}{R_k} + 1\right) \cdot tg\frac{\varphi_0}{2}}} \quad [12], \tag{3.11}$$

where r stands for radius of the roll pass groove, R_k for minimum roll radius and φ_0 for angle of the oval roll pass groove.

For circular pass, which may be seen on Fig. 3.13b, R_m is defined as

$$R_m = \frac{\frac{\pi \cdot r}{2} \cdot \sqrt{\left(\frac{R_k}{2r} + 1\right) \cdot \frac{R_k}{2r}}}{arctg\sqrt{1 + \frac{2r}{R_k}}} \quad [12], \tag{3.12}$$

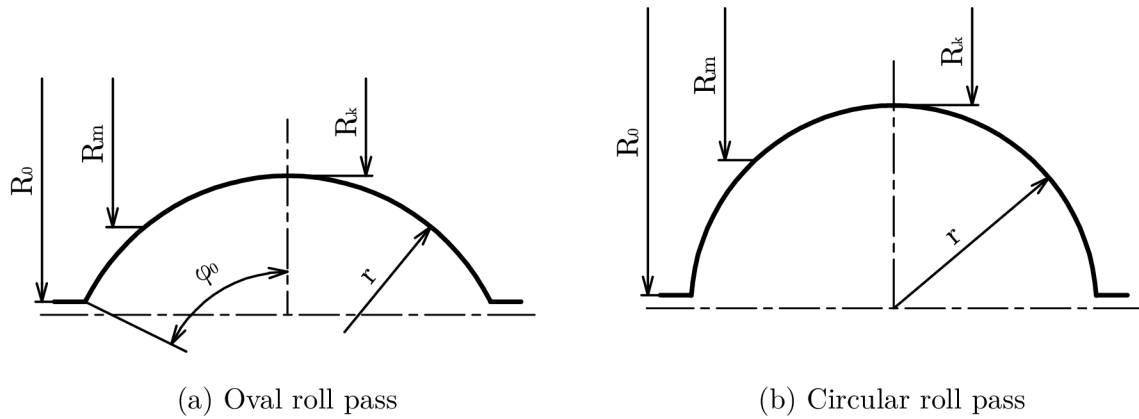(a) Oval roll pass $\qquad$ (b) Circular roll pass

Figure 3.13: Geometry of chosen roll pass shapes [12]

3.3.2 Neutral angle

In case of pass rolling, position of neutral plane is often defined by neutral line, which is defined as intersection of neutral plane and contact surface between the workpiece and the rolls. For the purpose of simplification, equal velocity is assumed at each point of the cross section. Furthermore, a pair of rolls is assumed symmetrical and only two deformation zones are considered. Due to circumferential velocity of the rolls varying along the contour of the roll pass, the neutral line, as well as the deformation zone is curved in the rolling direction (see Fig. 3.14).
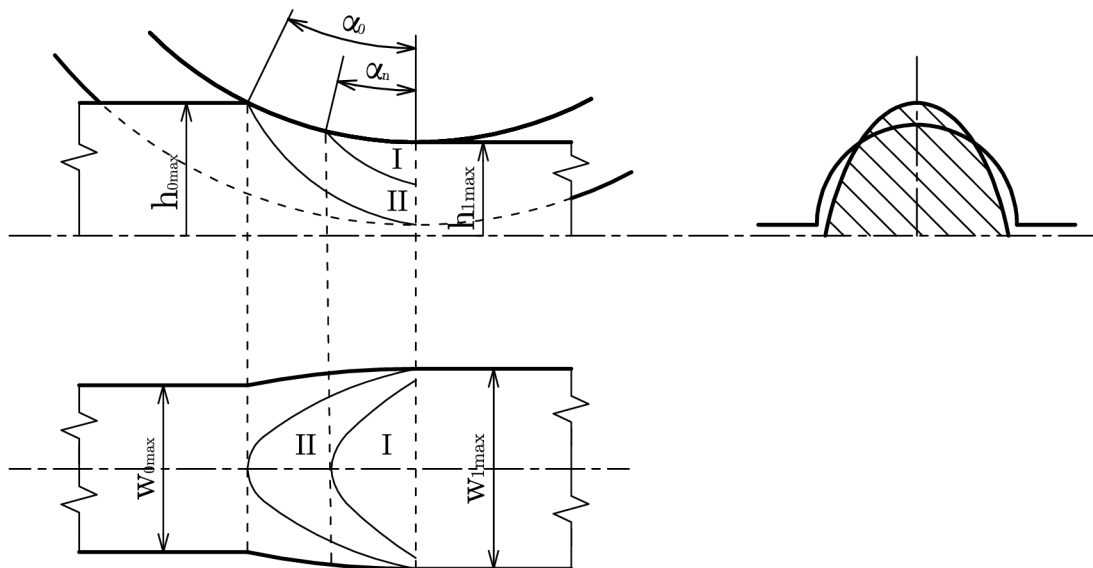

Figure 3.14: Neutral line and deformation zone bent in rolling direction [12]

Neutral angle at the effective diameter of the rolls may be acquired from the following equation, using dimensions of the workpiece:

$$\alpha_n = \frac{w_{0max} + w_{1max}}{3 \cdot (w_{0max} + w_{1max})} \cdot \left(1 - \frac{\alpha_{0m}}{2 \cdot \mu_f}\right) \cdot \alpha_{0m} \quad [12], \tag{3.13}$$

where α_{0_m} stands for mean bite angle, defined as

$$\alpha_{0_m} = \frac{\frac{S_0}{w_{0_{max}}} - \frac{S_1}{w_{1_{max}}}}{\sqrt{R_m \cdot \left(\frac{S_0}{w_{0_{max}}} - \frac{S_1}{w_{1_{max}}}\right)}} \quad [12] \tag{3.14}$$

Neutral line shape for a specific pass rolling problem may be described using various analytical approaches. An example of neutral lines for oval pass–rectangular workpiece and circular pass–oval workpiece problems may be seen on Fig. 3.15a and 3.15b, respectively. On both figures, neutral line is marked as a, contact surface between the roll and the workpiece as b and maximum width of the workpiece in the rolling gap as c.
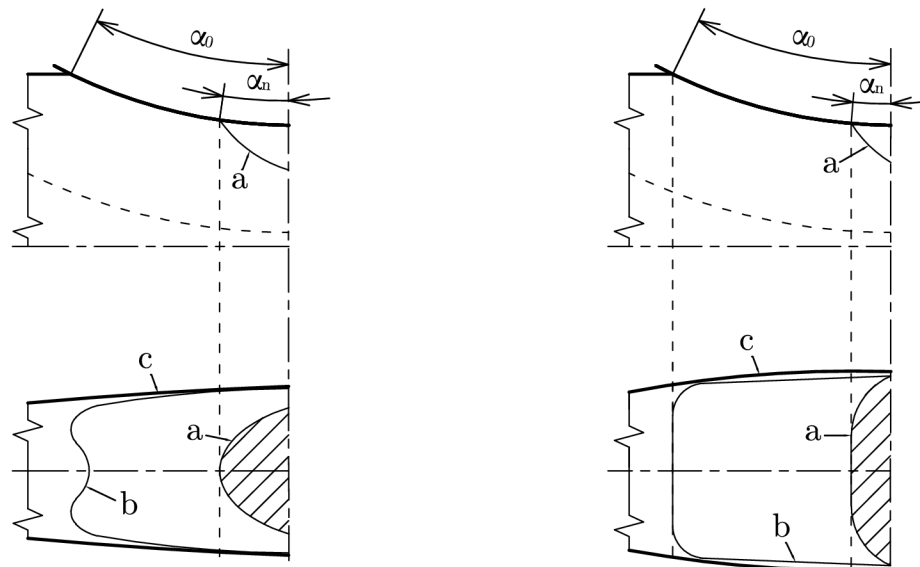
(a) Oval pass–rectangular workpiece (b) Circular pass–oval workpiece

Figure 3.15: Examples of neutral lines of pass rolling problems

3.3.3 Bite ability of the rolls

As mentioned earlier, in order to successfully commence the rolling process, the material needs to be bit and pulled into the rolling gap by frictional forces. Otherwise, the surfaces slide and the workpiece becomes stuck, disrupting the continuity of the process. It is crucial for the bite to occur on initial contact, as the conditions grow more favourable as the rolling gap is being filled with material. Bite ability of the rolls depends mainly on friction coefficient and knowledge of it is essential for proper determination of maximum rolling force and optimal reduction plan.

Upon contact, normal force F_n acts in radial direction and frictional force F_f in tangential direction. Their relation may be expressed as

$$F_f = \mu_b \cdot F_n, \tag{3.15}$$

When horizontal components of these forces are in equilibrium:

$$F_{f_z} = F_{n_z} \tag{3.16}$$

$$F_n \cdot \sin(\alpha_0) = F_f \cdot \cos(\alpha_0) \tag{3.17}$$

Using eq. 3.17, friction angle β is defined:

$$tg(\beta) = \frac{F_f}{F_n} = \mu_b, \tag{3.18}$$

For pass rolling problems where initial contact does not occur on the vertical symmetry plain, for example oval pass–rectangular workpiece, radial component of normal force F_{n_r} and bite angle at point of initial contact α_{0_c} are used instead.

Value of bite angle α_0 is obtained from:

$$cos(\alpha_0) = \frac{D - h_0}{2R_{c0}} \quad [12], \tag{3.19}$$

where D stands for roll diameter, i.e. distance between axes of the rolls and R_{c0} for roll radius at initial point of contact.

For roll pass shapes where the initial contact occurs on the symmetry axis, such as circular, R_{c_0} is identical with R_k. If the initial contact occurs anywhere else on the contour of the roll pass groove, more complex calculation is required. For oval roll pass and rectangular workpiece with rounded edges, following system of two equation is used to obtain bite angle α_c and x_c, which stands for distance from symmetry axis to initial contact point (see Fig. 3.17):

$$cos(\alpha_{0_c}) = \frac{D - 2 \cdot [+\sqrt{\bar{r}^2 - (x_c - \bar{\xi})^2}]}{2 \cdot [R_k + \bar{r} - \sqrt{\bar{r}^2 - x_c^2}]} \quad [12], \tag{3.20}$$

$$cos(\alpha_{0_c}) = \frac{(D - 2\cdot) \cdot x_c}{2\{(x_c - \xi) \cdot \sqrt{r^2 - x_c^2} + x_c \cdot [R_k + r - \sqrt{r^2 - x_c^2}]\}} \quad [12], \tag{3.21}$$

where $\bar{r}$ stands for radius of rounded corner of the workpiecee and $\bar{\kappa}$ and $\bar{\xi}$, respectively, for halves of straight parts of workpiece height and width (see Fig. 3.16).
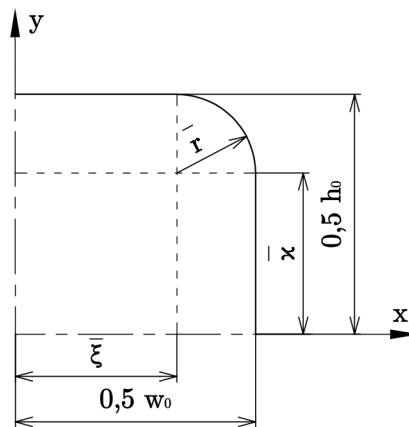

Figure 3.16: Quarter of rectangular cross section of the workpiece [12]

As may be seen on fig. 3.17, Ω stands for normal angle, defined between F_n and F_{n_r}. Its value may be obtained using the following equation:

$$cos(\Omega) = \frac{x \cdot sin(\alpha_{0_c}) + cos(\alpha_{0_c}) \cdot \sqrt{R_{0_c}^2 - z_c^2}}{R_{0_c} \cdot \sqrt{1 + x_c \cdot \sqrt{r^2 + x_c^2}}} \quad [12], \tag{3.22}$$

where z_c stands for position of the initial contact point in rolling direction, acquired from

$$z_c = sin(\alpha_{0_c}) \cdot R_{c0} \quad [12] \tag{3.23}$$
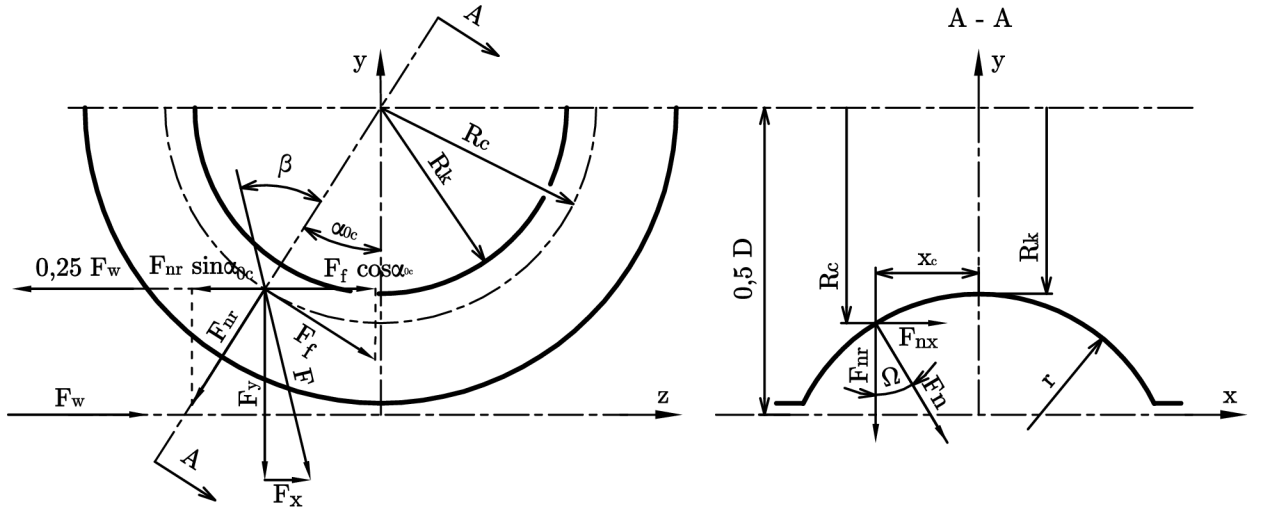

Figure 3.17: Depiction of bite conditions for selected pass rolling problem [12]

For the bite to occur, horizontal component of resulting force F_x must act in rolling direction. Exact expression of this condition depends on the shape of the roll pass. For symmetrical roll passes, where the contact occurs in two locations of the roll pass groove, such as oval pass (see Fig. 3.3.3), the condition is expressed as:

$$F_x = \frac{F_w}{n_c} \cdot \left[\frac{sin(\alpha_{0_c}) \cdot sin(\beta - \alpha_{0_c})}{cos(\Omega)} - sin^2\alpha_{0_c} \right] > 0 \quad [12], \tag{3.24}$$

where F_w stands for total force acting on the workpiece in rolling direction and n_c for number of points of contact on both rolls.

In addition to the first condition, following inequation must be satisfied as well:

$$tg(\beta) > tg(\alpha_0) \cdot tg(\Omega) \quad [12], \tag{3.25}$$

whre β stands for friction angle.

In case of flat rolls or symmetrical roll passes where the initial contact occurs at the top of the roll pass groove, such as circular pass, first condition is defined as:

$$F_x = \frac{F_w}{n} \cdot \frac{tg(\beta) \cdot sin(\alpha_0) \cdot cos\alpha_0)}{cos(\beta)} > 0 \quad [12], \tag{3.26}$$

where $n_c = 2$.

For these roll pass shapes, β must be greater than α_0:

$$\beta \; > \; \alpha_0 \quad [12].\tag{3.27}$$

Knowledge of friction angle β and normal angle Ω is then used to determine the value of maximum bite angle $\alpha_{0_{max}}$ at which both necessary conditions are still satisfied.

3.3.4 Maximum height reduction

Using previously acquired values, maximum height reduction of the workpiece Δh_{max} may obtained from:

$$\Delta h_{max} = 2R \cdot [1 - cos(arctg\frac{\mu_f}{cos\,(\Omega)})] \quad [12],\tag{3.28}$$

where R stands for roll diameter at position of maximum height reduction.

Subsequently, value of Δh_{max} is used to determine limit rolling force.

3.3.5 Rolling force

Rolling force F_{roll} is the vertical component of reaction force generated by contact of the workpiece and rolls. When using analytical approach, it is defined as sum of vertical components of local tangential and normal deformation resistances on the contact surface. In case that only lagging and leading zone is considered, as was depicted on Fig. 3.8, value of F_{roll} is acquired from:

$$F_{roll} = \int\int_{S_{lag}} \frac{q_{lag} \cdot R_c \cdot \sqrt{1 + \left(\frac{\mathrm{d}R_c}{dz}\right)^2}}{\sqrt{R_c^2 - z_c^2}} \mathrm{d}x\mathrm{d}z + \int\int_{S_{lead}} \frac{q_{lead} \cdot R_c \cdot \sqrt{1 + \left(\frac{\mathrm{d}R_c}{dz}\right)^2}}{\sqrt{R_c^2 - z_c^2}} \mathrm{d}x\mathrm{d}z \quad [12],\tag{3.29}$$

,

where q_{lag} and q_{lead} stand for vertical components of deformation resistances on the contact surfaces and S_{lag} and S_{lead} for horizontal projections of contact surfaces of respective zones.

For majority of practical applications, however, empirical and experimental approach is preferred. Multiple methods and formulas were devised, each of them using the following formula:

$$F_{roll} = \sigma_{nm} \cdot Q_{F_{roll}} \cdot S_h \quad [12],\tag{3.30}$$

where σ_{nm} stands for mean natural deformation resistance, $Q_{F_{roll}}$ for mean forming factor and S_h for area of horizontal projection of contact surface.

Natural deformation resistance σ_n describes the material's resistance against deformation in case of monotonous uniaxial loading and depends on rolling temperature T_r, strain ε and strain rate $\dot{\varepsilon}$. In case of cyclic loading, loading history must be respected as well. Due to all of these parameters varying throughout the rolling gap, $\sigma_n m$ assumes different values. Since natural deformation resistance σ_n is identical with equivalent stress $\bar{\sigma}$ (defined later in Sec. 4.1.1), its mean value σ_{nm} may be acquired from:

$$\sigma_{nm} = \frac{1}{S} \int_0^S \bar{\sigma}(S) \cdot \mathrm{d}S \quad [12].$$
(3.31)

Equivalent stress is acquired from tensile, compressive or torsion tests, conducted at reference temperature and strain rate. To correspond with conditions present during specific rolling process, its value is multiplied using various correction coefficients [12].

Forming factor Q_{F_v} respresents the effect of stress state at contact surface. In case of monotonous uniaxial loading, it assumes value of 1. Value of Q_{F_v} depends on geometry and deformation of the workpiece and friction on the contact surface. In flat rolling, its value may be obtained through a vast amount of theoretical or empirical methods. Due to more complex geometry in pass rolling, theoretical methods would be barely usable. Instead, multiple empirical flat rolling methods were corrected for various roll pass shapes, such as the following formula:

$$Q_{F_{roll}} = K_Q \cdot \left(A_Q + B_Q \cdot \frac{\sqrt{R_m \cdot \Delta h}}{0.5 \cdot (h_0 + h_1)} + C_Q \cdot \frac{0.5 \cdot (h_0 + h_1)}{\sqrt{R_m \cdot \Delta h}} \right) - (K_Q - 1) \quad [12], \quad (3.32)$$

where K_Q, A_Q, B_Q and C_Q stand for empirical correction coefficients for specific shapes of rolls and workpiece.

Area of horizontal projection of contact surface S_h, which is obviously more complex in case of pass rolling, may also be obtained by by multiple theoretical and experimental methods. One such method usable for various shapes of workpiece and rolls, fairly corresponding with experimental results was proposed in [13]. For oval pass and circular workpiece, S_h is acquired from:

$$S_h = G \cdot (w_{0_{max}} + w_{1_{max}}) \cdot \sqrt{R_k \cdot \Delta h} \quad [13],$$
(3.33)

where G stands for geometric correction coefficient.

For circular pass and oval workpiece, S is obtained from:

$$S_h = G \cdot w_{1_{max}} \cdot \sqrt{R_k \cdot \Delta h} \quad [13],$$
(3.34)

4 Material behavior

The purpose of the following chapter is to describe plasticity phenomenon and its use in finite element software Abaqus. A brief overview of constitutive models of plasticity is included as well. Final part of the chapter deals with damage criteria used to simulate ductile fracture propagation and assessment of material formability.

4.1 Incremental plasticity theory

Since plasticity is a non–conservative process, final values are dependent on the whole loading history, composed of individual load increments. Incremental plasticity theory is crucial for correct modelling of elastic–plastic response of the material. It consists of three separate characteristics which need to be defined for plastic constitutive models, those being yield criterion, flow rule and hardening.

4.1.1 Yield criterion

Yield criterion defines the stress state of the material at which yielding commences, with the material transitioning from elastic to elastic–plastic behavior. This thesis deals exclusively with Von Mises yield criterion, which uses Von Mises equivalent stress $\bar{\sigma}$, sometimes known as Von Mises stress intensity. For the rest of the thesis, it will be denoted only as equivalent stress. $\bar{\sigma}$ is defined as:

$$\bar{\sigma} = q = \sqrt{\frac{3}{2}(\mathbf{S} : \mathbf{S})} = \sqrt{\frac{3}{2}(S_{ij}S_{ij})} \quad [14],\tag{4.1}$$

where $\mathbf{S}$ stands for deviatoric stress tensor and S_{ij} for its components. Operator ":" means double dot product of two second–order tensors, result of which is a scalar.

Stress tensor $\boldsymbol{\sigma}$ (its components are denoted as σ_{ij} or σ_{11} to σ_{33}) may be expressed as a sum of $\mathbf{S}$, which alters the shape and volumetric component, which causes a change of volume of the stressed body [14]. $\mathbf{S}$ is then obtained by subtracting the volumetric component from $\boldsymbol{\sigma}$:

$$\mathbf{S} = \boldsymbol{\sigma} - \sigma_h \cdot \mathbf{I} \quad [15],\tag{4.2}$$

where σ_h stands for hydrostatic stress and $\mathbf{I}$ for unit matrix.

Hydrostatic stress, which is equal to negative value of pressure p_σ, defines volumetric component of stress tensor and is obtained from:

$$\sigma_h = -p_\sigma = \frac{\sigma_{11} + \sigma_{22} + \sigma_{33}}{3} \quad [14].\tag{4.3}$$

When using components of the stress tensor, $\bar{\sigma}$ is obtained from:

$$\bar{\sigma} = \frac{\sqrt{2}}{2} \cdot \sqrt{(\sigma_{11} - \sigma_{22})^2 + (\sigma_{22} - \sigma_{33})^2 + (\sigma_{11} - \sigma_{33})^2 + 6 \cdot (\sigma_{12}^2 + \sigma_{23}^2 + \sigma_{13}^2)} \quad [14].\tag{4.4}$$

For principal stresses $\sigma_1 \geq \sigma_2 \geq \sigma_3$, following equation is used:

$$\bar{\sigma} = \frac{\sqrt{2}}{2} \cdot \sqrt{(\sigma_1 - \sigma_2)^2 + (\sigma_2 - \sigma_3)^2 + (\sigma_1 - \sigma_3)^2} \quad [14]. \tag{4.5}$$

Third invariant of the stress tensor r_σ, used later in Sec. 4.3, is defined as:

$$r_\sigma = \sqrt[3]{\frac{27}{2}(\sigma_{11} - \sigma_h) \cdot (\sigma_{22} - \sigma_h) \cdot (\sigma_{33} - \sigma_h)} \quad [14]. \tag{4.6}$$

In Haigh stress space (where the three axes represent the principal stresses), von Mises yield surface takes on a shape of a cylinder with the axis along the hydrostatic line, where all principal stresses are equal (see Fig. 4.1).
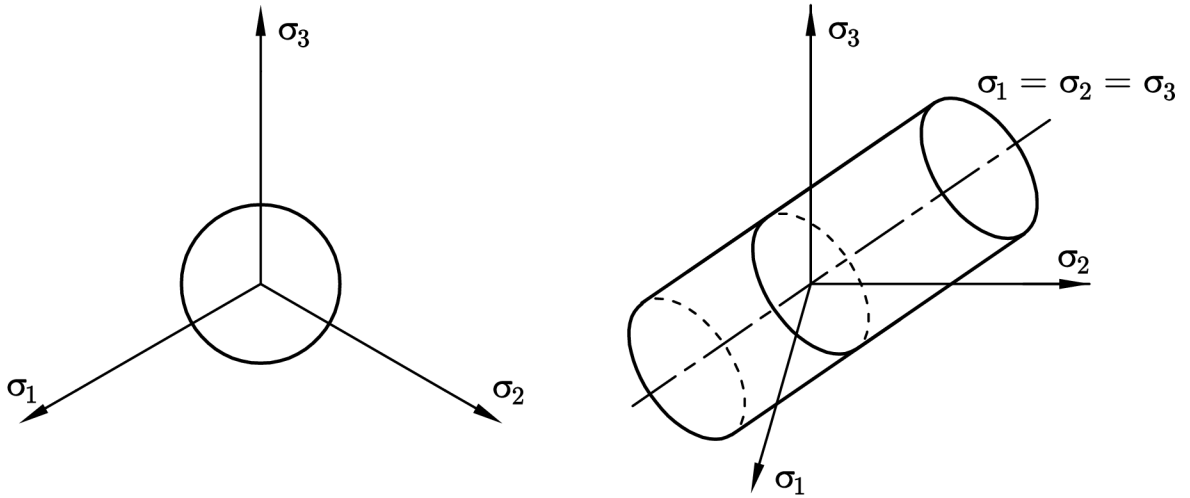

Figure 4.1: Depiction of von Mises yield surface in Haigh space

The criterion is defined as:

$$f(\sigma, \sigma_y) = \bar{\sigma} - \sigma_y = 0 \quad [16], \tag{4.7}$$

where σ_y stands for yield stress.

Inside the yield surface, where $f(\sigma) < 0$ is true, stress states result in elastic deformation. Yielding commences when yield surface is reached, with further loading causing plastic deformation. Since stresses do not exist outside yield surface, its shape evolves and maintains the stresses either inside or on the yield surface [16, 17]. Possible evolution of yield surface is further explained in Sec. 4.1.3.

4.1.2 Flow rule

Flow rule defines evolution of plastic strain by defining the dependency of plastic strain increment on stress increment:

$$d\varepsilon_{p_{ij}} = d\lambda \cdot \left(\frac{\partial Q}{\partial \sigma_{ij}}\right) \quad [18], \tag{4.8}$$

where $d\varepsilon_{p_{ij}}$ stands for increment of plastic strain, $d\lambda$ for plastic multiplier and Q for plastic potential.

When plastic strain increment is normal to the yield surface, which is represented by Q, the flow rule of the model is called associated. When associated flow rule is used, principal directions of plastic strain increment and deviatoric stress tensor are identical and plastic strain increment proportional to stress increment is assigned. Associated flow rules are usually used for modelling of metal behavior [17].

4.1.3 Hardening rule

Hardening rule defines the evolution of yield surface during plastic deformation. Except ideal plastic material, yielding always results in hardening, i.e. an increase in yield stress caused by further loading from the stress state at the yield surface, accompanied by increase of plastic strain.

Multiple types of hardening rules are distinguished [16, 17]:

- Isotropic - plastic deformation causes the yield surface to uniformly increase. This hardening rule may be used to properly model behavior of material under monotonous loading, but should not be used in case of cyclic loading.

- Kinematic - instead of increasing its size, plastic deformation causes the center of the yield surface to move in the loading direction. Being able to capture Bauschinger effect - a phenomenon of compressive yield strength reduction as a result of tensile loading - this hardening rule is a viable choice for modelling of material subjected to cyclic loading.

- Combined - various materials exhibit a combination of both previously mentioned hardening rules, which may both be combined to obtain a new hardening model. Change of shape of the yield surface or strain softening may also be captured by a variety of additional hardening models.
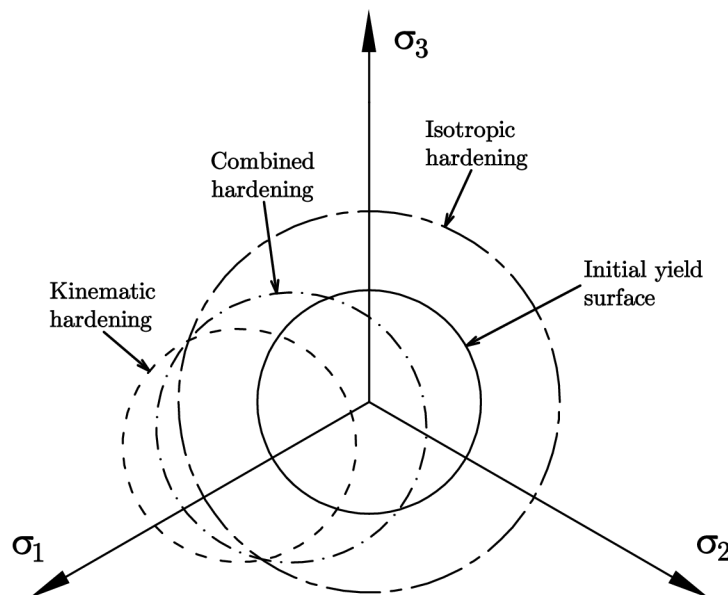

Figure 4.2: Basic hardening types

4.2 Constitutive models of material

In elastic–plastic models, total strain is decomposed into elastic and plastic components, with each being assigned a separate constitutive model.

Isotropic elastic model, used for the elastic component, is defined by two independent variables, usually Young's modulus E and Poisson's ratio ν. Notable temperature dependency of E, which may be seen on Fig. 4.3, needs to be taken into account when elevated temperatures are present in the analysis.
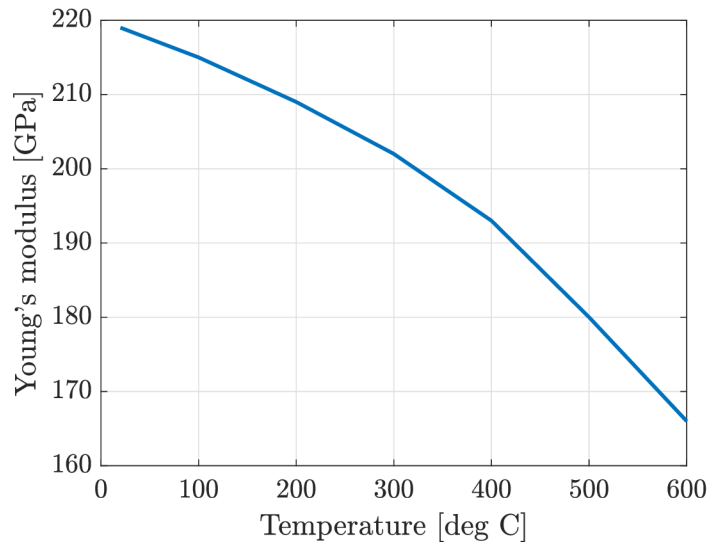

Figure 4.3: An example of Young's modulus temperature dependency [19]

Due to high temperatures throughout whole process, material is almost always in plastic state, with values of elastic strain insignificant when compared to their much more prominent plastic counterpart. Below lies an overview of some of constitutive models that may be used for modelling of plastic behavior of the materials.

4.2.1 Mises Isotropic plasticity model

Mises plasticity with isotropic hardening is defined by a yield stress versus equivalent plastic strain table, forming a flow curve. True stress σ_{true} and strain ε_{true} values (associated with actual cross–sectional area) are required to define the flow curve. Since engineering stress σ_{eng} and strain ε_{eng} values (associated with initial cross–sectional area) are usually obtained from uniaxial tensile test, a transformation is necessary [16]:

- $\varepsilon_{true} = \ln(1 + \varepsilon_{eng})$

- $\sigma_{true} = \sigma_{eng} \cdot (1 + \varepsilon_{eng})$

Influence of strain rate and temperature may be included by defining a flow curve obtained from a test at specified constant values of strain rate and temperature (see Fig. 4.4). Additionaly, strain rate dependency may be included by defining multiple flow curves for various equivalent strain rate values, representing tests carried out at different load rates. Similarly, temperature dependency may be defined. Proper yield stress values are then interpolated from these tables.
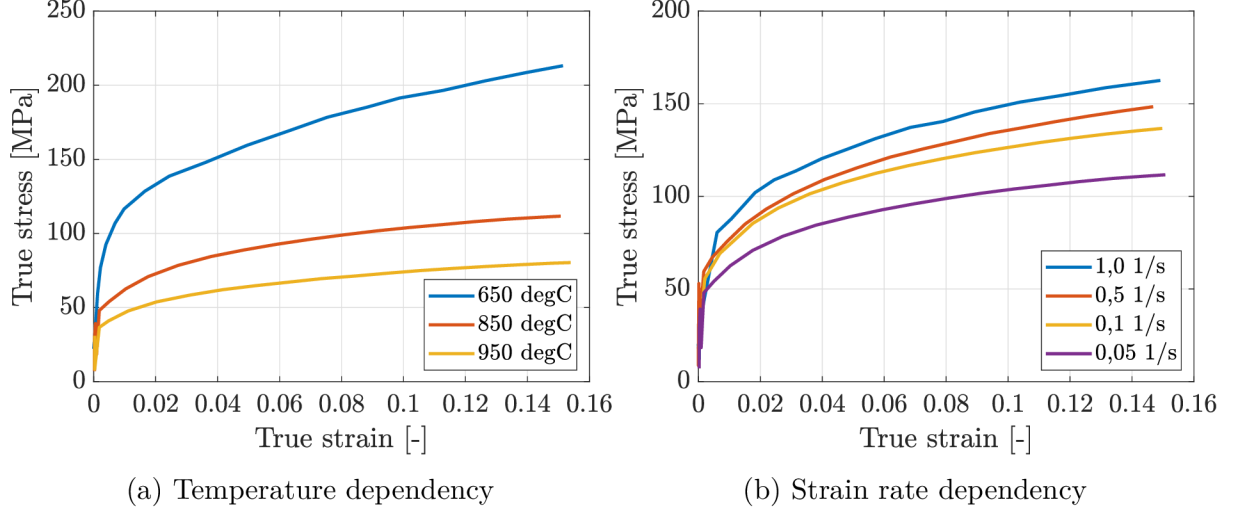
(a) Temperature dependency

(b) Strain rate dependency

Figure 4.4: Flow curves at various temperatures and strain rates [20]

4.2.2 Johnson–Cook plasticity

Johnson–Cook isotropic plasticity is widely used due to its strain rate and temperature dependency as well as simple implementation and usage in Abaqus environment. It also uses Mises yield criterion [21].

The flow curve is defined by the following equation:

$$\bar{\sigma} = [\sigma_y + K^{JC} \cdot (\bar{\varepsilon}_p)^{n^{JC}}] \cdot [1 + C^{JC} \cdot \ln(\dot{\varepsilon}_p^*)] \cdot [1 - (T^*)^{m^{JC}}] \quad [21], \tag{4.9}$$

where $\dot{\varepsilon}_p^*$ stands for dimensionless plastic strain rate, T^* for homologous temperature and K^{JC}, C^{JC}, n^{JC} and m^{JC} for Johnson–Cook plasticity parameters.

Starting from the left, terms in brackets define the flow curve, strain rate dependence and temperature dependence. Parameters defining rate and temperature dependency are independent on the each other, meaning that both dependecies do not need to be defined for the model to be used.

Homologous temperature assumes different values for following intervals, where T stands for actual temperature, T_{ref} for reference temperature (usually room temperature) and T_m for melting temperature:

- 0 for $T < T_{ref}$, where no temperature dependency is defined.

- $\frac{T - T_{ref}}{T_m - T_{ref}}$ for $T_{ref} \leq T \leq T_m$, where temperature dependency is defined.

- 1 for $T > T_m$, where the material starts to behave like an ideal fluid.

Dimensionless plastic strain rate is defined as:

$$\dot{\varepsilon}_p^* = \frac{\dot{\bar{\varepsilon}}_p}{\dot{\bar{\varepsilon}}_{p_0}} \quad [21], \tag{4.10}$$

where $\dot{\bar{\varepsilon}}_p$ stands for equivalent plastic strain rate and $\dot{\bar{\varepsilon}}_{p_0}$ for reference equivalent plastic strain rate.

4.3 Material damage

Assessment of material formability as well as simulation of ductile damage propagation may be carried out with the explicit algorithm using various damage criteria. For all criteria mentioned in this thesis, damage initiation occurs when equivalent plastic strain $\bar{\varepsilon}_p$ reaches its limit value $\bar{\varepsilon}_p^f$, called equivalent plastic strain at fracture, where the material is not capable of further plastic deformation [15].

This thesis deals exclusively with Von Mises equivalent plastic strain $\bar{\varepsilon}_p$, sometimes known as plastic strain intensity. In this thesis, it will be further denoted only as equivalent plastic strain. It is defined similarly to Von Mises equivalent stress. This time, however, two separate variables need to be distinguished. First of those is actual equivalent plastic strain $\bar{\varepsilon}_p^{act}$, obtained from plastic strain tensor:

$$\bar{\varepsilon}_p^{act} = \sqrt{\frac{2}{3}(\boldsymbol{\varepsilon}_p : \boldsymbol{\varepsilon}_p)} = \sqrt{\frac{2}{3}(\varepsilon_{pij}\varepsilon_{pij})} \quad [21], \tag{4.11}$$

where $\boldsymbol{\varepsilon}_p$ stands for plastic strain tensor and ε_{pij} for its components.

When components of the strain tensor are used, $\bar{\varepsilon}_p^{act}$ is acquired from:

$$\bar{\varepsilon}_p^{act} = \frac{\sqrt{2}}{3} \cdot \sqrt{(\varepsilon_{p11} - \varepsilon_{p22})^2 + (\varepsilon_{p22} - \varepsilon_{p33})^2 + (\varepsilon_{p11} - \varepsilon_{p33})^2 + 6 \cdot \left(\varepsilon_{p12}^2 + \varepsilon_{p23}^2 + \varepsilon_{p13}^2\right)} \tag{4.12}$$

In case of principal strains $\varepsilon_1 \geq \varepsilon_2 \geq \varepsilon_3$, ε_p^{act} is defined as:

$$\bar{\varepsilon}_p^{act} = \frac{\sqrt{2}}{3} \cdot \sqrt{(\varepsilon_{p1} - \varepsilon_{p2})^2 + (\varepsilon_{p2} - \varepsilon_{p3})^2 + (\varepsilon_{p1} - \varepsilon_{p3})^2} \tag{4.13}$$

The other of the two mentioned variables is cumulative equivalent plastic strain $\bar{\varepsilon}_p^{cum}$:

$$\bar{\varepsilon}_p^{cum} = \int_0^{t_a} \sqrt{\frac{2}{3}(\dot{\boldsymbol{\varepsilon}}_p : \dot{\boldsymbol{\varepsilon}}_p)}\mathrm{d}t \quad [21], \tag{4.14}$$

where stands for $\dot{\boldsymbol{\varepsilon}}_p$ plastic strain rate tensor and t_a for the duration of analysis.

Depending on used criterion, $\bar{\varepsilon}_p^f$ is defined as a function of one or more variables. The first of these is the stress triaxiality factor η, sometimes referred to as stress state index (particularly in literature regarding technology), which is defined by either of the two following equations:

$$\eta = \frac{\sigma_h}{\bar{\sigma}} = -\frac{p_\sigma}{q_\sigma} \quad [16] \tag{4.15}$$

Some of the more complex models also utilize Lode angle θ, defined either as:

$$\theta = tan^{-1}\left(\frac{\mu}{\sqrt{3}}\right) \quad \text{or} \quad \theta = -\frac{1}{3} \cdot sin^{-1}(\xi) \quad [16], \tag{4.16}$$

where μ stands for Lode parameter:

$$\mu = \frac{2 \cdot \sigma_1 - \sigma_3}{\sigma_1 - \sigma_3}, \tag{4.17}$$

and ξ for normalized third invariant of stress tensor:

$$\xi = \left(\frac{r_\sigma}{q}\right)^3 \tag{4.18}$$

Unlike μ and ξ, which assume values from interval $-1 \leq \mu, \xi \leq 1$, θ assumes values from $-\frac{\pi}{6} \leq \mu, \xi \leq \frac{\pi}{6}$ and is often normalized:

$$\bar{\theta} = -\frac{60}{\pi}, \tag{4.19}$$

where $\bar{\theta}$ stands for normalized Lode angle.

These parameters assume equal values for the following stress states:

- 1, $\frac{60}{\pi}$ for axisymmetric tension

- 0 for plane strain or pure shear

- -1, $-\frac{60}{\pi}$ for axisymmetric compression

4.3.1 Ductile damage mechanisms

Depending on the load type and stress state of the material, two separate ductile damage mechanisms are distinguished [15]:

- Cavity mechanism - typical for tensile loading (high triaxiality values), it is based on pooling (coalescence) of minor voids that form on the interface of the material and foreign particles, resulting in macroscopic crack intiation.

- Shear mechanism - commonly associated with compressive loading (low triaxiality values), crack initiation and propagation occurs in plane of maximum shear stress.

4.3.2 Ductile damage criteria

For each of the criteria introduced in this section, damage initiation occurs when the following condition is satisfied:

$$\omega_D = \int \frac{\mathrm{d}\bar{\varepsilon}_p}{\bar{\varepsilon}_p^f} = 1 \quad [21], \tag{4.20}$$

where ω_D stands for value of damage criterion.

ω_D accumulates with plastic strain and its increase at each increment $\Delta\omega_D$ is acquired from:

$$\Delta\omega_D = \frac{\Delta\bar{\varepsilon}_p}{\bar{\varepsilon}_p^f} \geq 0 \quad [21], \tag{4.21}$$

where $\Delta\bar{\varepsilon}_p$ stands for incremental increase of equivalent plastic strain.

The difference between individual criteria lies in definition of $\bar{\varepsilon}_p^f$, which is obtained from a specific equation and is dependent on some of the previously mentioned variables.

Simulation of ductile fracture propagation is carried out through element deletion. Stiffness of the elements is progressively degraded and when used criterion is met and damage initiation occurs, they are removed from the analysis [21].

Ductile criterion

Equivalent plastic strain at fracture for ductile criterion $\bar{\varepsilon}_f^{pD}(\eta, T, \dot{\bar{\varepsilon}})$ is defined through a table of fracture plastic strain values dependent on stress triaxiality factor, an example of which may be seen on Fig. 4.5. Optionally, strain rate and temperature dependency may be included by input of multiple curves, similar to Mises plasticity.
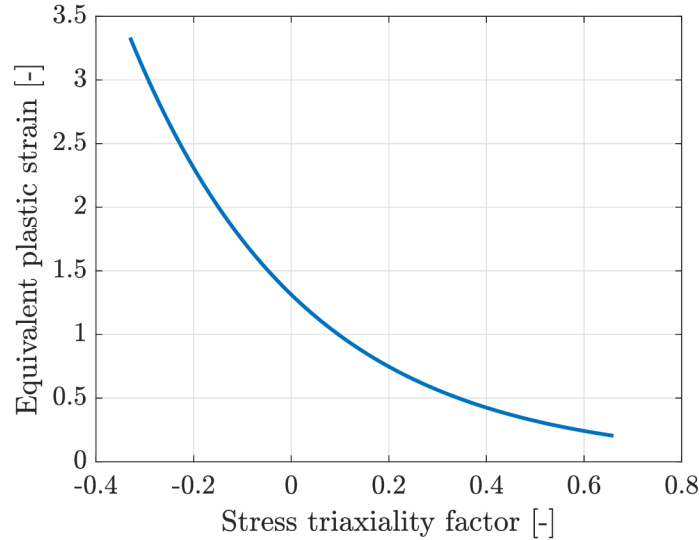

Figure 4.5: Fracture curve of stainless steel ČSN 41 7246 [22]

In [22], the curve was obtained from the following equation:

$$\bar{\varepsilon}_f^{pD}(\eta, T, \dot{\bar{\varepsilon}}) = K_1 \cdot e^{-K_2 \cdot \eta} \quad [22], \tag{4.22}$$

where K_1 and K_2 stand for material formability coefficients for specific thermodynamical conditions.

Johnson–Cook criterion

Fracture plastic strain for Johnson–Cook criterion $\bar{\varepsilon}_D^{pJC}$ is defined as:

$$\bar{\varepsilon}_D^{pJC}(\eta, T^*, \dot{\bar{\varepsilon}}) = \left[d_1^{JC} + d_2^{JC} \cdot e^{-d_3^{JC} \cdot \eta}\right] \cdot \left[1 + d_4^{JC} \cdot \ln(\dot{\varepsilon}_p^*)\right] \cdot \left[1 + d_5^{JC} \cdot T^*\right] \quad [21], \tag{4.23}$$

where d_1^{JC} to d_5^{JC} stand for Johnson–Cook damage parameters.

Johnson–Cook criterion provides fracture surface similar to ductile criterion (see Fig. 4.5), but its definition by mentioned material parameters may be more convenient for the user.

Xue–Wierzbicki criterion

Unlike previously discussed criteria, which are implemented in Abaqus, Xue–Wierzbicki criterion requires to be programmed through user subroutine. It belongs among more advanced criteria and in addition to stress triaxiality factor η, it is a function of normalized third invariant of stress tensor ξ [15].

Dor Xue–Wierzbicki criterion, $\bar{\varepsilon}_p^{fXW}(\eta,\xi)$ is defined as:

$$\bar{\varepsilon}_p^{fXW}(\eta,\xi) = d_1^{XW} \cdot e^{-d_2^{XW}\cdot\eta} - \left[d_1^{XW} \cdot e^{-d_2^{XW}\cdot\eta} - d_3^{XW} \cdot e^{-d_4^{XW}\cdot\eta} \right] \cdot \left[1 - \eta^{\frac{1}{n}} \right]^n \quad [23], \quad (4.24)$$

where d_1^{XW} to d_4^{XW} stand for Xue–Wierzbicki damage parameters and n stands for exponent of hardening.

Fracture strain is based on eliptical function on the ξ - $\bar{\varepsilon}_p^f$ plane, respecting the impact of different stress states. On the η - $\bar{\varepsilon}^f$ plane, exponential function is used, similar to Johnson–Cook criterion [15]. An example of Xue–Wierzbicki fracture envelope may be seen on Fig. 4.6.
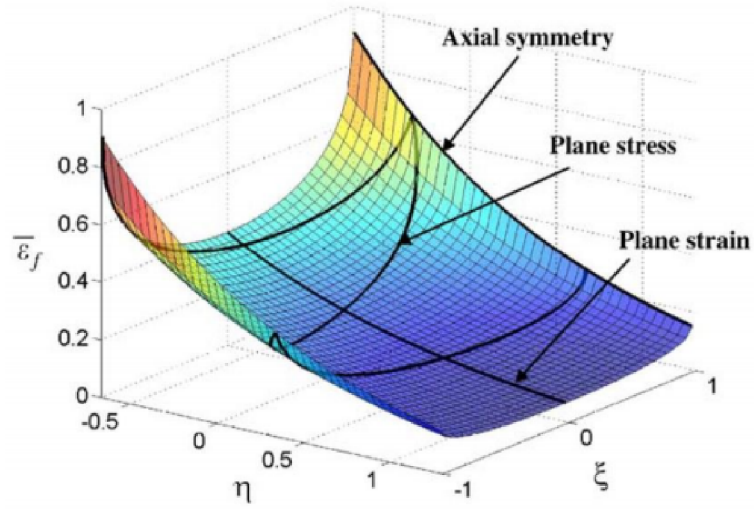

Figure 4.6: Xue-Wierbiczki fracture envelope [23]

5 Finite element method

Finite Element Method is a numerical tool used to solve a wide variety of analyses, such as structural, thermal, modal, electromagnetic or heat transfer. This chapter is focused mainly on its explicit formulation, which is used in all analyses carried out in the thesis. A description of simplified pass rolling analysis carried out in [22] forms the end of the chapter.

5.1 Lagrange's variational principle

FEM belongs among variational methods, which are based on variational principles. According to PETRUŠKA (2011, p. 8), Langrange's variational principle, on which FEM is based, may be interpreted as: „*Of all deformation functions which preserve the integrity of the structure and satisfy all geometric boundary conditions, those are utilized, which bestow stationary value to total potential energy, which also acts as its minimal value.*" Potential energy Π is defined as:

$$\Pi = W - P \quad [24],$$ (5.1)

where W stands for strain energy, acquired from

$$W = \frac{1}{2} \int_{\Omega} \boldsymbol{\sigma}^{\mathrm{T}} \boldsymbol{\varepsilon}^{\mathrm{T}} \, \mathrm{d}V \quad [24]$$ (5.2)

where $\boldsymbol{\sigma}^{\mathrm{T}}$ stands for stress vector, $\boldsymbol{\varepsilon}^{\mathrm{T}}$ for strain vector and P for external load potential, defined as:

$$P = \int_{\Omega} \mathbf{u}^{\mathrm{T}} \mathbf{o}^{\mathrm{T}} \, \mathrm{d}V + \int_{\Gamma_P} \mathbf{u}^{\mathrm{T}} \mathbf{p}^{\mathrm{T}} \, \mathrm{d}S \quad [24],$$ (5.3)

where $\mathbf{u}^{\mathrm{T}}$ stands for displacement vector, $\mathbf{o}^{\mathrm{T}}$ for body force vector and $\mathbf{p}^{\mathrm{T}}$ for surface force vector .

5.2 Explicit finite element method

Explicit finite element method was developed to solve quick, dynamic problems, such as projectile impacts, crash tests or explosions, which were difficult or unable to be solved with the traditional, implicit method. Explicit FEM is also capable of handling all types of nonlinearities well. Nowadays, it is used for a variety of problems, such as complex contact problems, nonlinear buckling problems, nonlinear quasi–static problems or problems involving material damage.

Explicit algorithm is based on following equation of motion defined at time t:

$$\mathbf{M} \cdot \ddot{\mathbf{U}}_t + \mathbf{B} \cdot \dot{\mathbf{U}}_t + \mathbf{F}_t^{int} = \mathbf{F}_t^{ext} \quad [24],$$ (5.4)

where $\mathbf{M}$ stands for global mass matrix, $\ddot{\mathbf{U}}_t$ for nodal acceleration matrix, $\mathbf{B}$ for global damping matrix, $\dot{\mathbf{U}}_t$ for nodal velocity matrix, $\mathbf{F}_t^{int}$ for internal forces matrix and $\mathbf{F}_t^{ext}$ for external forces matrix.

This equation represents a time-dependent system of nonlinear differential equations. Since no analytical solution is available, it has to be solved numerically. Explicit solvers employ central difference method, which calculates nodal displacement, velocity and acceleration values at time moment $t + \Delta t$ from equation of motion defined at previous time moment t, opposed to implicit algorithm, where all values at time moment $t + \Delta t$ are evaluated from equation of motion defined at the same time moment. To prevent errors, short time steps are used with explicit algorithm [24, 25].

Dynamic equation is expressed as Second Newton's law in matrix form, defined at moment t:

$$\ddot{\mathbf{U}}_t = \mathbf{M}^{-1} \cdot \left(\mathbf{F}_t^{ext} - \mathbf{F}_t^{int} \right) \quad [24]. \tag{5.5}$$

Velocity values at $t + \frac{\Delta t}{2}$ are obtained from:

$$\dot{\mathbf{U}}_{t+\frac{\Delta t}{2}} = \dot{\mathbf{U}}_{t-\frac{\Delta t}{2}} + \frac{\Delta t_t + \Delta t_{t+\Delta t}}{2} \cdot \ddot{\mathbf{U}}_t \quad [25], \tag{5.6}$$

where $\dot{\mathbf{U}}_{t+\frac{\Delta t}{2}}$ stands for nodal velocity matrix at $t + \frac{\Delta t}{2}$, $\dot{\mathbf{U}}_{t-\frac{\Delta t}{2}}$ for nodal velocity matrix at $t - \frac{\Delta t}{2}$ and $\ddot{\mathbf{U}}_t$ for nodal acceleration matrix at t.

Subsequently, displacement values at $t + \Delta t$ are obtained:

$$\mathbf{U}_{t+\Delta t} = \mathbf{U}_t + \Delta t_{t+\Delta t} \cdot \dot{\mathbf{U}}_{t+\frac{\Delta t}{2}} \quad [25], \tag{5.7}$$

where $\mathbf{U}_{t+\Delta t}$ stands for nodal displacement matrix at $t+\Delta t$, $\mathbf{U}_t$ for nodal displacement matrix at t and $\mathbf{U}_{t+\frac{\Delta t}{2}}$ for nodal displacement matrix at $t + \frac{\Delta t}{2}$.

Nodal displacement values obtained in each step are added to initial geometric configuration, forming new geometric configuration:

$$X_{t+\Delta t} = X_t + \mathbf{U}_{t+\Delta t}, \tag{5.8}$$

where $X_{t+\Delta t}$ stands for deformed geometry at $t + \Delta t$ and X_t for geometry at t.

Subsequently, aquired values of nodal displacement are used to obtain strain and then stress values. The process of stress calculation and formation of new geometric configurations is repeated for as many iterations as required to reach the end time of the load step.

Since mass matrix used in explicit algorithm is diagonal, the system is decomposed into equations. Desired results are obtained by separately solving these, as opposed to implicit algorithm, where global stiffness matrix formation and inversion are required. Since these operations consume notable portion of the computing time, time step is much longer than it would be in explicit algorithm [24, 25].

5.2.1 Critical time step length

Conditional stability is a substantial feature of explicit algorithm. It means that stable, reliable results are obtained if time step length Δt does not surpass critical time step length Δt^{crit}:

$$\Delta t \leq \Delta t^{crit} \quad [21]. \tag{5.9}$$

This condition requires that the time step length be lower than the time required for the stress wave to propagate through the characteristic dimension of the smallest element in the model. [25].

Critical time step length is given by:

$$\Delta t^{crit} = \frac{2}{\omega_{max}}, \tag{5.10}$$

where ω_{max} stands for maximum eigenfrequency of the smallest element of the model, acquired from:

$$\omega_{max} = \frac{2c}{l_{char}}, \tag{5.11}$$

where l_{char} stands for characteristic dimension of the smallest element of the model and c_v for the velocity of stress wave propagation throughout the material, given by

$$c_v = \sqrt{\frac{E}{\rho}}, \tag{5.12}$$

where E stands for Young's modulus and ρ for density of the material.

In Abaqus, time step length may be either provided directly by the user or determined by the program itself. In the latter case, critical time step of every element present in the model is determined. The lowest of them is further reduced (usually by 10 %) in order to safely satisfy the stability condition. Due to deformation of the smallest element, critical time step length may vary throughout the process [25].

As implied by the information above, time step length and overall computing time depend on the characteristic dimension of the smallest element present in the model. This means that if an otherwise coarse mesh contains a single small element, time step length and overall computing time will be the same as if it consisted solely of these small elements. This suggests that when using the explicit algorithm, optimal finite element mesh should be as homogenous as possible, as opposed to implicit algorithm, where computing time depends mainly on the number of elements [21, 25].

5.2.2 Mass scaling

As seen in eq. 5.12, critical time step length depends on Young's modulus and density of the material. This means that overall computing time may be reduced by artificially changing values of either of the two parameters. Tampering with value of Young's modulus, however, might drastically influence material response and render the results of the analysis useless. Increasing the density of material, on the other hand, is a method often employed in explicit analyses. It may either be realized manually, or using a function called mass scaling.

Abaqus computing environment, for instance, offers a wide variety of mass scaling methods, most of them under semi–automatic mass scaling option. The user may either specify scaling factors, which are then applied on the model, or directly specify desired time step length, which the program achieves by applying appropriate scaling factors. If the specified scaling factor is too high or desired time step is too short, the increase of the mass of the model and corresponding changes of inertial forces may affect the results of the analysis. In opposite case, while the results are not affected, the usage of mass scaling results in little to no reduction of the computing time.

Time step value may be either determined only at the start and kept throughout whole analysis (fixed mass scaling), or at the start and subsequently evaluated at specified intervals (variable mass scaling). The latter option requires more computing time, but is useful when scaled elements undergo deformations which alter their characteristic dimensions. User may also decide whether to apply mass scaling globally, or just on a specified part of the model.

Mass scaling is most efficient in quasi static problems, where inertial forces may be neglected. Commonly, problems are considered quasi-static if kinetic energy values are lower than 10 % of total strain energy. In this case, mass scaling affects the results only when enormous mass increase is present. This is accompanied by generation of large amounts of kinetic energy, surpassing the mentioned quasi–static threshold. In case of dynamic analyses, where inertial forces are play a substantial role, much more caution is advised for the user, as even a little increase of the mass of the model may result in obtaining incorrect results [25, 26].

Automatic mass scaling

Another option offered by Abaqus is automatic mass scaling, which is intended specifically for bulk metal rolling analyses. This method automatically determines appropriate scaling factors based on several parameters of the rolling process provided by the user [21]:

- l_e - average element length in rolling direction.

- R_{feed} - feed rate, defined as average velocity of the workpiece in rolling direction

- n_n - number of nodes in cross section of the workpiece

It is recommended that the workpiece be meshed by sweeping the mesh of the cross section along its length. Also, the length of the elements in the rolling direction should not vary significantly and should be similar to element size in the cross section [21].

5.2.3 Reduced integration

Linear elements with reduced (single point) integration are used in vast majority of explicit analyses. It means that the elements used in analysis contain a single integration point (Gauss point) located at its center, where all energy, stress and strain values are evaluated. The advantage of reduced integration is reduction of computing time, but comes at a cost of lower numerical stability. This problem manifests when an element is deformed symmetrically around its integration point, as no strain energy is associated with the deformation (see Fig. 5.1). Since the geometry is altered in process, this is considered unrealistic behavior, as no deformation is possible without generating a certain amount of strain energy [25].
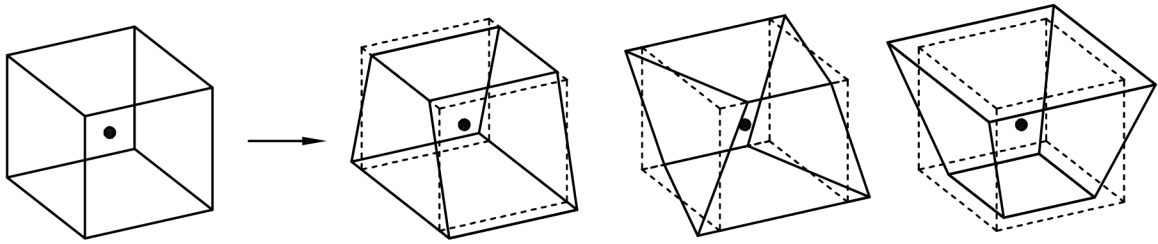
Figure 5.1: Hourglassing deformation modes [25]

This phenomenon is called hourglassing, due to a characteristic zig–zag deformation pattern, its shape similar to that of a hourglass. Presence of hourglassing impacts the results of the analysis, possibly rendering them useless or even causing the analysis to fail. Severity of hourglassing may be evaluated by measuring its energy, also called artificial strain energy. In order to obtain credible results, artificial strain energy should not pass 5 % of the total strain energy of the model [25].

Impact of hourglassing may be reduced by refining the mesh, which obviously results in higher computational time. Usage of point loads may also result in hourglassing occurence, and should be avoided at all costs [21, 25].

To completely avoid hourglassing problem, fully integrated linear elements may be used in the analysis. However, in addition to higher computational time, fully integrated elements are also associated with the problem of shear locking. When subjected to pure bending (see Fig. 5.2), these elements, being linear, are not capable of bending deformation. Shear deformation occurs instead, generating shear stress. Due to this, bending stiffness of the elements is increased, leading to notably reduced deformation in bending problems, obtaining inaccurate results. Due to this, fully integrated elements are usually avoided in explicit analyses [25, 27].
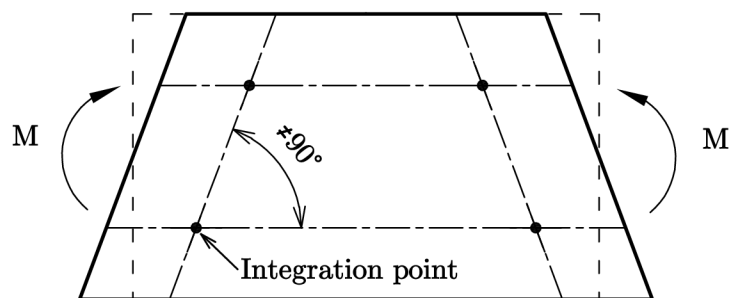
Figure 5.2: Shear locking of fully integrated element [27]

Another way to get rid of both hourglassing and shear locking would be to use quadratic (second order) elements. However, in addition to lower computing time requirement, linear elements are less sensitive to excessive deformation and tend to yield more accurate results. Thus, they are the common choice in most problems solved with explicit algorithm [27].

49

5.3 Simplified pass rolling analysis

This section describes finite element analysis of a certain pass rolling problem carried out in [22], used to assess formability of a workpiece in given geometrical and thermodynamical conditions. The problem includes hot–rolled bloom passing throught an oval and then through a circular roll pass, both of which may be seen on Fig. 5.3 and 5.4, respectively. Initial cross section and cross section assumed after passage through the first roll pass are marked by dash lines.
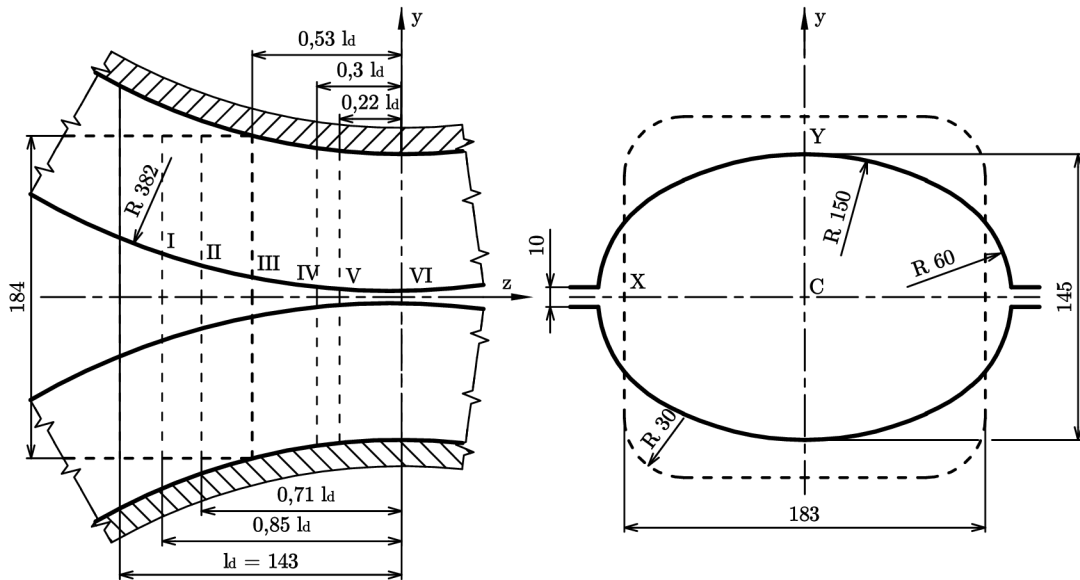
Figure 5.3: Depiction of used oval roll pass [22]
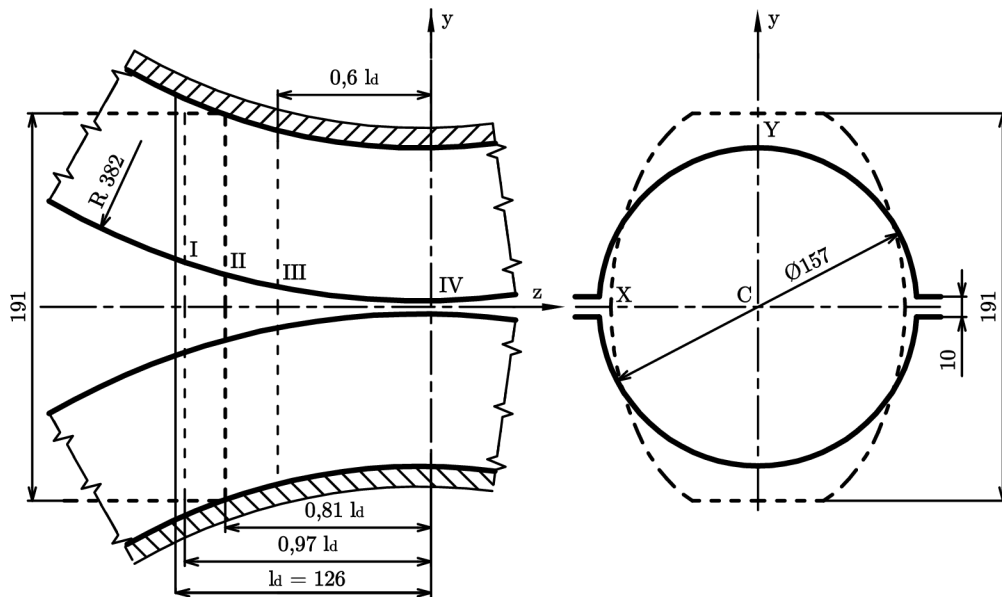
Figure 5.4: Depiction of used circular roll pass [22]

5.3.1 Analysis setup
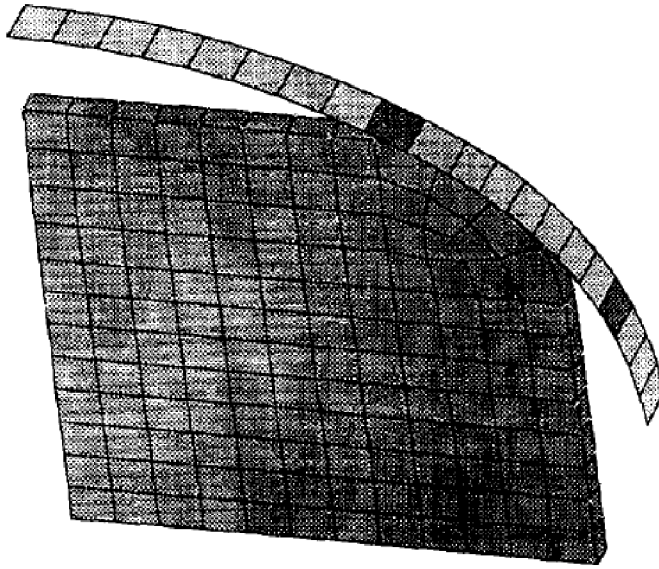
Figure 5.5: Depiction of mesh used for workpiece and oval roll pass [22]

In contrast with actual rolling operation, several simplifications were made to the finite elment model used in this analysis [22]:

- Model of the workpiece consisted only of a single layer of elements with corresponding cross sections, instead of actual length of the workpiece (see Fig. 5.5).

- Both roll passes were modelled as rigid (their deformation was omitted) shell bodies with corresponding shapes, as may be seen on Fig. 5.5.

- Due to the shape of the workpiece being symmetrical in two axes, only a quarter of it was used in the analysis.

- Friction coefficient was presumed to be constant throughout the analysis and assumed value of 0,3.

- Loading history was not taken into account, since passage through each rolling gap was simulated in a separate analysis. The model of the workpiece used in the second analysis may be seen on fig. 5.4).

- All cross sections were presumed to remain planar throughout the analysis.

In both analyses, proper symmetry conditions were applied on respective surfaces in symmetry planes and one side of the workpiece was fixed in the rolling direction. To preserve planarity of all cross sections, nodes on the other side were coupled in rolling direction, i.e. were assigned equal displacement values throughout the analysis. This state was accepted as a reasonable approximation of stationary state of rolling, i.e. excluding ends of the workpiece. Roll pass model was then assigned a displacement boundary condition, simulating passage through the rolling gap [22].

5.3.2 Results of the analysis

Results were evaluated in sections I to VI along the first roll pass (see Fig. 5.3) and I to IV for the second one (see Fig. 5.4). Stress and strain results for section III of the first roll pass were the only ones included in [22], and may be seen on Fig. 5.6 and 5.7.
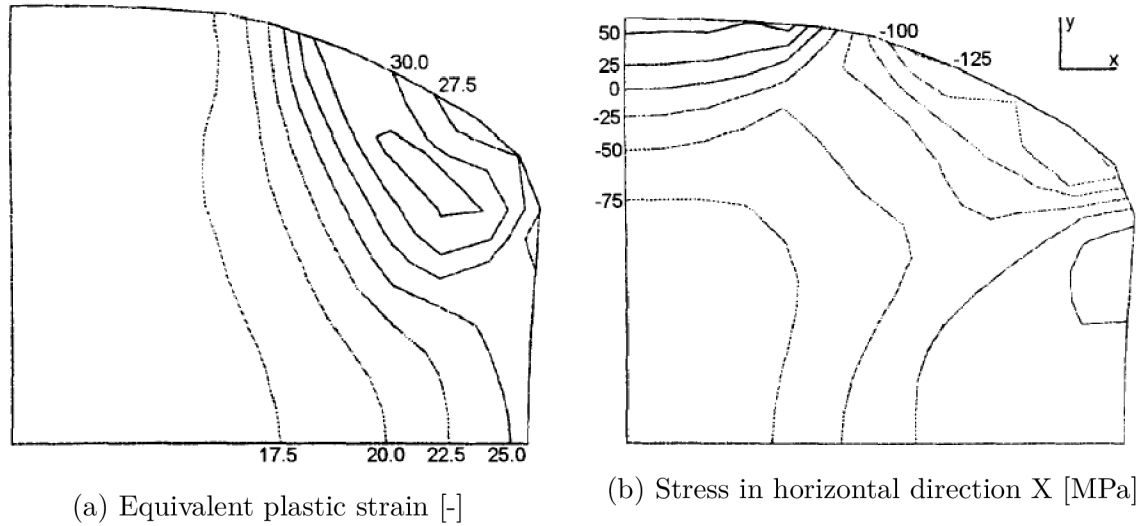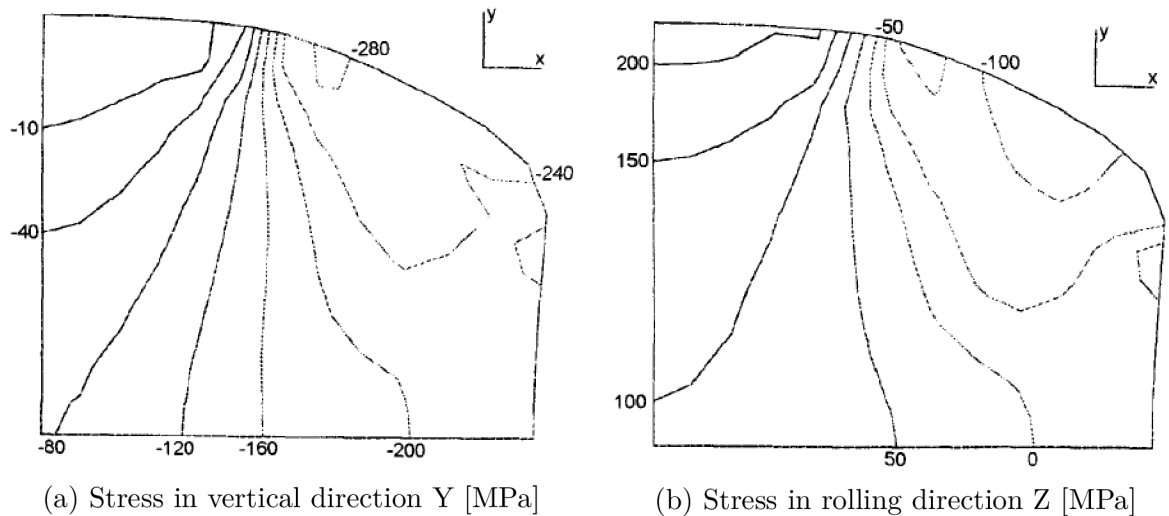

(a) Equivalent plastic strain [-]

(b) Stress in horizontal direction X [MPa]

Figure 5.6: Results at section III [22]

(a) Stress in vertical direction Y [MPa]

(b) Stress in rolling direction Z [MPa]

Figure 5.7: Results at section III [22]

In order to assess material formability, stress triaxiality factor was evaluated at central (C), rightmost (X) and uppermost point (Y) of the cross section (may be seen on Fig. 5.3 and 5.4), where risk of crack occurence was deemed highest. Values of stress triaxiality factor for both both roll passes may be seen on Fig. 5.8.

(a) First roll pass   (b) Second roll pass
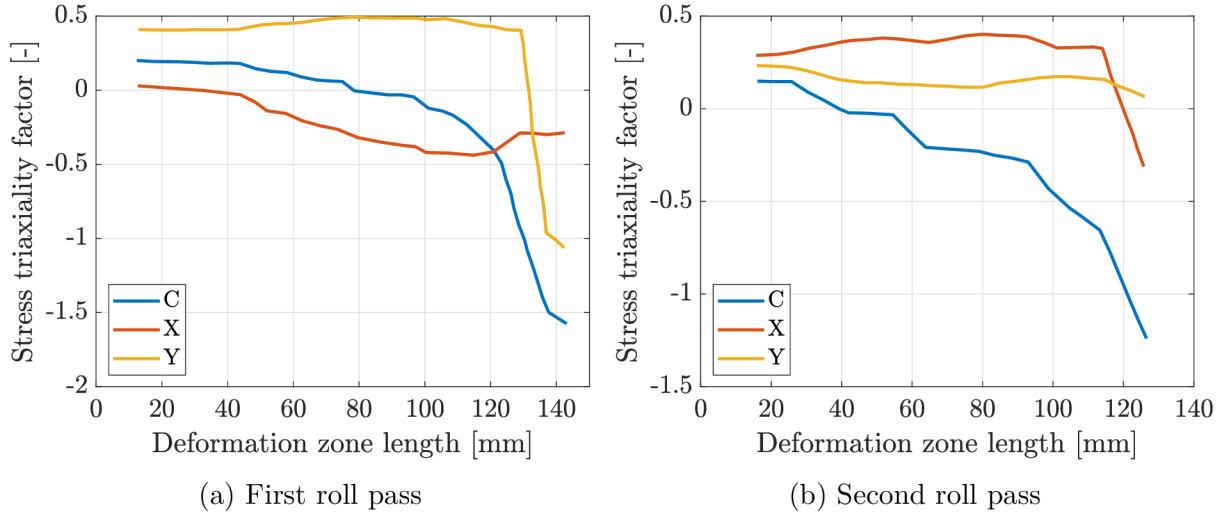
Figure 5.8: Stress triaxiality factor values for both roll passes [22]

Values of $\bar{\varepsilon}_p^f$ for given thermodynamical conditions, dependent on stress triaxiality factor, was defined by the following equation, with values of multiplier and exponent obtained through tensile and torsion tests:

$$\bar{\varepsilon}_p^f = e^{0,2728 - 2,82 \cdot \eta} \quad [22].$$
(5.13)

The only available equivalent plastic strain results were those at point Y of the first roll pass, which was labelled as the most probable location of crack initiation, as the difference between actual and limit plastic strain was the lowest there. As may be seen on Fig. 5.9, no fracture should occur, as the value was below the limit.
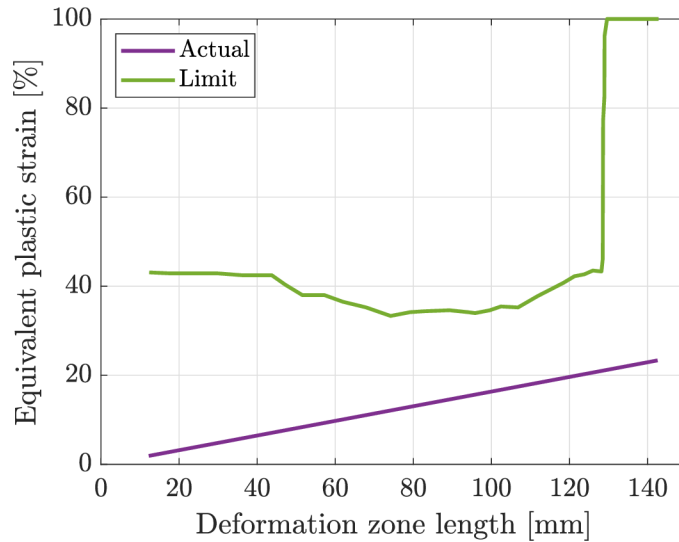
Figure 5.9: Course of actual and limit equivalent plastic strain at point Y for passage through the first roll pass [22]

6 Photoelasticimetry

Before numerical variational methods such as FEM or boundary elements method were invented, photoelasticimetry posed a viable means of experimental stress and strain analysis in a variety of industrial applications such as manufacturing, design or quality control, and even other fields like masonry or dentistry. When the analysis of materials not exhibiting photoelastic behavior was required, scaled model of geometry was made of photoelastic material, which was then loaded and constrained in a manner similar to the analysed structure [28].

Models made of photoelastic materials capable of plastic deformation were built in order to carry out photoplastic analysis, used to analyee cases such as metal rolling. According to [28], three specific types of photoplastic analysis may be distinguished, depending on the used material:

- Plastic materials, such as epoxy resin or nylon.

- Silver halides, mainly silver chloride.

- Photosensitive lacquers, which were applied on actual structures and measured using special equipment, instead of an actual model being built.

As of today, traditional photoelasticimetry is considered obsolete and is rarely used for any of the mentioned applications. It has been succeeded by other optical methods such as Digital Image Correlation (abbreviated as DIC), which is widely used due to its simple implementation and use.

6.1 Basic theory of photoelasticity

Based on photoelastic phenomenon, which was discovered and described by Scottish scientist and inventor David Brewster in early 19th century, it describes stress or strain distribution in material under mechanical deformation by changes of the material's optical properties, namely the refraction index. In other words, material with stress dependent refraction index is considered to be photoelastic [29].
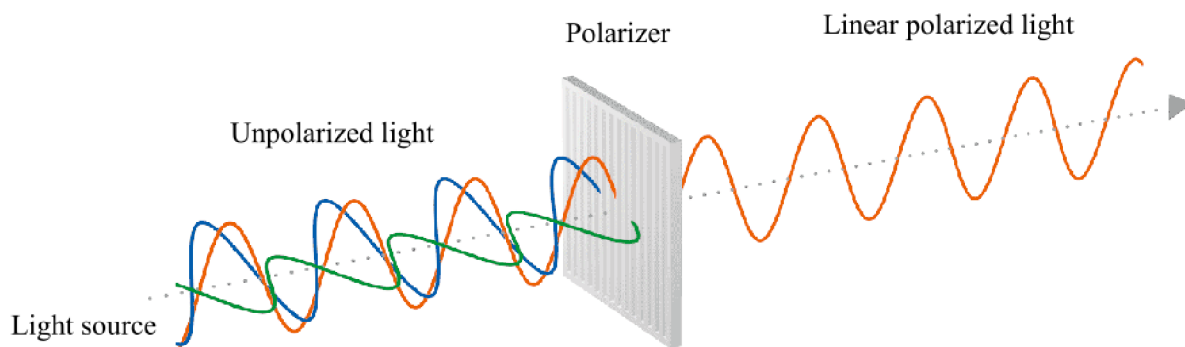

Figure 6.1: Linear polarization of emitted light [30]

Light is an electromagnetic wave that oscillates in transverse direction (orthogonal to direction of propagation). All common sources of light emit unpolarized light, meaning

that oscillation occurs in multiple directions. It may be converted into polarized light using device called a polarizer, which blocks all light except that in the respective plane of polarization (see Fig. 6.1).

Optical isotropy means that the particle density of the material is homogenous, resulting in the same optical properties in all directions. Light passing through the material in any direction experiences the same refractive index. In case of optically anisotropic material, when optical properties depend on the orientation, two refractive indices are experienced by the passing light. This phenomenon is called birefringence or double refraction. Deformation of optically isotropic material induces optical anisotropy, resulting in occurrence of birefringence [29].

6.1.1 Polariscope setup

Polariscope setup, which can be seen at fig. 6.2, consists of two polarizers and a light source. Emitted light is converted into plane polarized light when proceeding through the first polarizer, passes through the specimen and finally through the second polarizer (also called analyzer), which polarizes the light in direction orthogonal to that of the first polarizer [31].
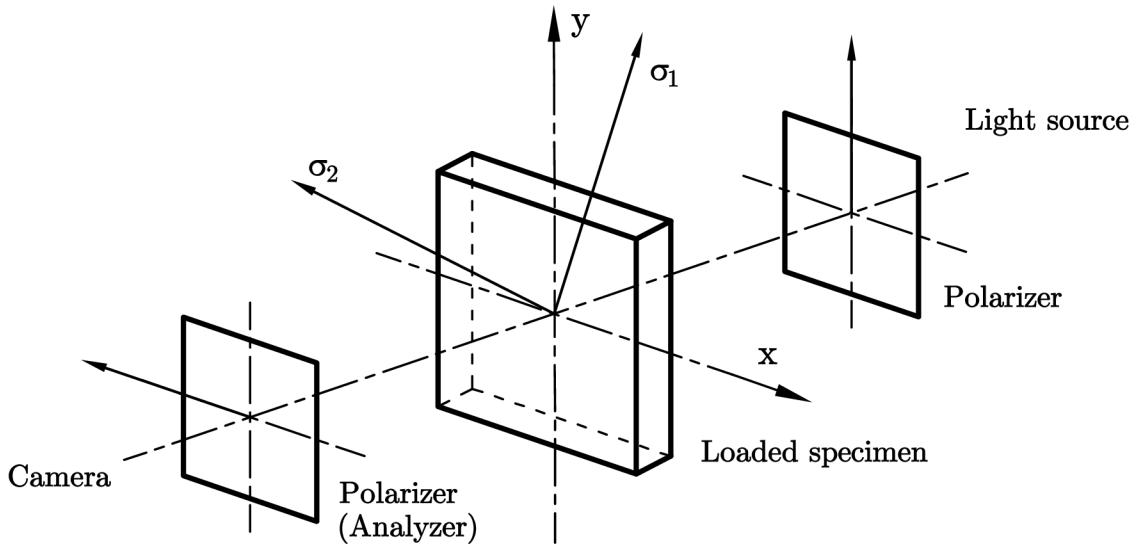

Figure 6.2: Plane polarizer setup [31]

6.1.2 Evaluation of results

When passing through material, wave components of the light are distributed along two principal stress directions, each associated with different refractive index. This difference causes relative phase retardation Δ. When a specimen made of optically isotropic material with thickness much smaller than its other dimensions is assumed, relative phase retardation is acquired from the stress–optic law:

$$\Delta = \frac{2 \cdot \pi \cdot t_{spec}}{\lambda} \cdot C_{opt} \cdot (\sigma_1 - \sigma_2) \quad [32],$$

(6.1)

where t_{spec} stands for thickness of the specimen, λ for vacuum wavelength and C_{opt} for stress–optic coefficient.

Polarization of transmitted light is altered by phase retardation, which may be used to obtain difference between first and second principal stress as well as their directions. A device called polariscope is used to combine both states of the light and reveal a fringe pattern, which is used to determine stress states present in various locations in the material. Individual stress components are then determined using any of viable stress–separation techniques [29, 28].

Fringe pattern consist of multiple types of lines. Isoclinic lines are formed by points the same direction of the principal stresses. Lines with the same values of the principal stresses and therefore same maximal shear stress are called isochromatic lines. Isostatic line are those to which principal stress directions are tangential in each point. Lines inclined by 45° to isostatic lines are called slip lines [22, 28]. Examples of all mentioned lines may be observed in Sec. 6.2.2.

6.2 Photoplastic pass rolling analysis

In addition to the finite element analysis of pass rolling described in Sec. 5.3, photoplastic analysis of analogical problem was included in the same paper [22]. Original material of the workpiece was stainless steel, which obviously does not exhibit photoelastic behavior. Instead, specimens were made of low module epoxy resin capable of plastic deformation, efficient in cases where large amounts of compressive deformation occur [28].

6.2.1 Experiment configuration

Experimental model was simplified similarly to the computational model model described in Sec. 5.3:

- Dimensions of all models used in the experiment were scaled 1:5 to the original.

- Specimens with thickness of 3 mm and corresponding cross sections were used.

- Both roll passes were replaced by shape templates with the same contour. Being much stiffer than the workpiece, their deformation was neglected.

- Separate specimens were used for each passage through the rolling gap.

The specimens were placed between the templates. Whole assembly was placed between two transparent plates to ensure proper elongation of the specimen in the rolling direction, while preserving planarity of the cross sections. Polarizers were placed on each side of the assembly and the templates were gradually moved closer to each other, applying load to the specimen [22].

6.2.2 Results

Results for both passes were evaluated in the same stages of the loading process as described in Sec. 5.3. Deformed shape of the specimen in sections III and VI may be seen on Fig. 6.3.
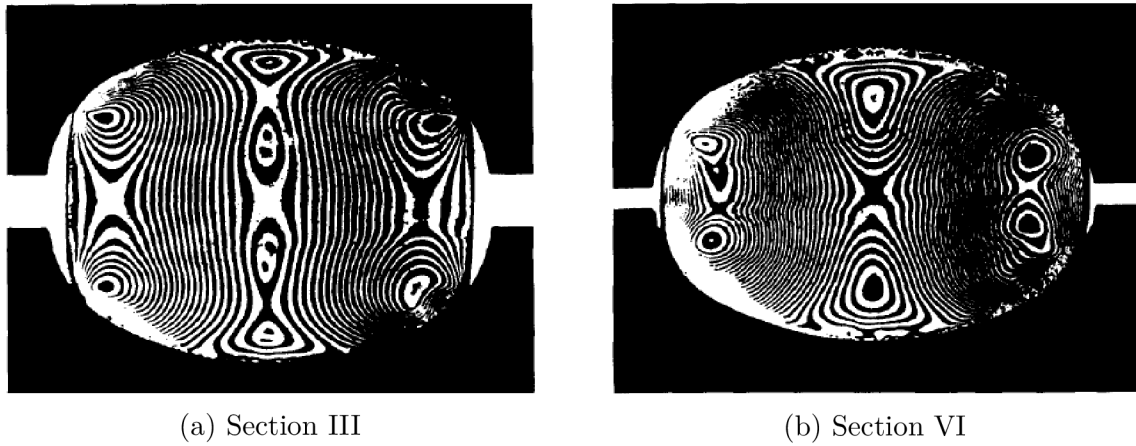

| (a) Section III | (b) Section VI |

Figure 6.3: Deformed specimen during photoplastic analysis [22]

However, the only results included in [22] were those for section III of the first roll pass. These include isoclinic and isochromatic lines, both of which describe strain distribution throughout the specimen and may be seen on Fig. 6.4a. A system of isostatic lines and slip lines (see Fig. 6.4b) was constructed using obtained isochromatic lines.

(a) Isoclinic (upper) and isoclinic lines (lower)   (b) Isostatic (upper) and slip lines (lower)
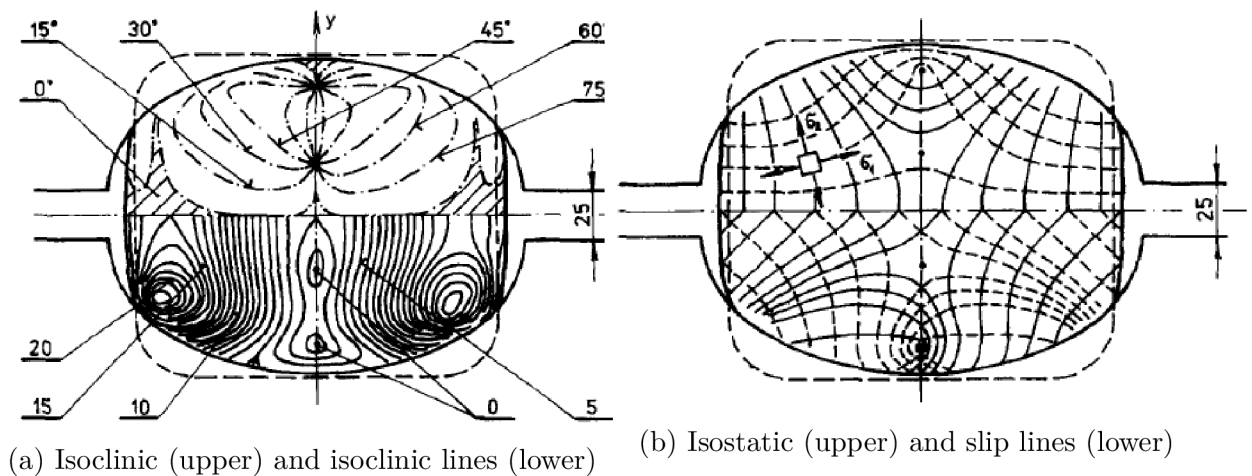
Figure 6.4: Fringe patterns obtained from photoplastic analysis at section III [22]

Values of principal stresses and strain differences were separated using techniques properly described in [33]. Subsequently, equivalent stress and strain distributions were obtained (see Fig. 6.5), as well as courses of directional stresses along both symmetry lines, which may be seen on Fig. 6.6.
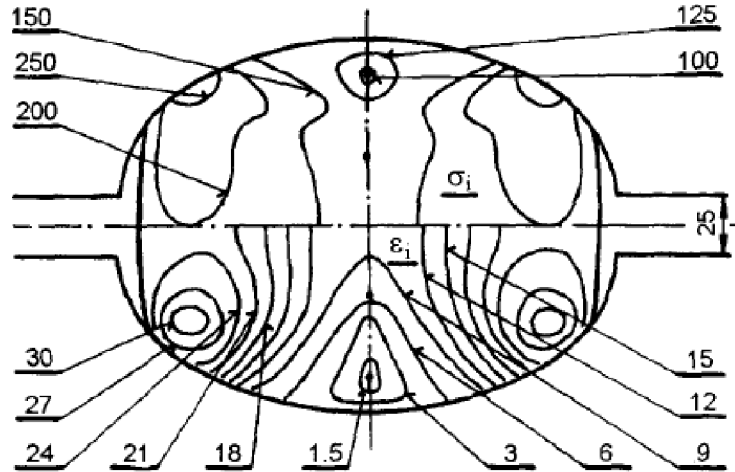
57

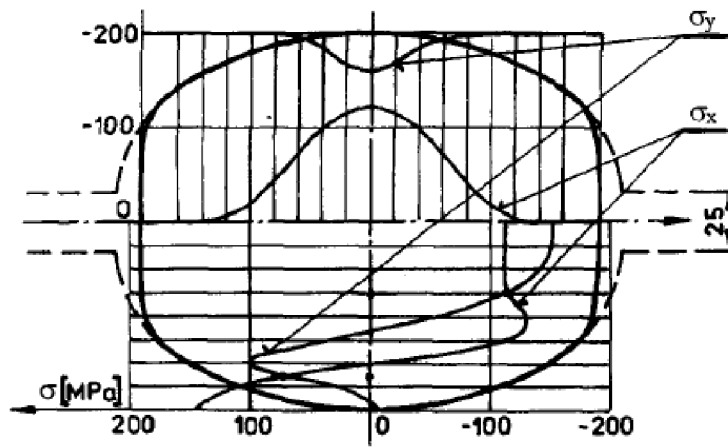Figure 6.5: Equivalent stress [MPa] and strain [%] distribution at section III [22]

Figure 6.6: Vertical and horizontal stress [MPa] along symmetry lines at section III [22]

7 Finite element analysis of pass rolling

This chapter describes creation of finite element models used for structural analysis of pass rolling. A total of three models were created, those being:

- Case A - Full 3D simulation.

- Case B - Separate planar simulation.

- Case C - Sequential planar simulation.

7.1 Used software and hardware

All analyses were carried out in Abaqus/CAE 2019 computing environment.

Hardware specifications of the workstation which was used to perform the analyses is listed below:

- Operating system: Microsoft Windows 10 education 64–bit
- Physical memory: 16 GB RAM
- CPU: AMD Ryzen 5 1500X Quad–core Processor
- CPU frequency: 3,50 GHz
- Number of CPU cores: 4 (8 logical processors)
- Graphic card: NVIDIA GeForce GTX 1050 Ti
- Graphic card memory: 4 GB
- Disc drive: Kingston S A400 S37480G SSD (Solid State Drive)
- Data transfer speed: up to 500 MB/s Read and 450 MB/s Write

Due to licence limitations, only 2 cores (4 logical processors) were employed to carry out the analyses.

7.2 Case A - full simulation

This model simulates passage of workpiece through two rolling gaps and is the cornerstone of the whole thesis.

7.2.1 Geometry

Due to two available symmetry planes, only the upper right quarter of real geometry was created. Individual bodies present in the analysis include:

- Workpiece - a rectangular bar with rounded corner, modelled as a solid body. All dimensions may be found on Fig. 7.1.
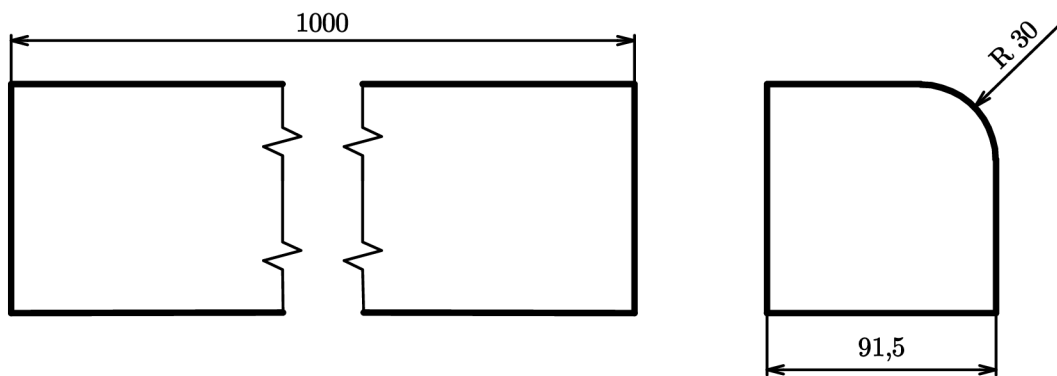

Figure 7.1: Geometry of the workpiece model

- Pusher plate - planar, square shaped rigid surface, its edge 130 mm long.

- Oval roll pass - roll pass groove which comes into contact with the workpiece is modelled as a rigid surface (see Fig. 7.2a). Other geometric elements are omitted.

- Circular roll pass - similar to oval roll pass, its dimensions may be seen on Fig. 7.2b
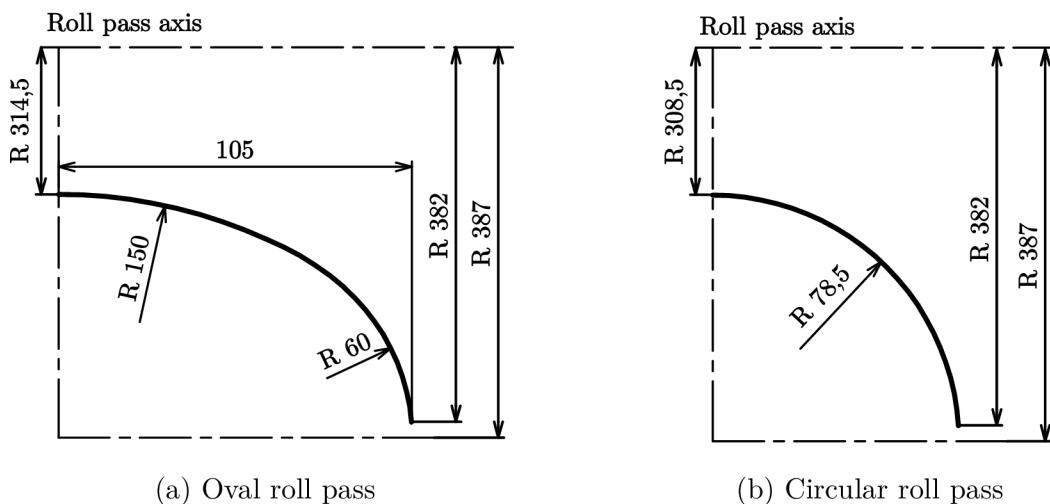

(a) Oval roll pass

(b) Circular roll pass

Figure 7.2: Geometry of both roll pass models

7.2.2 Finite element mesh

To enable use of mapped mesh, model of the workpiece geometry was partitioned by two planes, creating four cells and effectively separating the filleted corner.
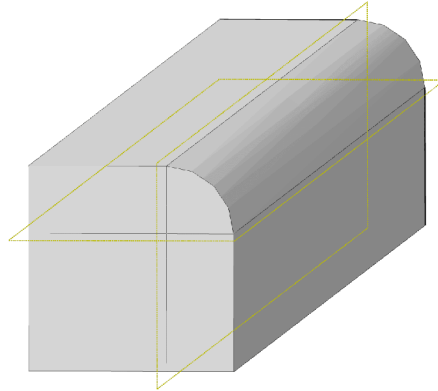

Figure 7.3: Partitioned geometry of the workpiece

Element type C3D8R, a solid linear 8–node brick element with reduced integration and hourglass control, was assigned to the model of the workpiece. Then, to recreate the model used in [22] as closely as possible, a mesh similar to the original one (see Fig. 5.5 in Sec. 5.3.1) was used for the workpiece and may be seen on Fig. 7.6a. Elements of maximum size 7,5 mm were used in all cells except the upper right, which contained the rounded corner. A slightly coarser mesh was used there, created by lowering the number of elements along the radius from six to four.
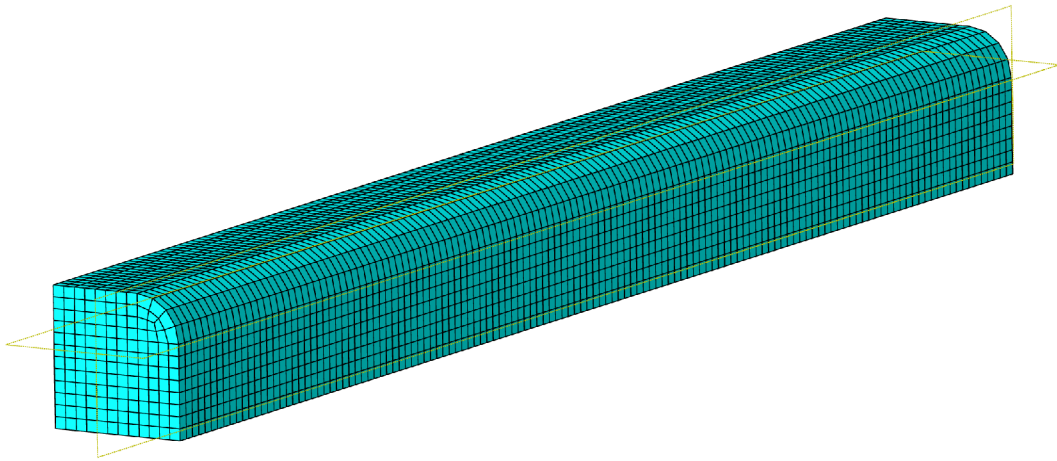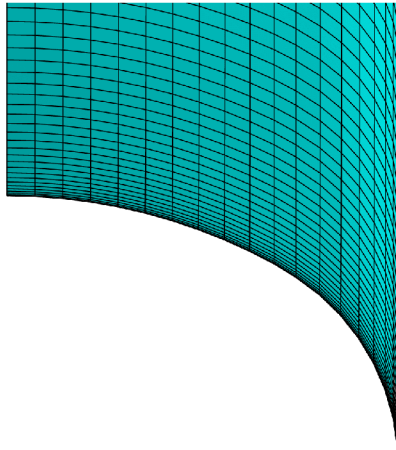

Figure 7.4: Meshed geometry of the workpiece

Surfaces of all rigid bodies were meshed using free mesh option and therefore did not require to be partitioned. These surfaces were assigned element type R3D4, a bilinear rigid 4–node quadrilateral shell element. Maximum element size was 7,5 mm, same as the workpiece. Both meshed roll passes are depicted on Fig. 7.5.

(a) Oval roll pass
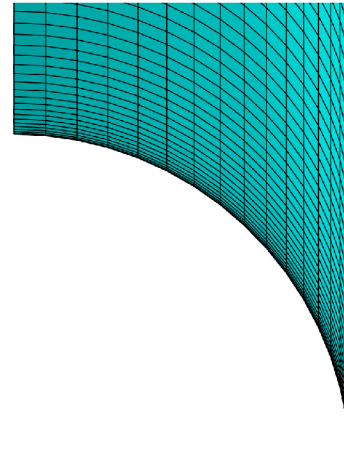
(b) Circular roll pass

Figure 7.5: View of meshed roll passes in rolling direction

In order to determine the effect of the used mesh on the acquired results, mesh convergence study was suggested. A total of four mesh variants were used, those being the original , 7,5 mm, 5 mm and 3 mm, all of which may be seen on Fig. 7.6 and 7.7. The same element sizes were applied on rigid surfaces for respective mesh variants.
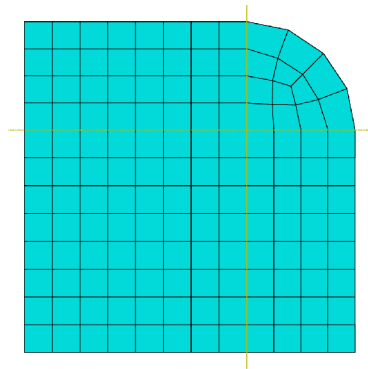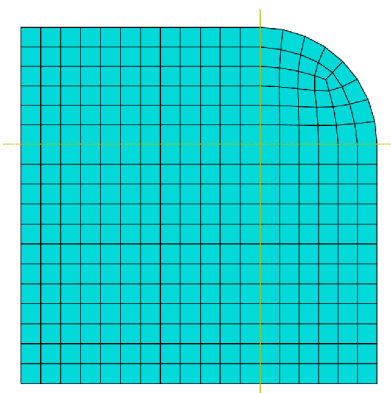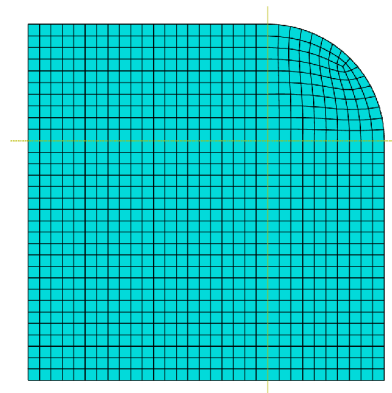

(a) Original mesh used in [22]
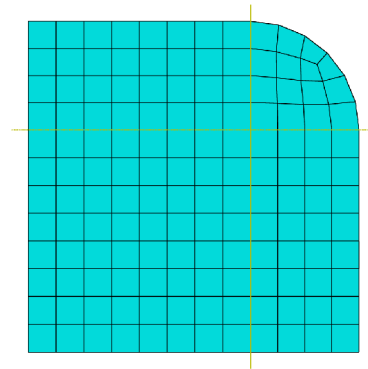
(b) Element size 7,5 mm

Figure 7.6: Cross section of the workpiece meshed using various element sizes

(a) Element size 5 mm

(b) Element size 3 mm

Figure 7.7: Cross section of the workpiece meshed using various element sizes

Summary of node and element counts of each component for every mesh may be seen in tab. 7.1.

Table 7.1: Properties of used mesh variants

| Component | Mesh variant | | | | | | | |
| | Original | | 7,5 mm | | 5 mm | | 3 mm | |
	Nodes	Elem.	Nodes	Elem.	Nodes	Elem.	Nodes	Elem.
Cross section	163	140	167	143	355	320	2 036	957
Workpiece	21 842	18 620	22 379	19 019	71 355	64 000	340 012	318 681
Oval roll pass	5 377	5 094	5 377	5 094	11 956	11 529	32 660	31 950
Circular roll pass	4 913	4 624	4 913	4 624	10 850	10 416	28 920	28 197
Pusher plate	324	289	324	289	729	676	1 936	1 849
Whole assembly	32 459	28 633	32 992	29 026	94 890	86 621	403 528	380 677

7.2.3 Assembly & Boundary conditions

Topology of the whole assembly at the start of the analysis may be seen on Fig. 7.8.
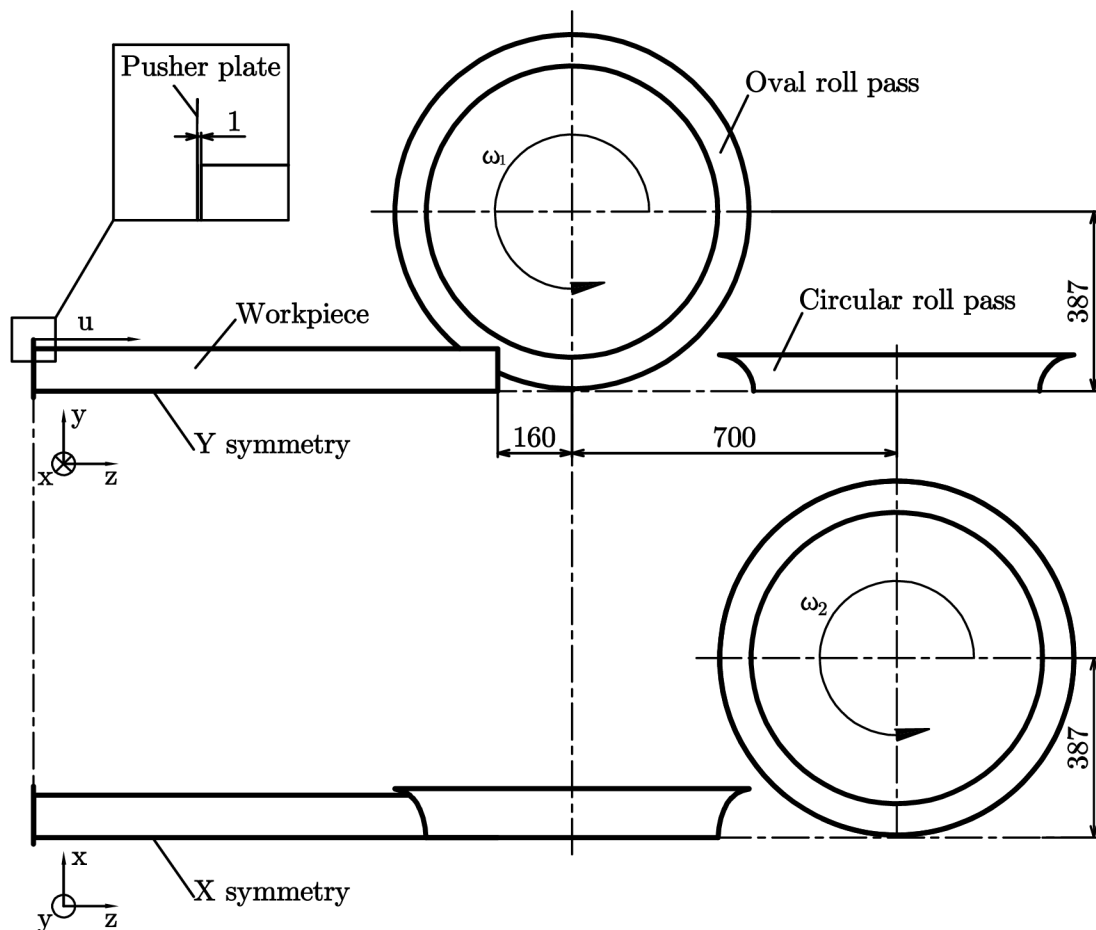

Figure 7.8: Initial layout of components of the full model

When rigid bodies are used in an analysis, they are assigned a single reference point where loads, predefined fields or boundary conditions are applied. In case of roll passes, it was defined at their center, in the respective symmetry plane. For the pusher, reference point was defined in one of its corners.

Symmetry in YZ plane ($U_X = 0$, $R_Y = 0$, $R_Z = 0$) was applied to the bottom side of the workpiece and reference point of the first roll pass. Similarly, symmetry in XZ plane ($U_Y = 0$, $R_X = 0$, $R_Z = 0$) was defined for the second roll pass, which is positioned orthogonal to the first one.

Another boundary condition, applied reference points of both rolls, was used in order to constrain remaining degrees of freedom ($U_Y = 0$, $U_Z = 0$ for the first and $U_Y = 0$, $U_Z = 0$ for the second roll pass), except the rotational direction (R_X for the first and R_Y for the second roll pass).

Since no rate dependency was defined for the material and no strain rate value was specified in [22], $n_1 = 15$ revolutions per minute was chosen for the first roll pass. The value was then converted into angular velocity:

$$\omega_1 = \frac{2 \cdot \pi \cdot n_1}{60} = \frac{2 \cdot \pi \cdot 15}{60} = 1{,}57 \, \text{rad/s}. \tag{7.1}$$

Angular velocity of the second roll pass was determined using law of continuity, which must be obeyed in order to secure optimal material flow in tandem rolling. Since radii (distance from roll pass axis to the center of the workpiece) of both roll passes were equal, following equation was used:

$$\omega_2 = \frac{S_1^{gap} \cdot \omega_1}{S_2^{gap}} = \frac{5542{,}3 \cdot 1{,}57}{4839{,}8} \doteq 1{,}8 \, \text{rad/s}. \tag{7.2}$$

Displacement boundary condition of 120 mm in Z direction was applied to pusher plate, centered and positioned 1 mm behind the workpiece. A linear amplitude was assigned to the movement. At this stage, frictional forces on the interface were able to pull the workpiece through the rolling gap, successfully commencing the rolling process.

The analysis was divided into two separate steps. Displacement of the pusher took place in the first step, which was 0,27 s long. Since lenght of the second load step was 4,3 s, the time at the end of the analysis was 4,57 s.

7.2.4 Interaction and contact conditions

As described in Sec. 3.2.1, friction coefficient assumes various values depending on the current state of rolling operation. In this analysis, however, it was assumed to be constant. Using penalty method, it was assigned value of 0,3, corresponding with [22].

Contact conditions were defined by General contact option, which may be used exclusively with the explicit algorithm. This option might have been sufficient, but even so, meshes were used to define surfaces to further ensure that no penetration would occur on the interface of the components:

- Surface and volume of the workpiece

- Surface of pusher plate

- Surface of oval roll

- Surface of circular roll

For the workpiece, whole surface of each element was taken into account. For rigid bodies, sides where the contact would occur were chosen. Using surfaces defined above, following contact pairs were defined:

- Oval roll - workpiece.

- Circular roll - workpiece.

- Pusher plate - workpiece.

- Workpiece - itself. This pair was defined to ensure that surface nodes of the workpiece would not penetrate the nodes beneath during compressive deformation, .

7.2.5 Model of material

Since all bodies except the workpiece were defined as rigid, they were not assigned any material parameters.

As was stated in [22], the workpiece was made of stainless steel ČSN 41 7246, chemical composition of which may be seen in tab. 7.2. Since its density at elevated temperatures was not provided in the material standard [19], effect of temperature was omitted and its value at room temperature – 7900 kg/m^3 – was used.

Table 7.2: Chemical composition of stainless steel ČSN 41 7246 [19]

Element	C	Mn	Si	Cr	Ni	Ti	P	S
	max.	max.	max.			min.	max.	max.
Value [%]	0,12	2,00	1,00	$17,0 - 20,0$	$8 - 11,0$	$5 \cdot (\% \text{ C} - 0,03)$	0,045	0,030

Material behavior was defined as elastic–plastic with large strains and isotropic hardening. While strain rate or temperature dependency was defined, their effect is included in the flow curve, which was provided by the following equation:

$$\bar{\sigma} = 264,7 \cdot \bar{\varepsilon}^{0,1855} \quad [22], \tag{7.3}$$

which corresponds with reference thermodynamical conditions, those being temperature $T = 1000°$ C and strain rate $\dot{\varepsilon} = 0,2 \ s^{-1}$.

As mentioned earlier, elastic and plastic strain components are assigned separate models of material, which is properly described in the following lines. Overview of material parameters used in the analyses may be seen in tab. 7.3.

Table 7.3: Summary of used material parameters

E [GPa]	μ [–]	ρ [kg/m^3]	$R_{p0,2} [MPa]$
75	0,3	7900	90

Elastic component

For the elastic component of strain, isotropic linear elastic model was used. Since value of Poisson's ratio was not specified in the material standard [19], commonly used value of 0,3 was utilized instead. Also, value of Young's modulus at elevated temperatures was specified only up to 600 °C, as seen on Fig. 4.3. Due to this, its value at 1000 °C was determined to be 75 GPa, which was obtained using the slope of the elastic part of the flow curve (see Fig. 7.9).
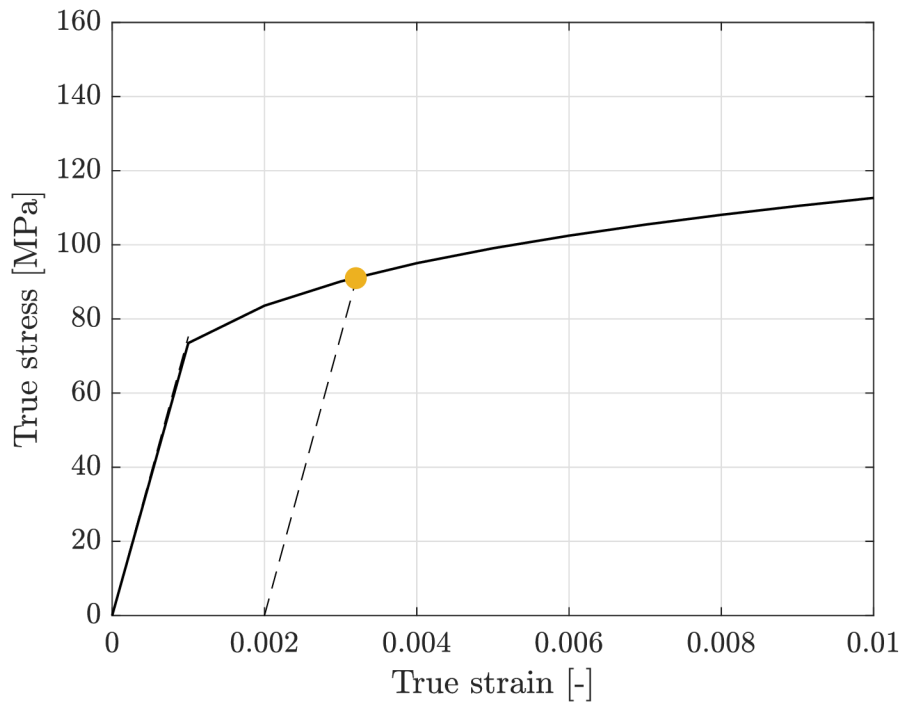

Figure 7.9: Determination of proof strength and Young's modulus from the flow curve [22]

Plastic component

Multilinear Mises plasticity model with isotropic hardening was defined to simulate plastic behavior of the material. Since yield stress at elevated temperatures was not specified in the material norm [19], proof strength at 0,2 % of plastic strain $R_{p0,2} = 91$ MPa, which results in 0,2% of plastic strain, was determined from the flow curve (see Fig. 7.9).

In order to define Mises plasticity, plastic strain values were required. These were acquired by substracting elastic ε_e from total strain values ε_t:

$$\varepsilon_p = \varepsilon_t - \varepsilon_e. \tag{7.4}$$

Substituting ε_e with Hooke's law in Eq. 7.4, following equation was obtained:

$$\varepsilon_p = \varepsilon_t - \frac{\sigma}{E}. \tag{7.5}$$

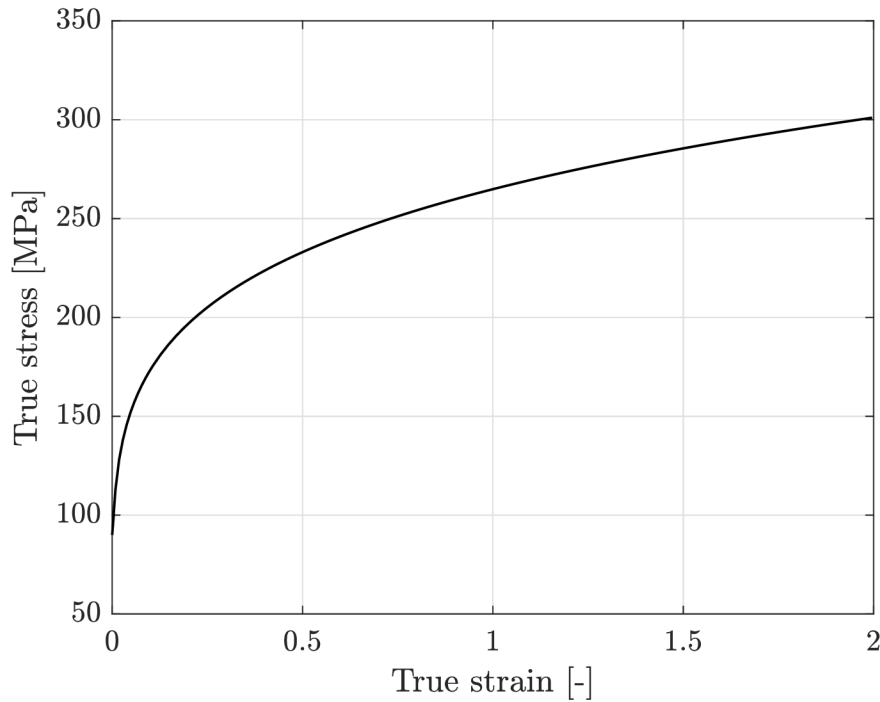Flow curve defined with separated plastic strain values may be seen on Fig. 7.10.

Figure 7.10: Separated plastic strain values

7.3 Case B - Separate planar simulation

Recreation of the original simplified analysis described in [22] is the purpose of this variant of computational model. It consists of two analyses, each simulating passage through one rolling gap. Used contact conditions and model of material were the same as in previous analysis and therefore are not mentioned below.

7.3.1 Assembly & Boundary conditions

Similar to the analysis described in [22], slices with corresponding cross sections were used instead of whole workpiece. While the first slice bore the same shape as initial cross section of the workpiece in previously described analyses, the second slice was shaped as it was supposed to be after leaving the first rolling gap (see Fig. 5.4 in Sec. 5.3), according to [22]. Since thickness of used model of the workpiece was not specified in [22], a dimension equal to the size of used elements was used, which was 7,5 mm. Both roll passes were modelled as rigid surfaces with corresponding shapes and width of 20 mm. Their reference points were defined on their ends. Geometry layout for both analyses may be seen on Fig. 7.11 and 7.12.
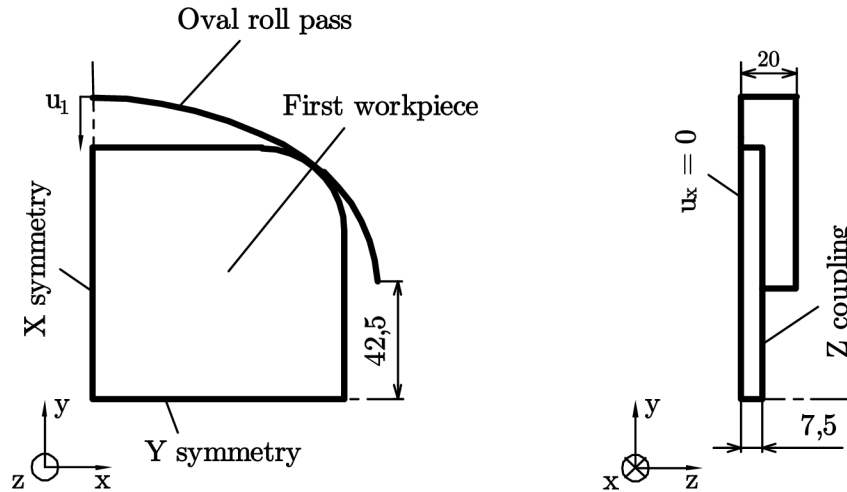
67

Figure 7.11: Initial layout of comopnents of the separate model for passage through oval roll pass
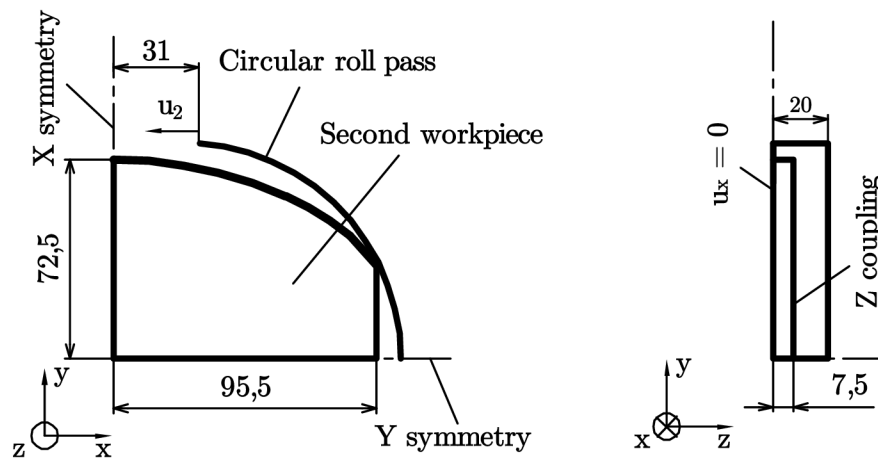

Figure 7.12: Initial layout of comopnents of the separate model for passage throught circular roll pass

Equal sets of boundary conditions, based on information found in [22], were used for both analyses. Symmetry boundary conditions were applied on appropriate surfaces of the workpieces. While one side of each workpiece was constrained in Z direction, kinematic coupling in Z direction was defined for the other. Displacement boundary conditions in respective directions were applied on models of oval $u_1 = 37{,}5$ mm and circular roll pass $u_2 = 26$ mm. Analyses consisted of one step with length of 0,2 s and 0,15 s, respectively.

As may be seen on Fig. 7.13a, deformation of material in the upper left corner of the second workpiece caused it to flow out of the rolling gap. To prevent this behavior and secure proper deformed shape of the second workpiece, an arc with corresponding radius and horizontal length of 5 mm was created, as well as extension of 20 mm in X direction (see Fig. 7.13b).
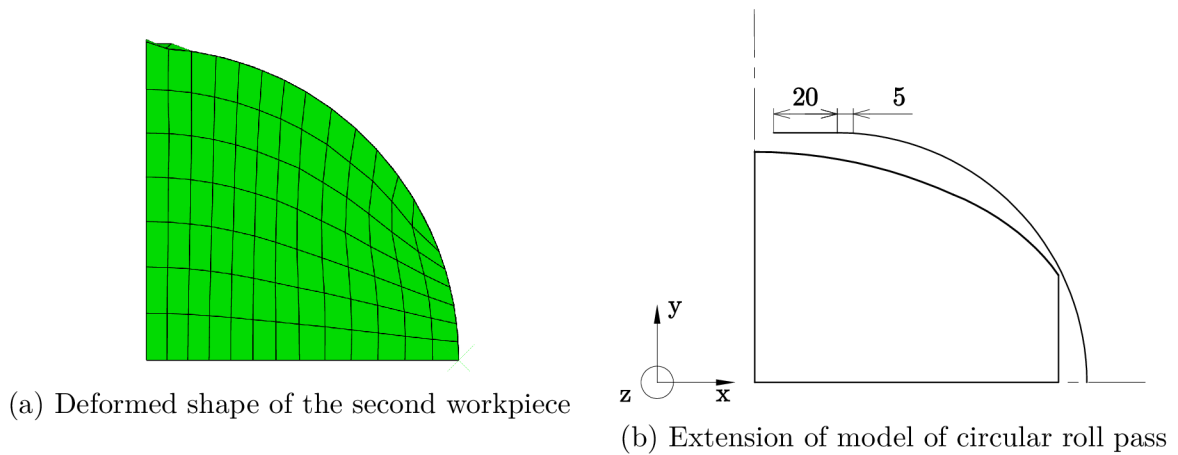
(a) Deformed shape of the second workpiece

(b) Extension of model of circular roll pass

Figure 7.13: Solution of inappropriate deformation of the second workpiece

7.3.2 Finite element mesh

To enable use of mapped mesh, first model of the workpiece was partitioned the same as in the previous case, while the partition of the second may be seen on Fig. 7.14. Elements types used for both deformable and rigid bodies were the same as in the previous case.
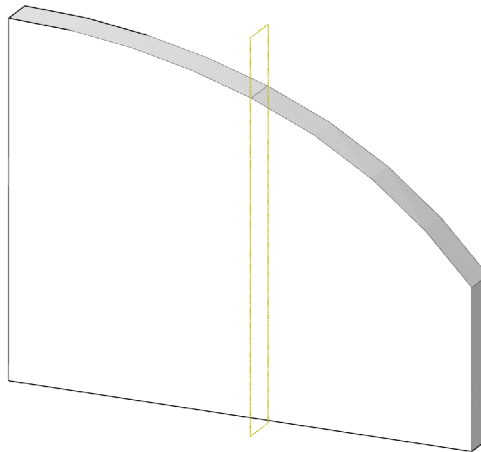

Figure 7.14: Partitioned geometry of the second workpiece

Except the first workpiece, for which the original mesh from [22] was used, meshes of all bodies consisted of elements sized 7,5 mm. However, the software was not able to mesh the workpiece with a single layer of elements. Two layers were used instead. Meshes used for both analyses may be seen on Fig. 7.15.

(a) Passage through oval roll pass   (b) Passage through circular roll pass
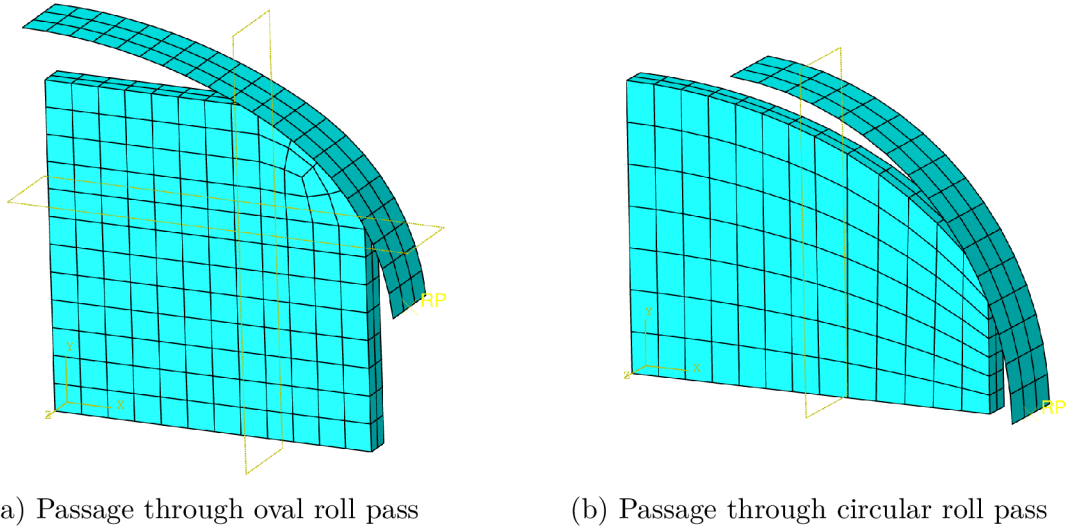
Figure 7.15: Meshed components of the separate model

Total number of nodes and elements for both analyses may be seen in tab 7.4.

Table 7.4: Total number of nodes and elements for both analyses

	Analysis			
Component	First		Second	
	Nodes	Elements	Nodes	Elements
First workpiece	489	280	-	-
Oval roll pass	84	60	-	-
Second workpiece	-	-	336	182
Circular roll pass	-	-	84	60
Total	573	340	420	242

7.4 Case C - Sequential planar simulation

The only difference from the previous variant is that passages through both rolling gaps are simulated in the same analysis, thus respecting the loading history. Only the first workpiece is deformed by both oval and circular roll pass (see Fig. 7.16). Model of circular roll pass was extended in the same way as in the previous case (see Fig. 7.13b).
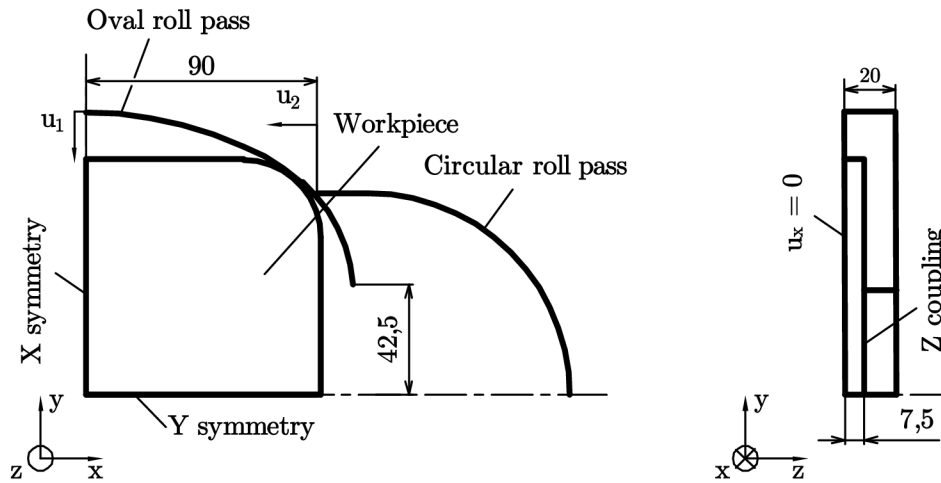
Figure 7.16: Initial layout of components of the sequential model

Displacement boundary condition applied on the first roll pass is the same as in previous analysis $u_1 = 37,5$ mm and occurs during first step, which lasts 0,2 s. During second step, workpiece is unloaded as roll pass returns to its initial position over the next 0,2 s. At the start of the same step, displacement $u_2 = 100$ mm is applied on the second roll pass and occurs over the next 0,6 s. Total time of the analysis is 0,8 s.

Mesh used in the analysis may be seen on Fig. 7.17. A total of 657 nodes and 400 elements were used.
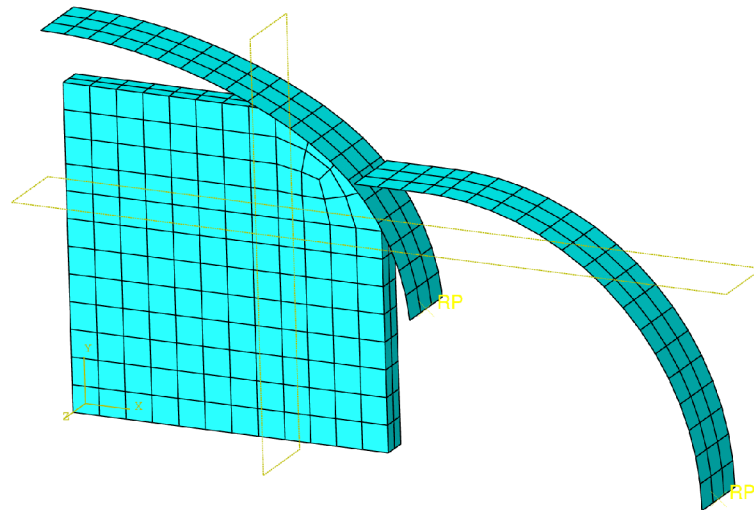
Figure 7.17: Meshed components of the sequential model

8 Result summary

Various results obtained from finite element analyses with models introduced in previous chapter are displayed and discussed in the sections below. Illustratory depictions of the full and simplified models may be seen on Fig. 8.1 and 8.2, respectively.
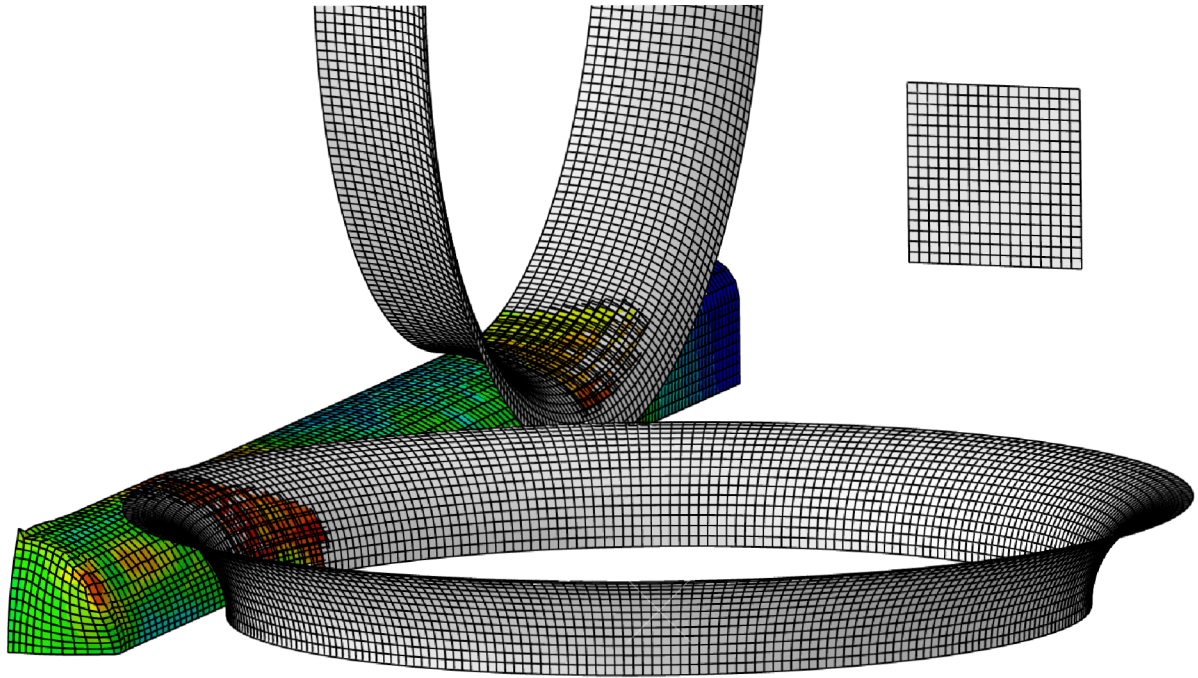
Figure 8.1: Material flow in analysis with the full model

(a) Separate model

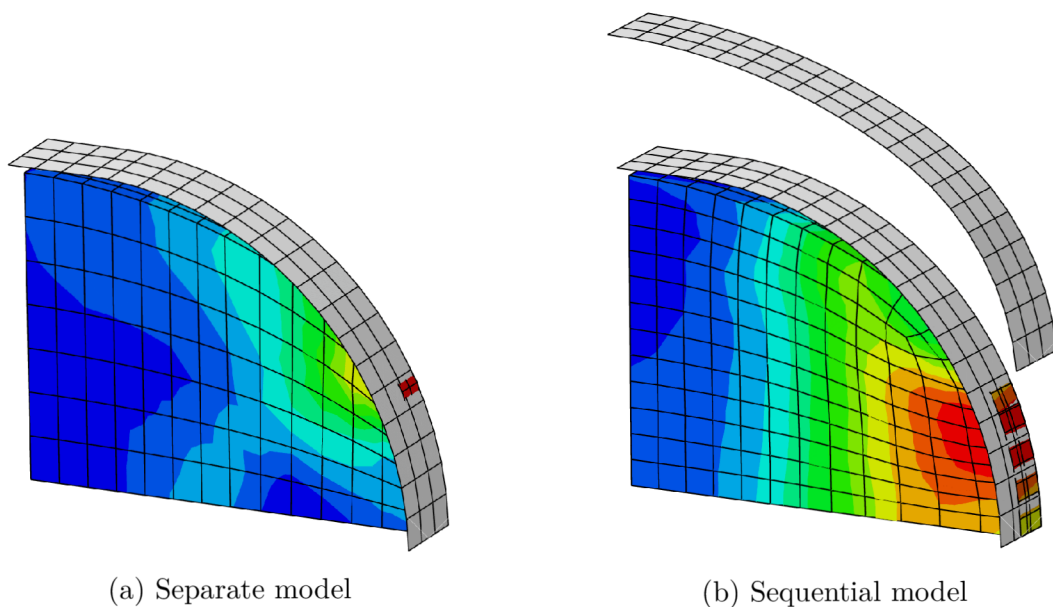(b) Sequential model

Figure 8.2: Filling of the second rolling gap in analyses with the simplified models

Summary of computing times required for each analysis may be found in Tab. 8.1. Analysis with element size 3 mm and 5 mm were not carried out completely due to excessive computing time requirements. Whole analyses would probably require more

than 70 and 30 hours, respectively. The time required for analysis with the separate planar model is a sum of both analyses, which were carried out separately.

Table 8.1: Summary of computing times elapsed during individual analyses

		Full			Simplified	
	Original	7,5 mm	5 mm	3 mm	Sequential	Separate
Time [hh:mm:ss]	1:24:46	1:54:35	9:46:23	16:31:40	00:11:35	00:05:19

It should be noted that all evaluated $\bar{\varepsilon}$ values are $\bar{\varepsilon}_p^{cum}$ values and are denoted either as equivalent plastic strain or PEEQ, which is an abbreviation used in Abaqus.

8.1 Mesh convergence study

Four variants of finite element mesh, seen on Fig. 7.6 and 7.7 in Sec. 7.2.2 were used to carry out a mesh convergence study. Only the full simulation was taken into account. Stress triaxiality factor at point Y for passage through the first roll pass was evaluated for each mesh variant. As may be seen on Fig. 8.3, element size did not affect the acquired results in any notable way, making the original mesh variant a choice for result evaluation at specific points on the cross section. Results acquired with the original mesh used in [22] are marked as '10 mm' in this figure.
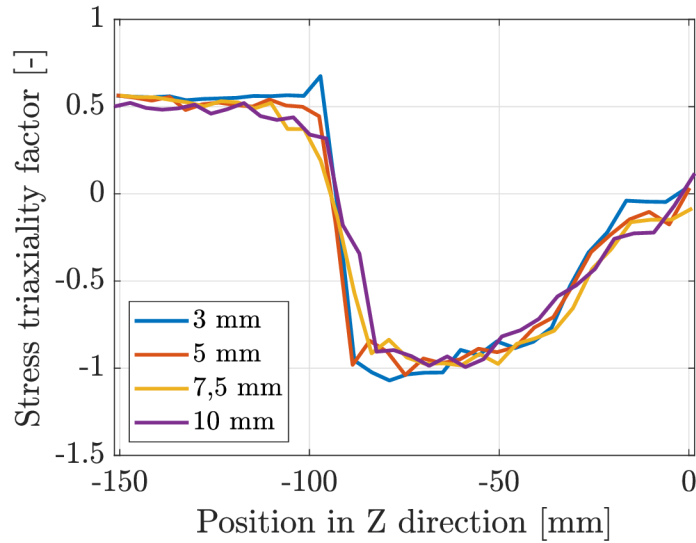

Figure 8.3: Stress triaxiality values at point Y for passage through the first roll pass obtained from different mesh variants

Furthermore, as seen on Fig. 8.4, maximum values of Mises equivalent stress and plastic strain, respectively, were evaluated at section III, position of which is specified later in Sec. 8.3. This comparison has shown that there is a difference in maximum values obtained with the original and 7,5 mm mesh. In Sec. 8.6, results from both of these variants are evaluated in order to determine the possible effect of element size on material formability. Beyond these two variants, the differences were negligible and none of the other mesh variants were further used.
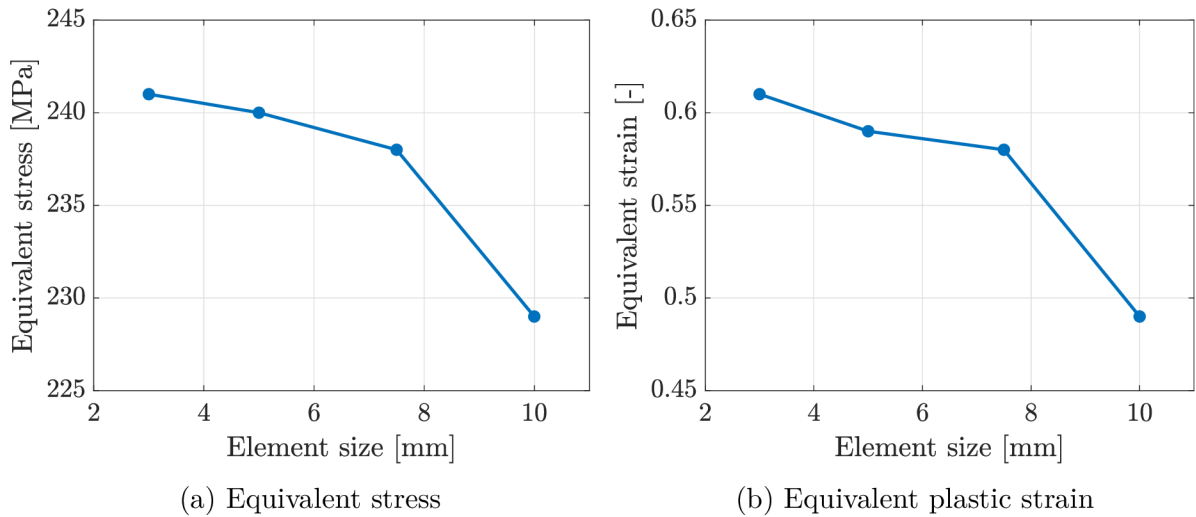
(a) Equivalent stress

(b) Equivalent plastic strain

Figure 8.4: Maximum equivalent stress and plastic strain values obtained from different mesh variants

8.2 Evaluation of dynamic effects

As mentioned in Sec. 7.2.3, values of angular velocities of the roll passes were chosen arbitrarily since no valued were specified in [22]. To ensure that no notable dynamic effects, such as inertial forces, would be present in the analyses and the results would not be affected by hourglassing, values of total strain energy, kinetic energy and artificial strain energy were compared for both full (see Fig. 8.5a) and simplified (see Fig. 8.5b) model. Since these comparisons have proven that kinetic energy nor artificial strain energy reached 10 % of total strain energy in either of the analyses, their results were considered reliable.
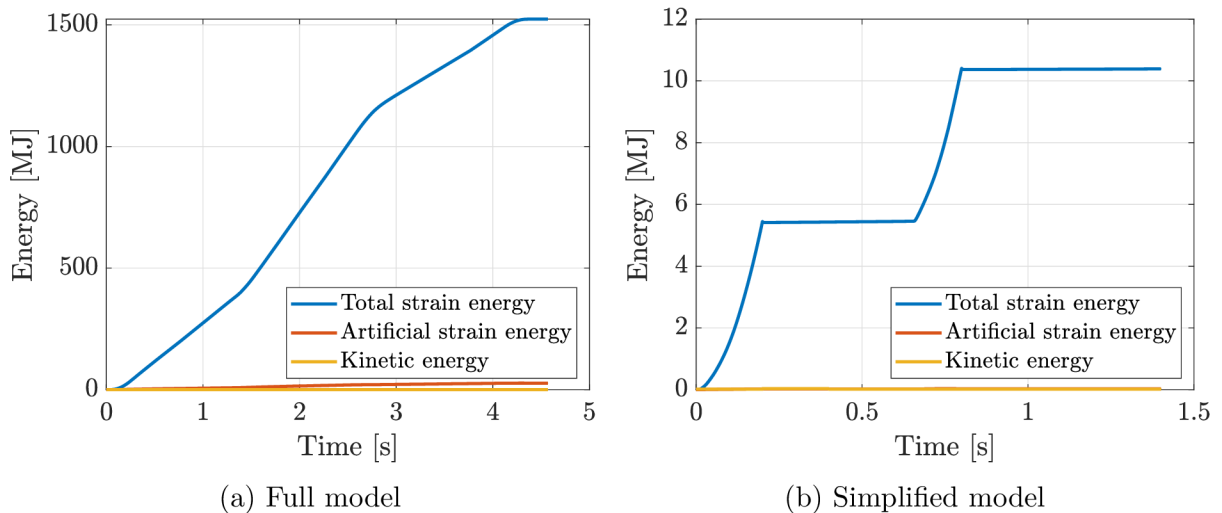

(a) Full model

(b) Simplified model

Figure 8.5: Courses of energy values throughout analyses

8.3 Stress and plastic strain distribution

Distribution of stress and plastic strain throughout the cross section of the workpiece for passage through the first roll pass was evaluated from the computational models. In [22], it was stated that these results were evaluated at section III, which lay 75,8 mm from the narrowest point of the rolling gap. This claim was either a mistake, or the progress of the deformation vastly differed from other computational models. Deformed shape of the workpiece in 3D model at this location may be seen on Fig. 8.6a. New plane of evaluation was chosen at -110 mm (see Fig. 8.6b), where the deformed shape and stress distribution corresponds more accurately to the original analysis.

(a) Original position

(b) Newly chosen position
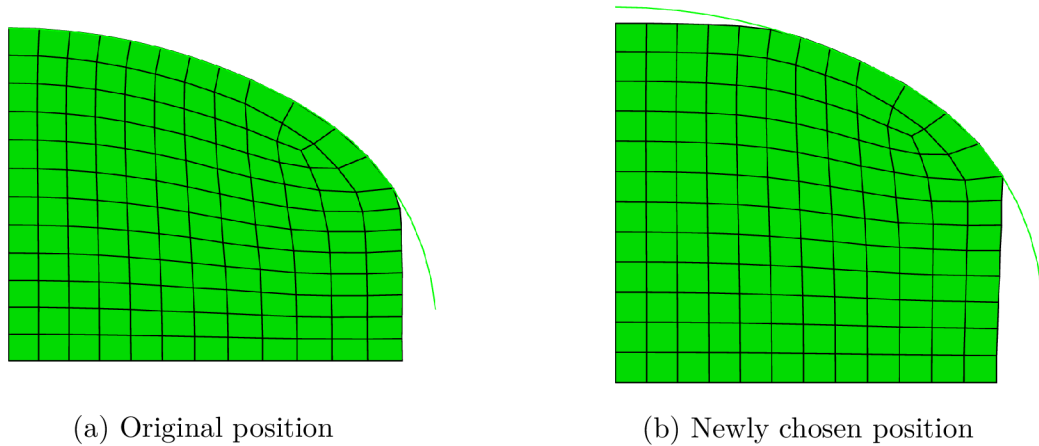
Figure 8.6: Deformed shape of the workpiece at section III of the full model

As may be seen on Fig. 8.7, plane of evaluation was adjusted in a similar manner for the simplified model.

(a) Original position

(b) Newly chosen position

Figure 8.7: Deformed shape of the workpiece at section III of the simplified model

Comparison of acquired results with available experimental and original computational results may be found below. All results are evaluated in section III of passage through the first roll pass.

8.3.1 Equivalent stress

Distribution of Mises equivalent stress may be seen on Fig. 8.8 and 8.9. Unfortunately, results obtained from original computational model were not included in [22].
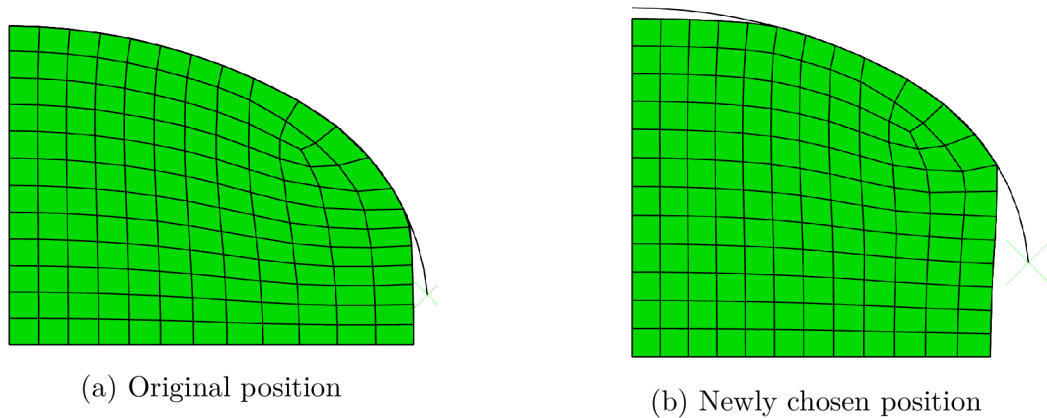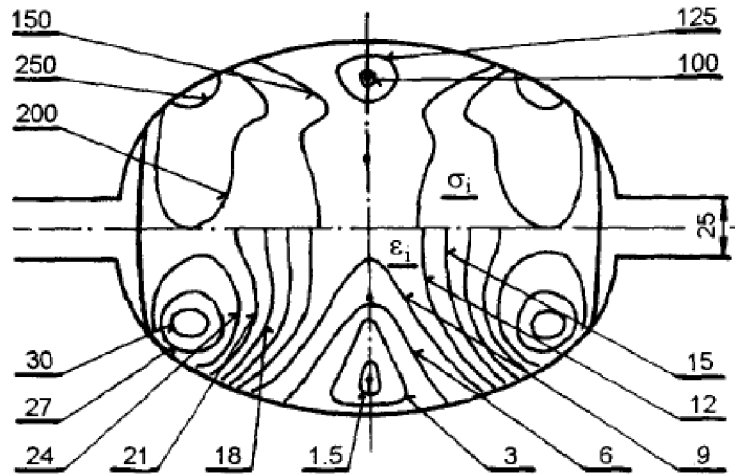

Figure 8.8: Experimental equivalent stress [MPa] and plastic strain [%] distribution [22]

(a) Full model   (b) Simplified model
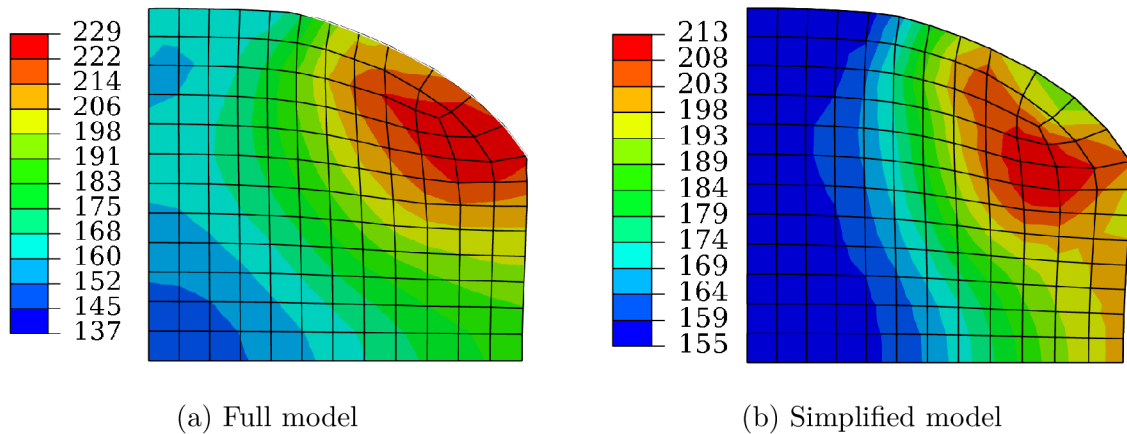
Figure 8.9: Distribution of equivalent stress [MPa]

As may be seen, all of the displayed distributions are similar but surprisingly, results obtained from the full model were closer to experimental ones. Maximum value obtained from experimental solution was higher than other values.

8.3.2 Stress in X direction

Distribution of stress in X direction may be seen on Fig. 8.10 and 8.11. Experimental results were not included in [22].

Figure 8.10: Original distribution of stress in X direction [MPa] [22]

(a) Full model   (b) Simplified model

Figure 8.11: Distribution of stress in X direction [MPa]

In general, all models yielded similar distributions. The minimum value, i.e. maximum compressive stress value was higher in both new models, especially the full model.

8.3.3 Stress in Y direction

Distribution of stress in X direction may be seen on Fig. 8.12 and 8.13. Experimental results were not included in [22].

Figure 8.12: Original distribution of stress in Y direction [MPa] [22]

(a) Full model

(b) Simplified model

Figure 8.13: Distribution of stress in Y direction [MPa]

    As predicted, results from simplified model more closely correspond with the original values. Maximum compressive stress value from full model is notably higher than other results.

8.3.4 Stress in Z direction

Distribution of stress in Z direction may be seen on Fig. 8.14 and 8.15. Experimental results were not included in [22].
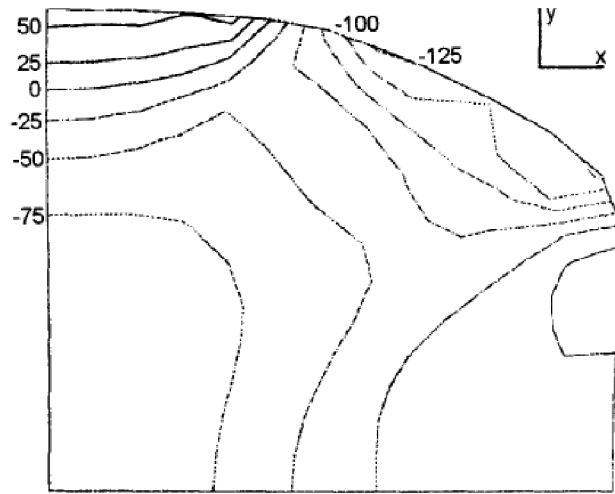

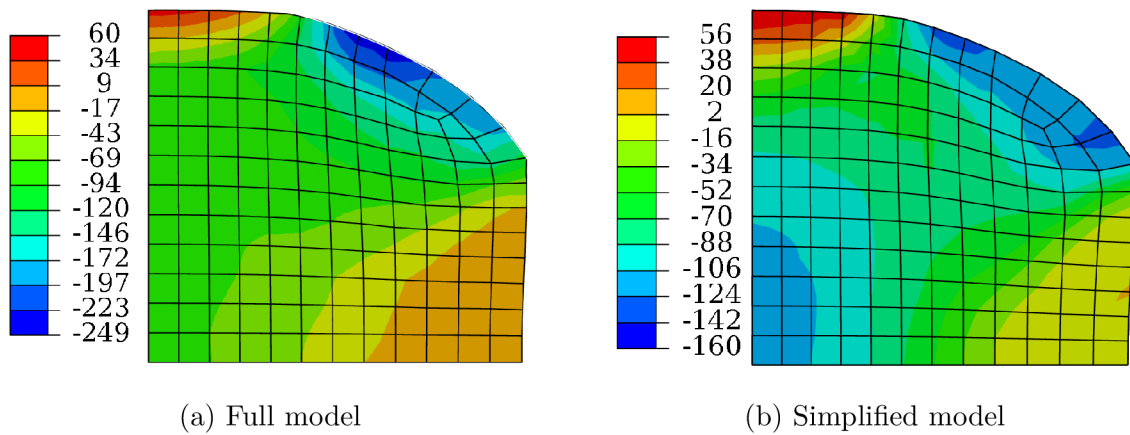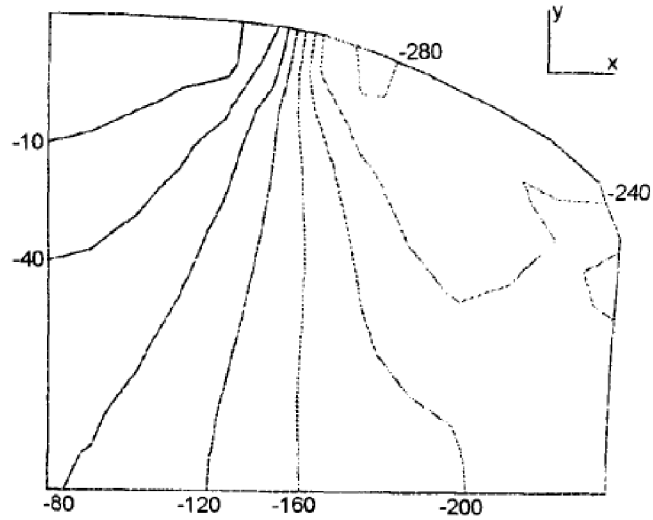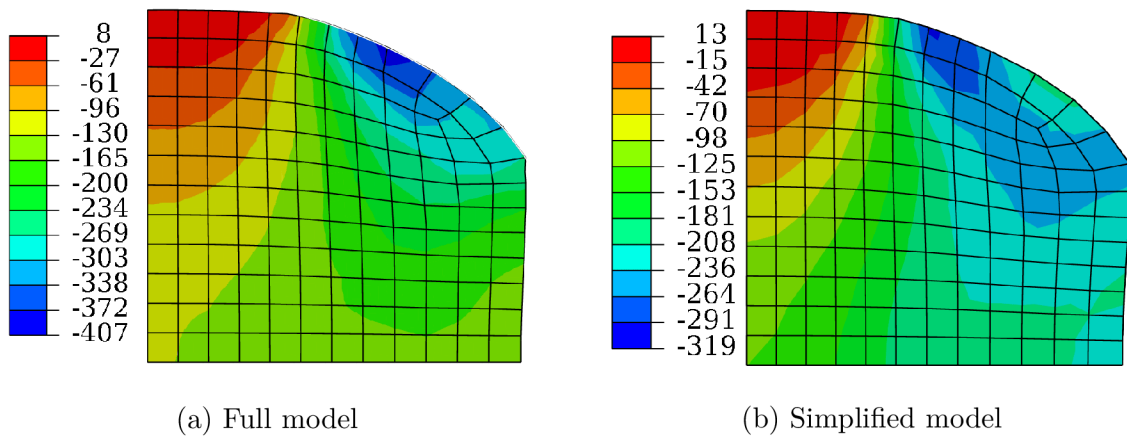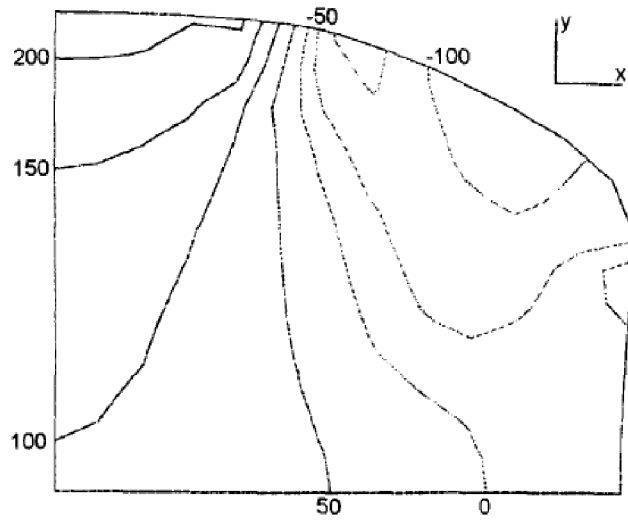Figure 8.14: Original distribution of stress in Z direction [MPa] [22]

(a) Full model   (b) Simplified model
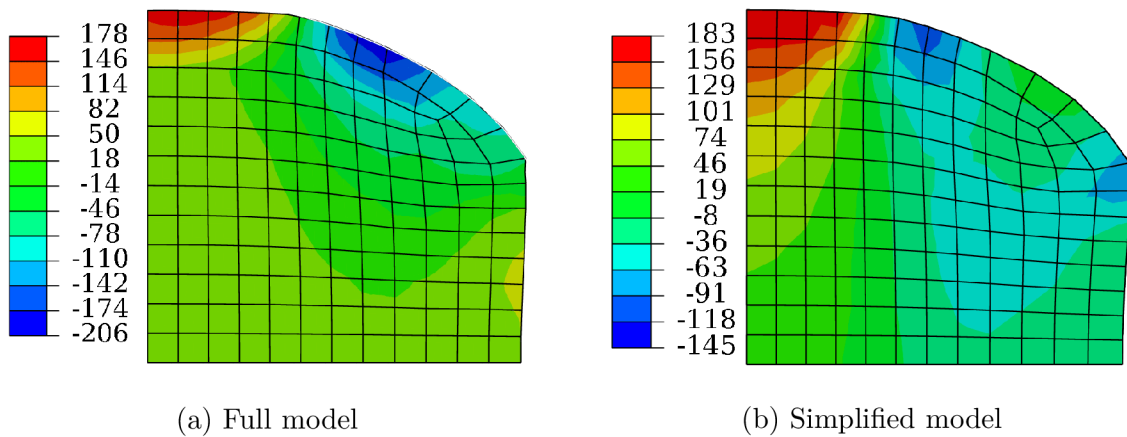
Figure 8.15: Distribution of stress in Z direction [MPa]

Distribution acquired from simplified model more closely corresponds with the original values. Maximum compressive stress values from both new models are higher than the original one.

8.3.5 Equivalent plastic strain

Distribution of Mises equivalent plastic strain may be seen on Fig. 8.16 and 8.17 below. Experimental results were shown on Fig. 8.8 in Sec. 8.3.1.
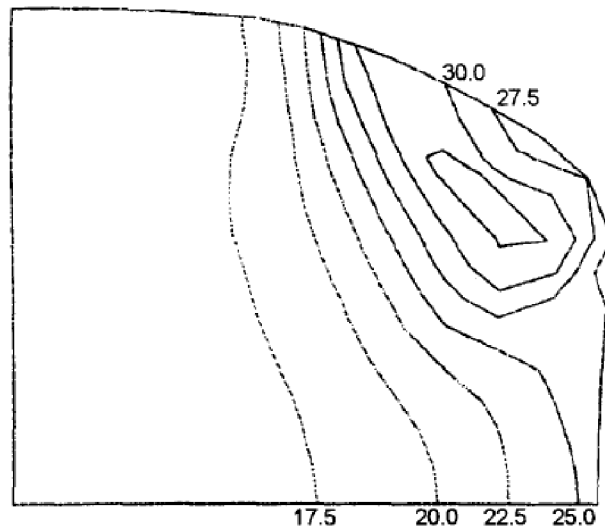
Figure 8.16: Original distribution of equivalent plastic strain [%] [22]

| (a) Full model | (b) Simplified model |
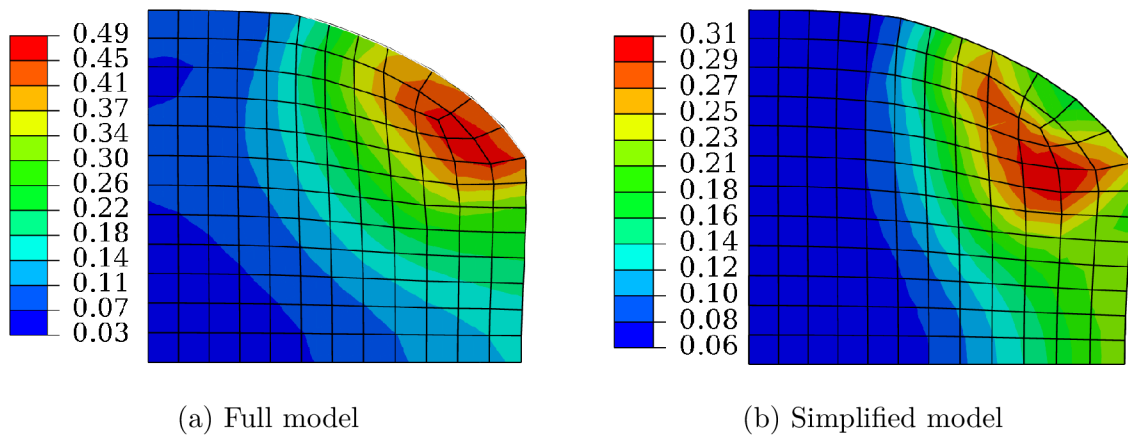
Figure 8.17: Distribution of equivalent plastic strain [%]

This comparison has shown a notable difference in maximum value of equivalent plastic strain obtained from the analysis with full model and the other results, which almost ideally correspond with each other. In order to determine the cause of this variation, individual normal and shear components of plastic strain were evaluated and compared for both full and simplified model.
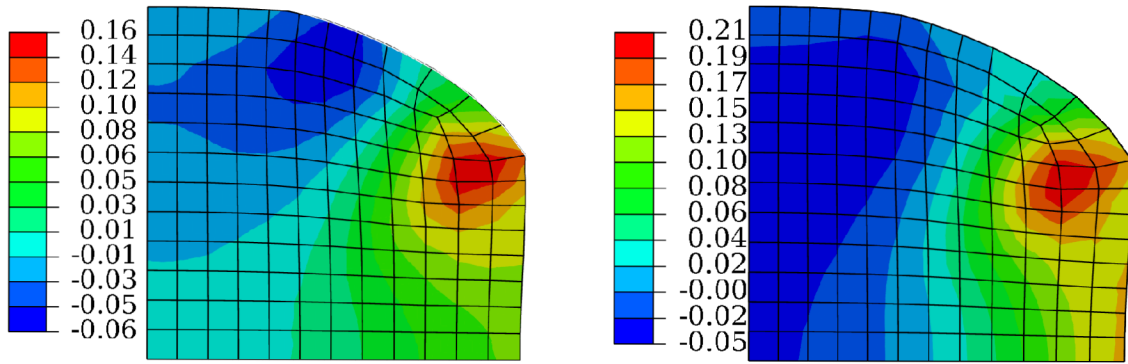
(a) Full model

(b) Simplified model

Figure 8.18: Distribution of plastic strain in X direction [%]
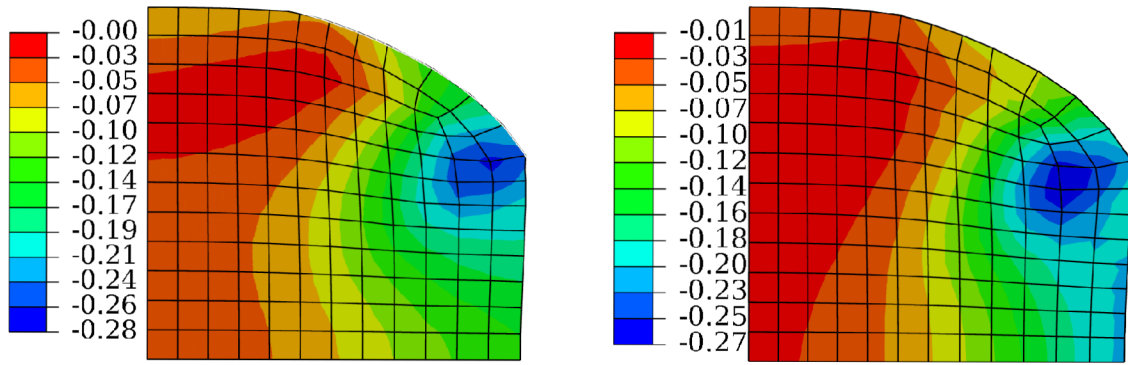
(a) Full model

(b) Simplified model

Figure 8.19: Distribution of plastic strain in Y direction [%]
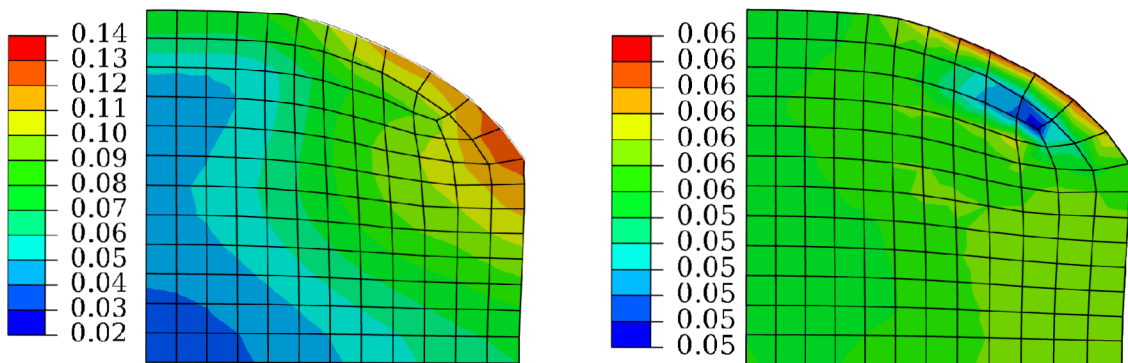
(a) Full model

(b) Simplified model

Figure 8.20: Distribution of plastic strain in Z direction [%]

81
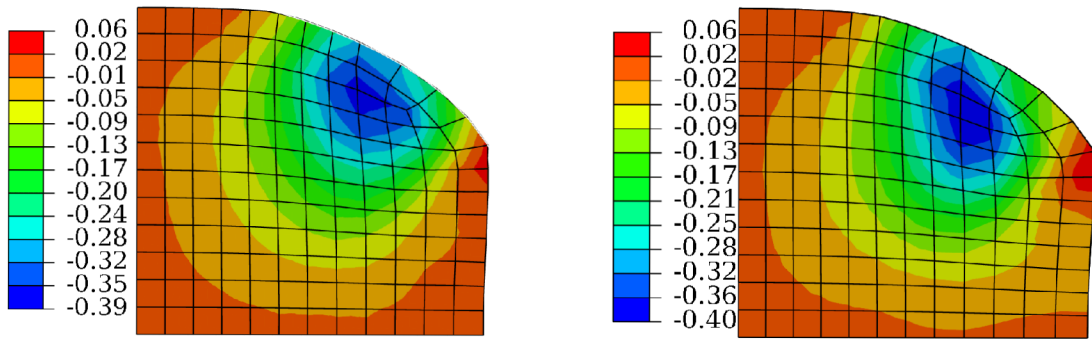
(a) Full model

(b) Simplified model

Figure 8.21: Distribution of shear plastic strain in XY direction [%]
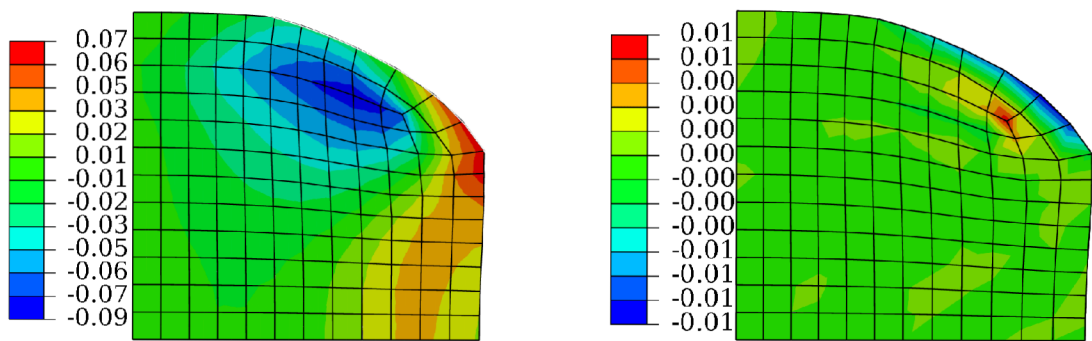
(a) Full model

(b) Simplified model

Figure 8.22: Distribution of shear plastic strain in XZ direction [%]
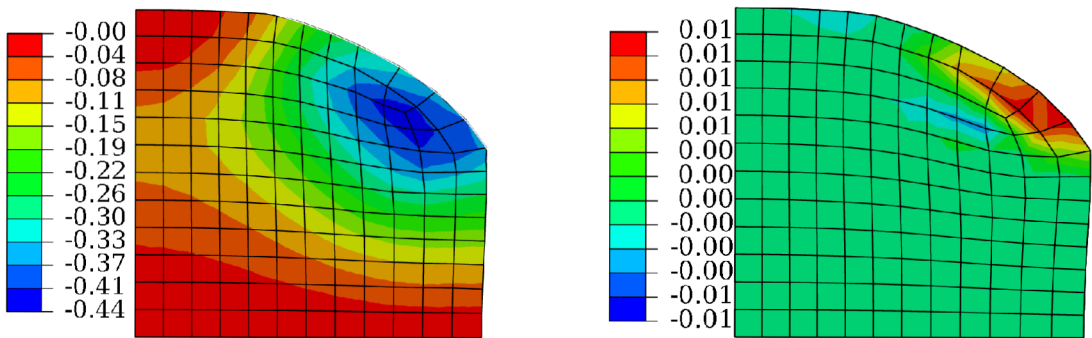
(a) Full model

(b) Simplified model

Figure 8.23: Distribution of shear plastic strain in YZ direction [%]

As expected, strain in X direction (see Fig. 8.18), Y direction (see Fig. 8.19) and shear strain in XY direction (see Fig. 8.21) were mostly similar, whereas strain in Z direction (see Fig. 8.20) and shear strain in XZ (see Fig. 8.22) and YZ direction (see Fig. 8.23) were notably lower for the simplified model. This was caused by geometry of the simplified model.

8.4 Stress along symmetry lines

Stresses along symmetry lines at section III of passage through the first rolling gap were evaluated from the full and simplified model in order to be compared to experimental values. These comparisons may be seen on Fig. 8.24 and 8.25.

(a) Stress in X direction [MPa]

(b) Stress in Y direction [MPa]
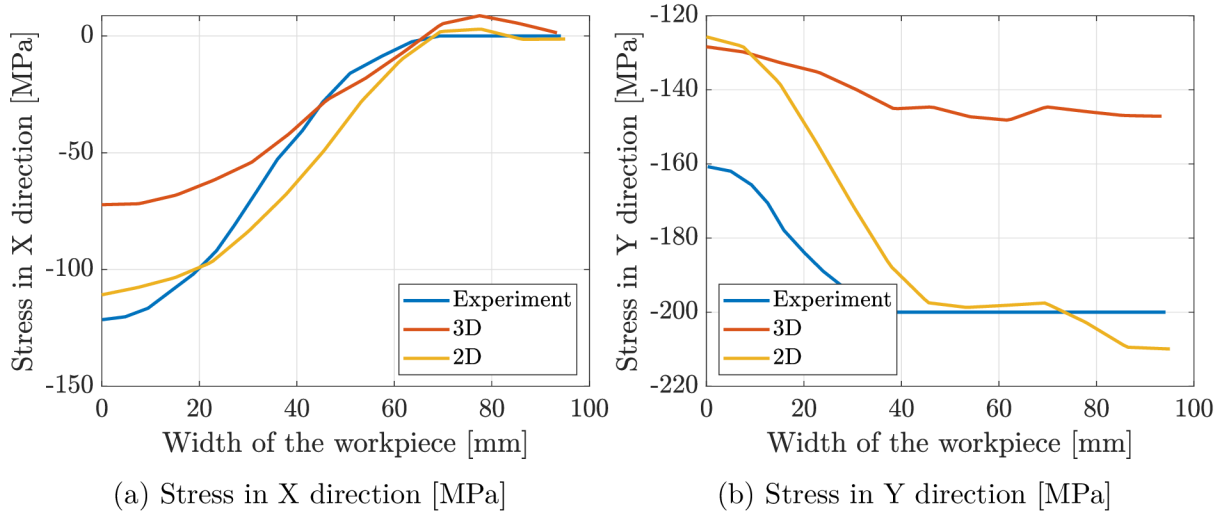
Figure 8.24: Stresses along horizontal symmetry line

(a) Stress in X direction [MPa]

(b) Stress in Y direction [MPa]
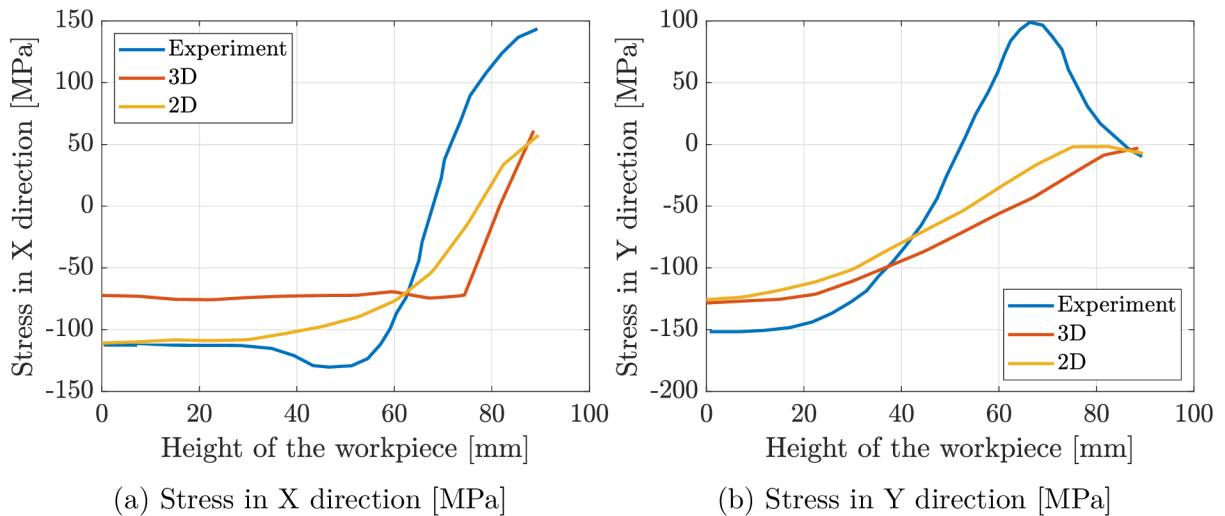
Figure 8.25: Stresses along vertical symmetry line

As expected, results from the simplified model correspond more closely with the experiment. As seen on Fig. 8.24b, stress values obtained the 3D model were considerably lower in comparison with the other results. Tensile stresses near the surface of the workpiece obtained from the experiment (see Fig. 8.25b) were not present in any of other analyses. Other than that, trends obtained from all sources were similar.

8.5 Stress triaxiality factor

Values of stress triaxiality factor were evaluated at three points of the cross section of the workpiece for passages through each rolling gap, same as in [22]. Instead of deformation zone length, position in Z direction was used as independent variable on each chart. Since movement in Z direction does not occur in analyses with the simplified models, artificial values of Z coordinates were used to include their results in the comparison.

It should be noted that while other results are presented up to 0 mm and 700 mm, which are positions of the narrowest parts of rolling gaps, results from analysis with the full model continue further as the workpiece emerges from the rolling gap.

(a) Passage through oval roll pass   (b) Passage through circular roll pass
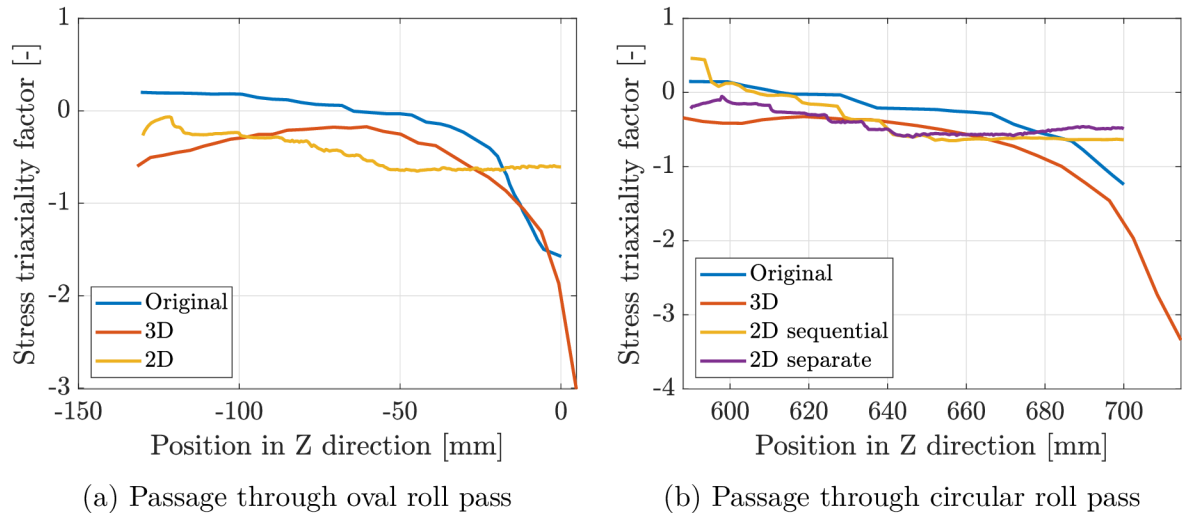
Figure 8.26: Stress triaxiality values at point C for passages through both rolling gaps

At point C, results for which may be seen on Fig. 8.26, similar values of stress triaxiality were observed, the only exception being the simplified models, where further decrease near the end of loading did not occur. On Fig. 8.26b, high values of stress triaxiality obtained from analysis with the simplified model may be observed near the start of the loading. This should not be taken into account, as it is caused by unloading of the simplified roll pass model, which does not represent any real process.

(a) Passage through oval roll pass

(b) Passage through circular roll pass
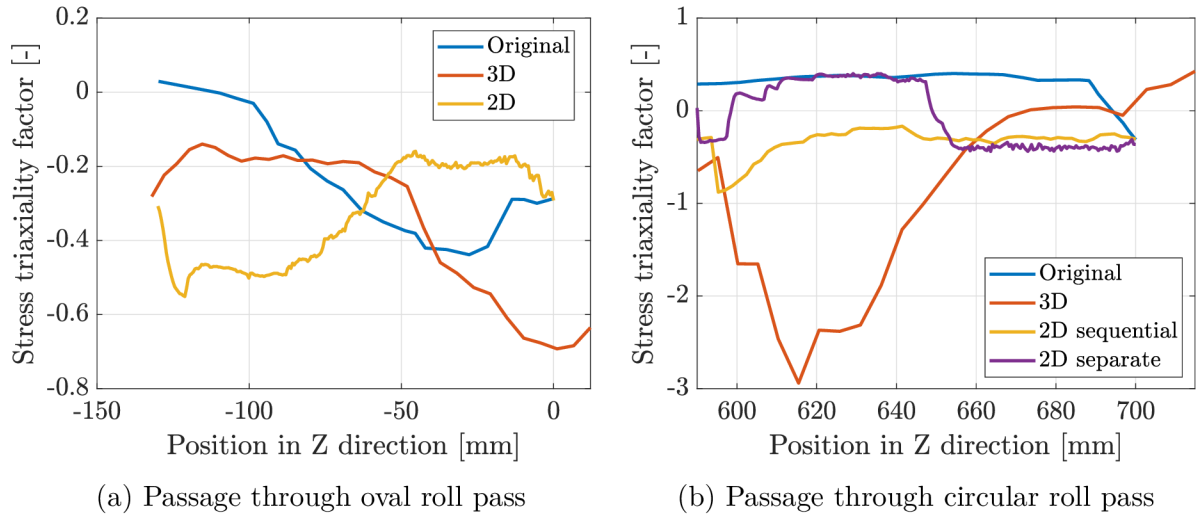
Figure 8.27: Stress triaxiality values at point X for passages through both rolling gaps

Results at point X for passage through the first rolling gap, which may be seen on Fig. 8.26a, exhibit different trends of stress triaxiality for each model. In the simplified model, stress triaxiality value grows due to sudden increase of tensile stress in Z direction, whereas in the full model, stress triaxiality decreases as compressive stress is generated.

For passage through the second rolling gap, seen on Fig. 8.27b, stress triaxiality assumes negative values for the full model as the workpiece is compressed. Subsequently, its value gradually increases, reaching positive values when as the workpiece emerges from the rolling gap. This is due to area near the contact surface being pulled in rolling direction, which does not occur in either of the simplified models. The variance of stress triaxiality courses in the sequential and separate model are caused by different shapes of used workpiece (see Fig. 8.28). In the sequential model, initial contact occurs at point X, immediately causing negative stress triaxiality values, whereas in the separate model, initial contact occurs on the corner of the workpiece. Positive stress triaxiality values are present at point X until contact occurs there, which is around 650 mm.

(a) Sequential model

(b) Separate model
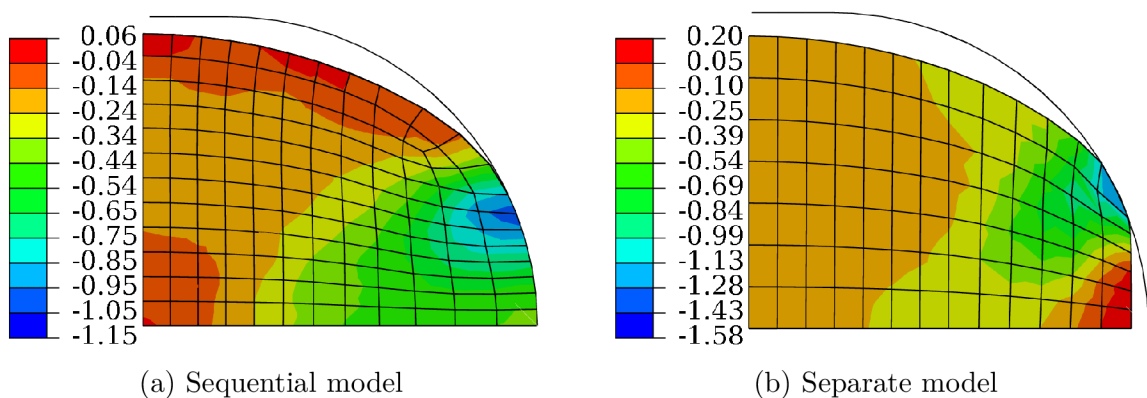
Figure 8.28: Distribution of stress triaxiality factor [-] after initial contact of circular roll pass and the workpiece during filling of the second rolling gap for the simplified models

(a) Full model

(b) Simplified model
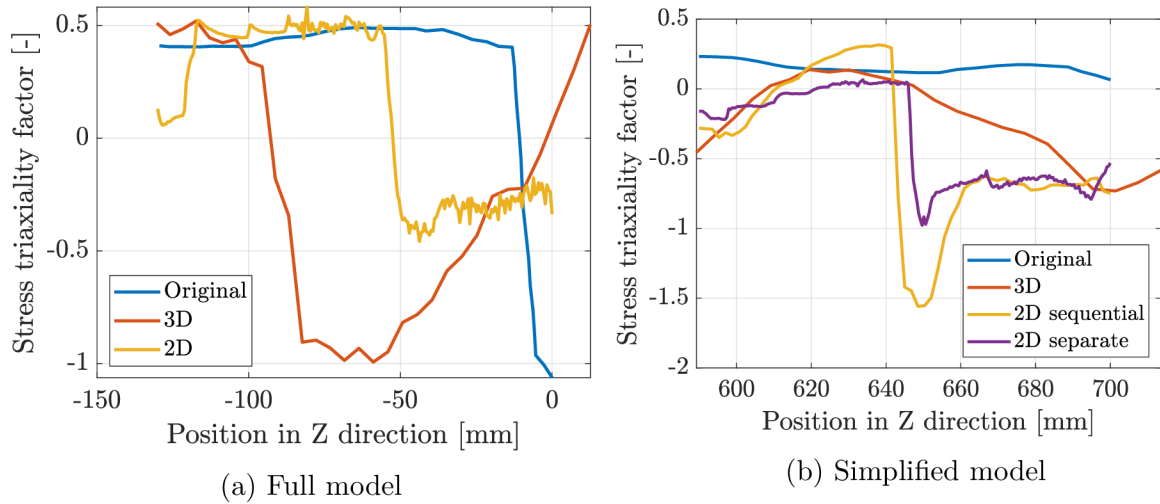
Figure 8.29: Stress triaxiality values at point Y for passages through both rolling gaps

Results at point Y for passage through the first rolling gap may be seen on Fig. 8.26a. Positive values of stress triaxiality are present for each case (see Fig. 8.30) until the rolling gap is filled and contact at point Y occurs, which is around -120 mm for the full model, -50 mm for the simplified model and -20 mm for the original model. Compressive stresses in Y direction then cause negative values of stress triaxiality. In the full model, values of stress triaxiality subsequently rise as area surrounding the interface is pulled into the rolling gap.

(a) Full model

(b) Simplified model
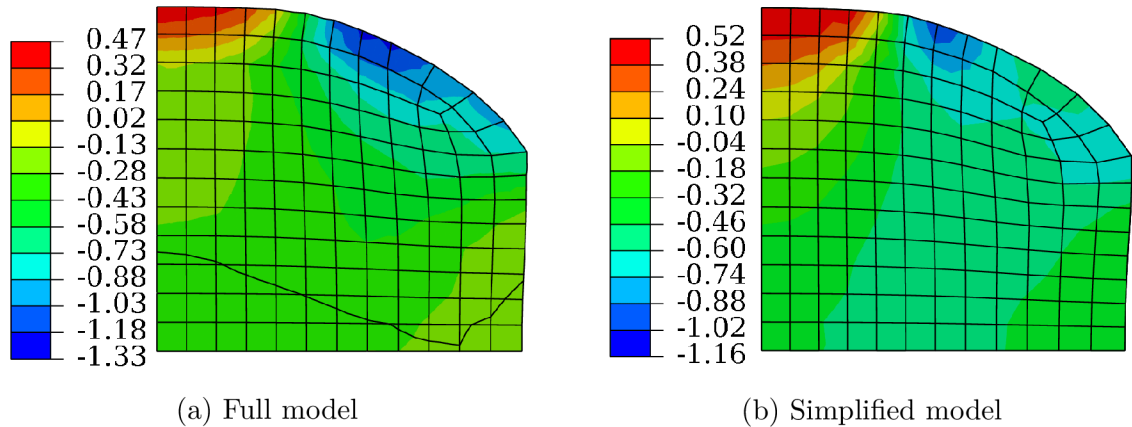
Figure 8.30: Distribution of stress triaxiality factor [-] during filling of the first rolling gap

For passage through the second rolling gap (see Fig. 8.29b), values of stress triaxiality grow as the rolling gap is filled with material and lower around 640 mm when contact at point Y occurs, similar to previously mentioned point X. For the full model, the value decreases gradually, whereas for both simplified models it happens abruptly, due to artificial elongation of the circular roll pass model. If this elongation was not included, the results would probably be closer to those from the full model.

8.6 Formability assessment

Assessment of material formability, i.e. evaluation of possibility of material damage occurence was carried out at the same three points where stress triaxiality factor was evaluated earlier. Two approaches were utilized, with the damage supossed to occur when value of 1 is reached for either of them.

The first means of evaluation was based on comparison of equivalent plastic strain to equivalent plastic strain at fracture, dependent on the current value of stress triaxiality. On the charts below, these are denoted as 'PEEQ', 'PEEQ$_f$' and 'TRIAX', respectively. Instead of comparing the two curves as in [22], their ratio was evaluated instead.

For the second approach, ductile damage criterion was employed, value of which is denoted as 'DUCTCRT' on following charts. Damage envelope defined by eq. 5.13 in Sec. 5.3 was used. The fracture curve may be seen on Fig. 4.5 in Sec. 4.3.2. No temperature or rate dependency was defined.

Comparison of values of both criteria acquired from available models may be seen on Fig. 8.31, 8.32, 8.33, 8.34, 8.35 and 8.36 below.
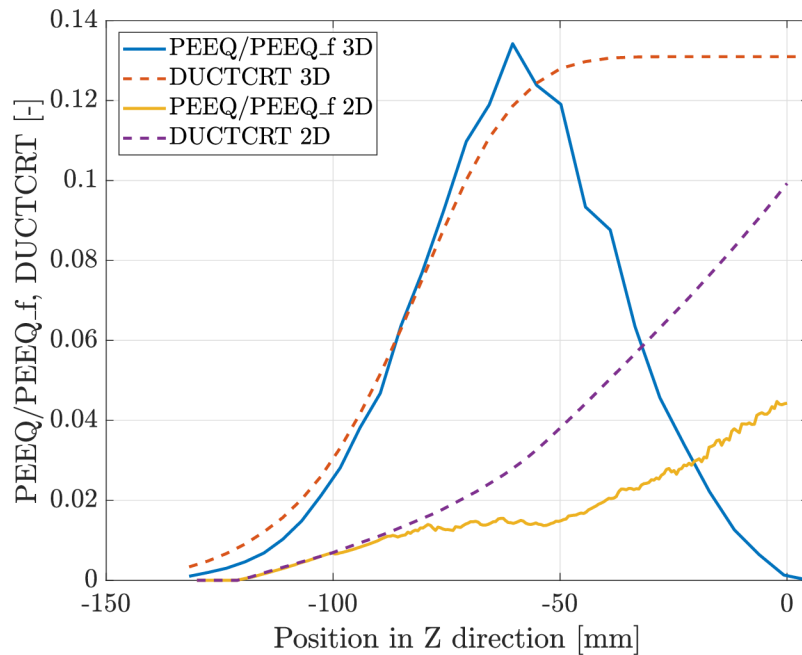
Figure 8.31: Values of damage criteria at point C for passage through the first rolling gap
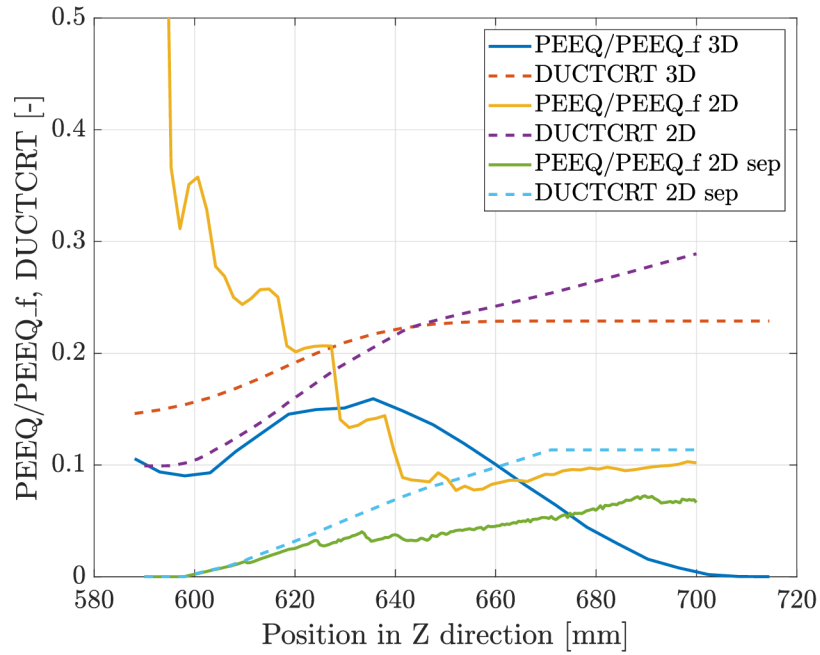
Figure 8.32: Values of damage criteria at point C for passage through the second rolling gap
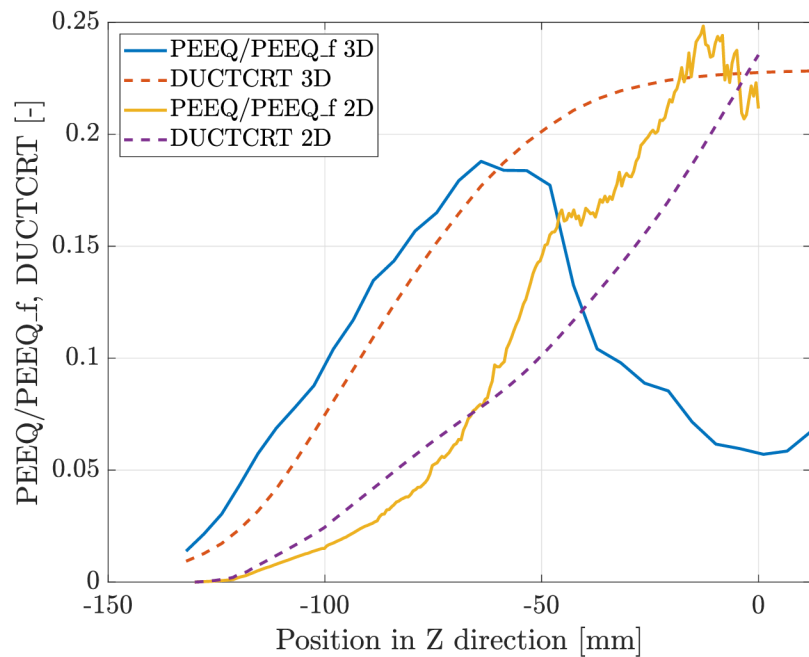
Figure 8.33: Values of damage criteria at point X for passage through the first rolling gap
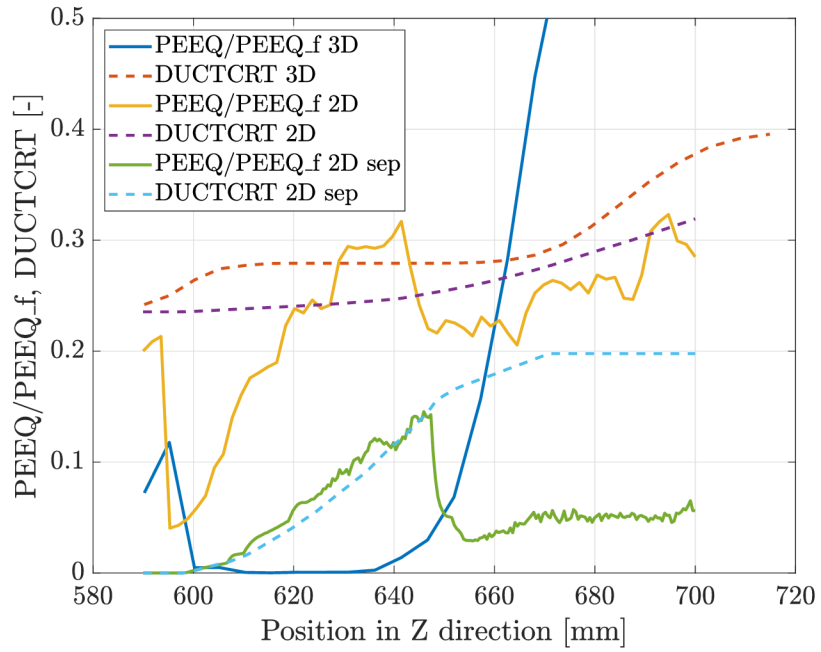
Figure 8.34: Values of damage criteria at point X for passage through the second rolling gap
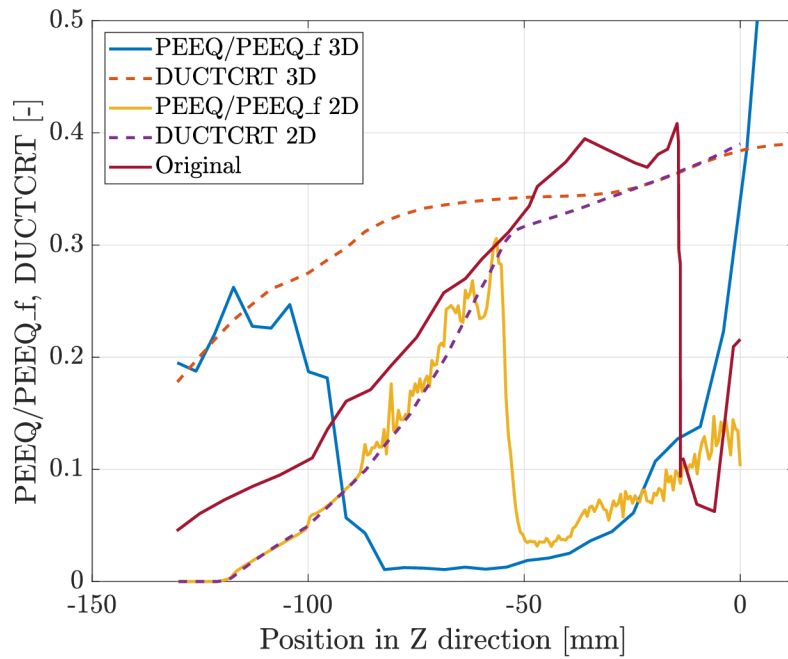
Figure 8.35: Values of damage criteria at point Y for passage through the first rolling gap

89
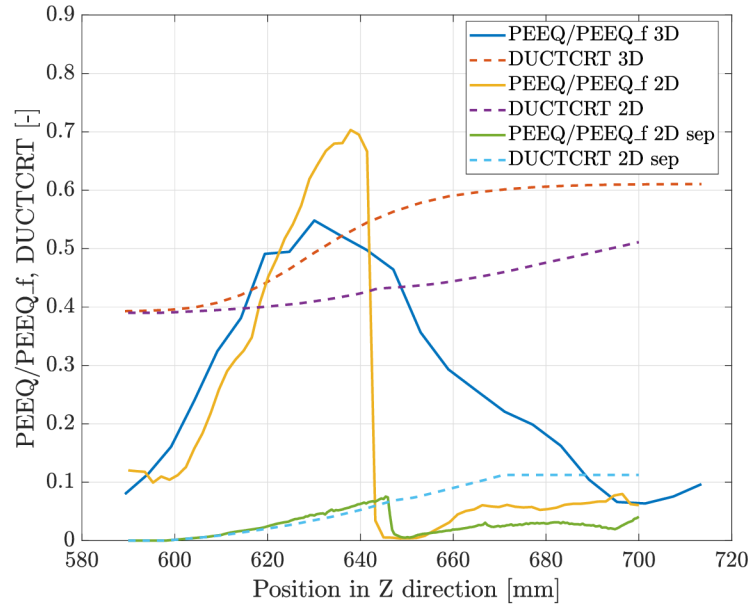
Figure 8.36: Values of damage criteria at point Y for passage through the second rolling gap

On Fig. 8.34 and 8.35, maximum values of PEEQ to $PEEQ_f$ curves are cut off. In case of point Y (see Fig. 8.37), this curve reaches values higher than 200 after the workpiece leaves the first rolling gap, whereas the value of DUCTCRT does not increase due to the fact that plastic straining is not active at the time. This is the main difference between the criteria, as the PEEQ to $PEEQ_f$ ratio does not require active plastic straining in order to increase, which does not correspond with reality. It only describes the actual state of the material, not respecting the loading process as a whole. For these reasons, PEEQ to $PEEQ_f$ ratio can not be used as a damage criterion. That must always be based on accumulated plastic strain, as in case of ductile damage criterion.
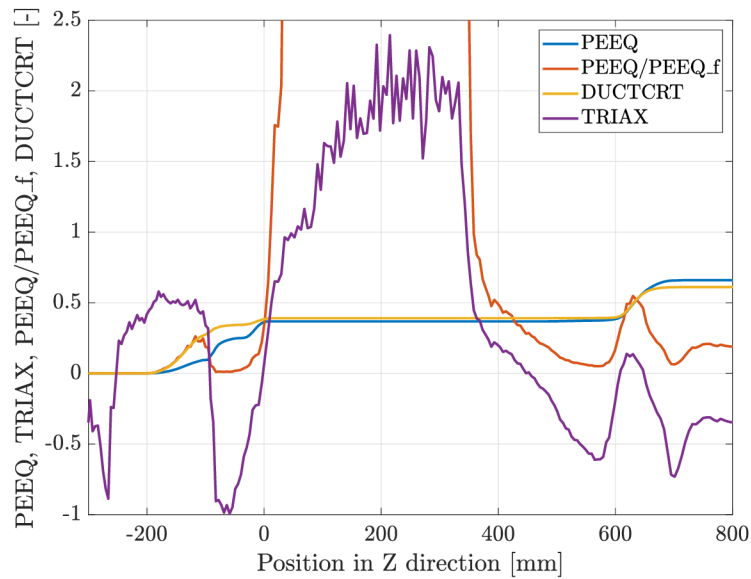
Figure 8.37: Value of damage criteria at point Y for full duration of the analysis

In addition, distribution and maximum values of DUCTCRT were evaluated on cross sections of deformed workpieces 100 mm beyond the narrowest part of each rolling gap, that being 100 mm and 800 mm.

(a) First roll pass

(b) Second roll pass
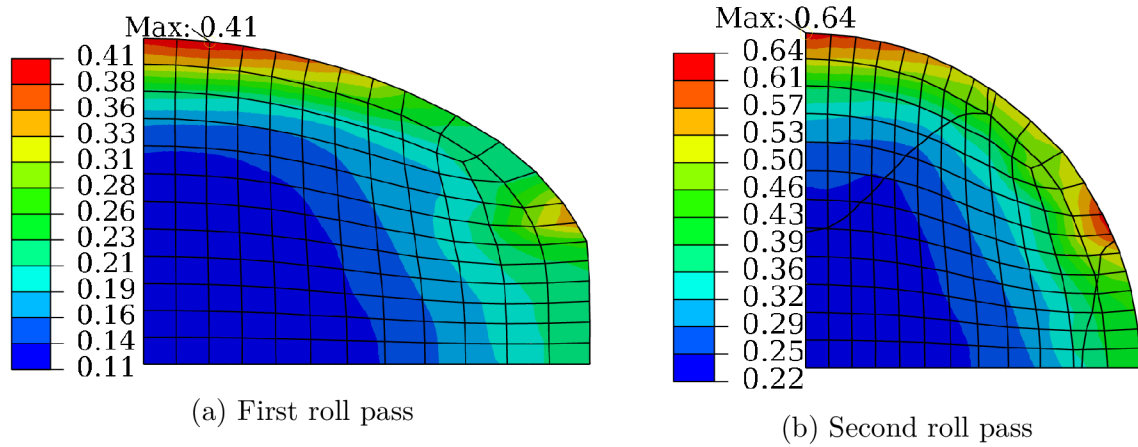
Figure 8.38: Distribution of DUCTCRT [-] obtained from the full model

(a) First roll pass

(b) Second roll pass
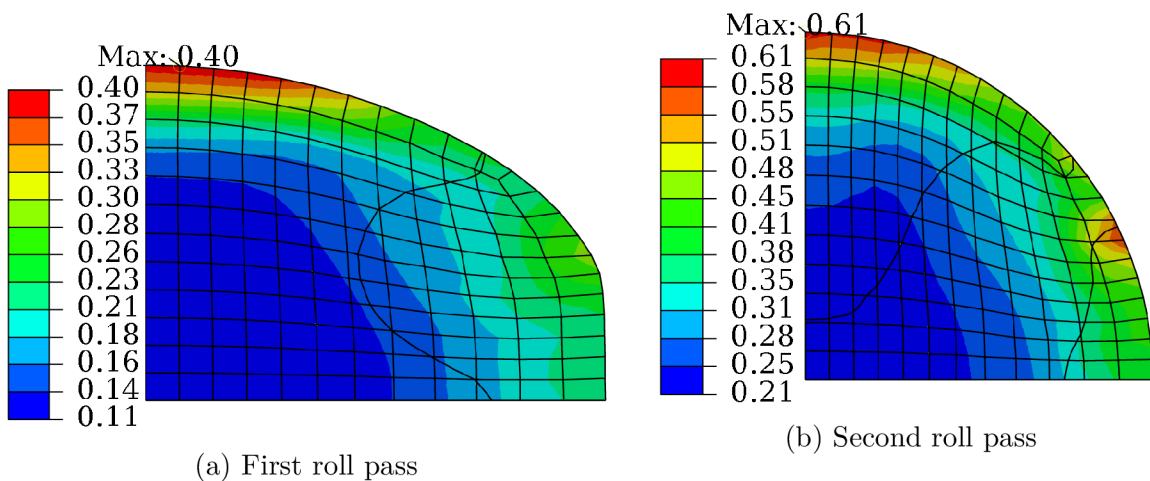
Figure 8.39: Distribution of DUCTCRT [-] obtained from the full model with refined mesh

According to results obtained from analysis of the full model (see Fig. 8.38), maximum value is located near point Y. An additional local peak, situated on the edge of the contact surface, reaches values close to the maximum during passage through the second roll pass (see Fig. 8.38b). Mesh refinement of the workpiece (see Fig. 8.39) resulted in peak at the edge of the contact surface being less prominent for passage through the first rolling gap, as well as a slight decrease of maximum value for passages through both rolling gaps.

(a) First roll pass

(b) Second roll pass
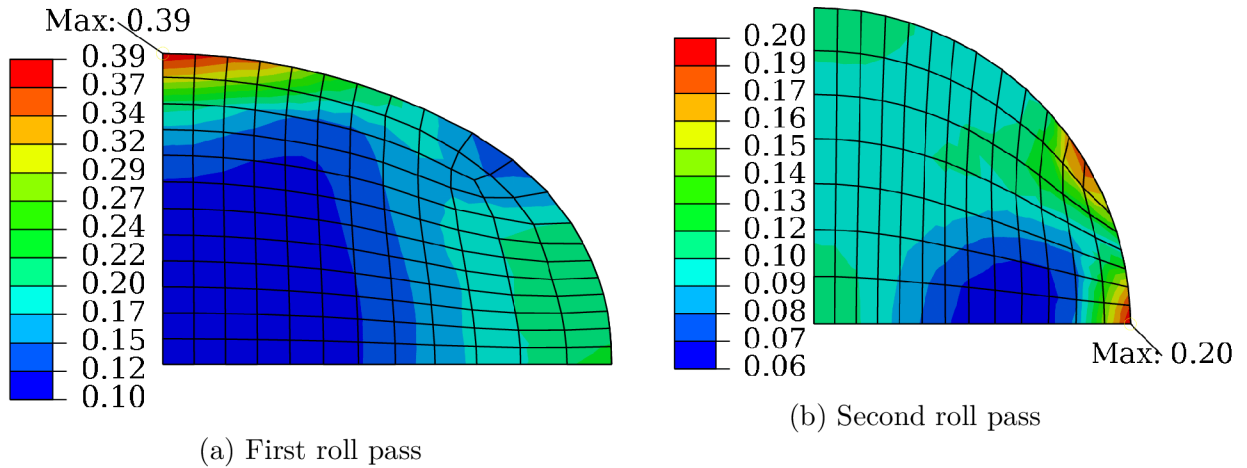
Figure 8.40: Distribution of DUCTCRT [-] obtained from the separate model

Analysis of the simplified model yielded maximum value almost equal to that of the full model, located directly at point Y (see Fig. 8.40a). Maximum value obtained from separately analysed passage through the second roll pass (see Fig. 8.40b) was notably lower and located at point X. An additional peak is situated at former location of corner of used model of workpiece.
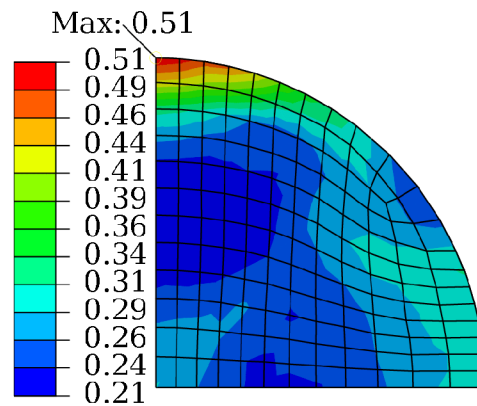
Figure 8.41: Distribution of DUCTCRT [-] obtained from the sequential model

Sequential analysis of passage through the second rolling gap (see Fig. 8.38b) yielded results much more resembling those of the full model. As may be seen on Fig. 8.42, mesh refinement yielded results closely similar to the result obtained with original mesh.

Max: 0.39

0.39
0.37
0.34
0.32
0.29
0.27
0.25
0.22
0.20
0.17
0.15
0.12
0.10

(a) First roll pass

Max: 0.52

0.52
0.49
0.47
0.44
0.42
0.39
0.37
0.34
0.32
0.29
0.27
0.24
0.22

(b) Second roll pass
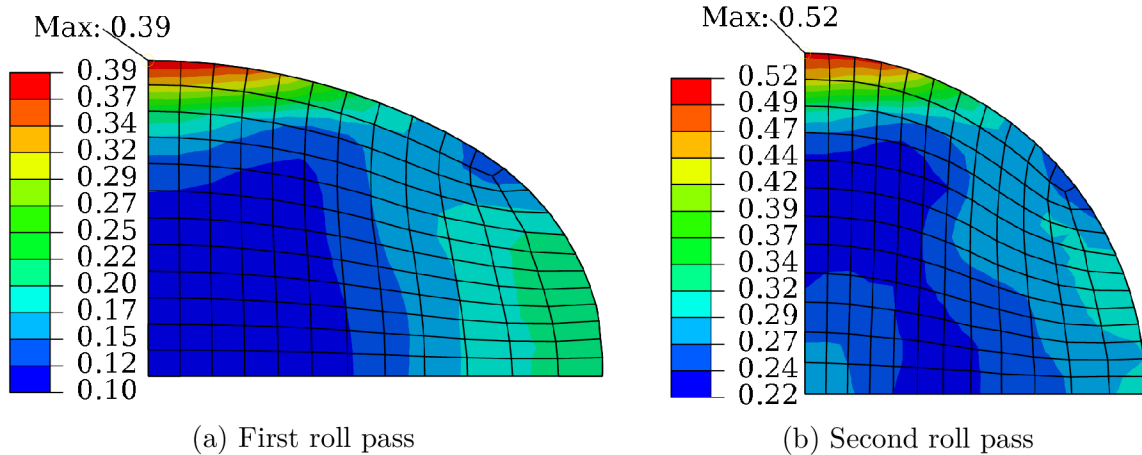
Figure 8.42: Distribution of DUCTCRT [-] obtained from the sequential model with refined mesh

An overall summary of equivalent plastic strain, stress triaxiality factor, PEEQ to PEEQ$_f$ ratio and ductile damage criterion values for each of the analysed cases may be found in Tab. 8.2. Results obtained with the original mesh variant are included there. Maximum values of both damage criteria for each case is displayed in bold. It may be seen that at point Y, sum of DUCTCRT from both roll passes closely resembles result from the sequential model. It should also be noted that no value obtained from analysis of the full model beyond position of 0 mm and 700 mm is taken into account. The same goes for value 0,91 at point C, obtained from the sequential model, not taken into account, which was explained in Sec. 8.5.

Table 8.2: Values of variables associated with evaluation of material damage

Max. value [-]	Position	Original 1.	Original 2.	Full 1.	Full 2.	Separate 1.	Separate 2.	Sequential 2.
TRIAX	C	0,20	0,15	-0,17	-0,33	-0,07	-0,05	0,46
	X	0,03	0,40	-0,14	0,43	-0,16	0,40	-0,17
	Y	0,49	0,23	0,52	0,14	0,58	0,07	0,32
PEEQ	C	-	-	0,34	0,65	0,32	0,347	0,81
	X	-	-	0,53	0,83	0,63	0,21	0,88
	Y	0,22	-	0,37	0,66	0,35	0,24	0,66
	Total	-	-	0,81	1,26	0,73	0,43	1,02
$\frac{PEEQ}{PEEQ_f}$	C	-	-	0,13	0,16	0,04	0,07	0,91
	X	-	-	0,19	**0,9**	0,25	0,15	0,32
	Y	**0,41**	-	0,34	0,55	**0,31**	0,08	**0,7**
DUCTCRT	C	-	-	0,13	0,23	0,01	0,11	0,29
	X	-	-	0,23	0,40	0,24	0,20	0,32
	Y	-	-	0.39	**0,64**	**0,39**	0,11	**0,51**
	Total	-	-	0,41	0,64	0,39	0,20	0,51

9 Conclusion

This master's thesis is focused on possibilities of finite element modelling of pass rolling, comparing a simplified computational model used in previous research with a contemporary one. It begins with a short introduction, formulation of the problem and subsequent definition of system of essential variables. In the next chapter, the reader was introduced to basics of rolling technology as well as traditional approach to roll pass design, which is composed of multiple analytical and empirical procedures. Next chapter dealt dealt with models of plasticity and material damage, essential for modelling of plastic behavior and assessment of material formability. Following chapters introduced and described other methods of pass rolling analysis, namely experimental method of photoelasticimetry and finite element method. Emphasis was put on its explicit algorithm, which was later employed in the computational part of the thesis. Description of photoplastic experiment and finite element analysis of a rectangular bar passing through oval and circular roll pass, carried out in previous research, was also included.

A total of three computational models were created, all of which used dimensions, material, contact conditions and other parameters specified in the original paper. First of these was the full simulation, employing actual geometry of the rolls and the workpiece. The other two were models with simplified geometry, based on original model, one of them respecting loading history of passages through both rolling gaps, while the other not. For both simplified models, model of the second roll pass needed to be slightly elongated in order to prevent the material from flowing out of the rolling gap, which occured in both cases. Since only partial information about the original computational model was available, direct cause of this problem was not determined.

Elastic-plastic model with isotropic hardening was used. Constant temperature was assumed, its effect included in the flow curve for reference temperature and strain rate.

To recreate the original model as closely as possible, similar finite element mesh was used. Even so, several refined mesh variants were created and mesh convergence study was carried out to determine the effect that the element size might have had on the results. It has proven that for the three distinct points where results were evaluated, original mesh was appropriate.

Since the material of the workpiece was not dependent on strain rate, nor was the velocity of its movement specified in the original article, a reasonable value of angular velocity was chosen for the first roll pass. Subsequently, law of continuity was used to obtain value of angular velocity for the second roll pass to ensure optimal flow of the material through the rolling gap. To ensure that no notable dynamic effects were present in any of the analyses, nor that the results were affected by hourglassing deformation, values of total strain energy were compared kinetic and artificial strain energy. This comparison has proven reliability of the results in this matter.

Except the inconvenience with inaproppriate material flow, solved by elongation of circular roll pass, creation of used computational models was considered successful.

Structural analyses were carried out using each of these models, yielding variety of results. While analyses with the full model took hours to finish, those with the simplified models were completed in matter of minutes. Firstly, stress and plastic strain distribution throughout cross section of the workpiece at a specific stage of loading process, included in the original paper, was compared with the newly values acquired. There was a notable difference between equivalent plastic strain values, prompting evaluation of components

of plastic strain for the full and simplified model. As expected, the main difference lay in the normal and shear strains in the rolling direction, values of which were significantly lower due to applied geometry simplifications.

Values of stress triaxiality, which is essential in assessment of material formability, were evaluated at three points of the cross section, in accordance with the original article. Its courses were notably affected by the course of filling of rolling gap. Highest values were present in zones where contact with the roll pass has not occured yet. As soon as the contact was commenced, compressive stresses caused stress triaxiality values to drop below zero. For the full model, high values of stress triaxiality occured due to the workpiece being pulled in rolling direction.

Assessment of material formability was was first carried out using actual plastic strain and stress triaxiality values, as in the original paper, and then with usage of ductile damage criterion, implemented in the finite element post-processor.

The main difference between the two approaches lies in the cumulative character of ductile damage criterion value, which requires active plastic straining in order to grow, whereas the ratio of actual and limit plastic strain for current value of stress triaxiality does not. This was most notable in the unloading phase, i.e. when the workpiece emerged from the rolling gap. Even though plastic straining was not active at the time, high values of stress triaxiality caused massive growth of the value of the criterion, exceeding the critical value multiple times. In general, this approach should be avoided and only cumulative damage criteria should be used.

Results obtained from the sequential simplified model were closest to the full model, which yielded the highest value of ductile damage criterion. However, even though damage initiation was predicted in the same location, an additional possible place of damage occurence near the edge of the contact surface was indicated only by the latter of the two.

As expected, analysis of separate simplified model yielded results closest to the original computational model. Distribution of values of ductile damage criterion did not correspond with any of the previous results. Also, its maximum value was notably lower due to absence of plastic strain accumulated during passage through the first roll pass, as the loading history was not respected. As opposed to all other models, maximum value of ductile damage criterion occured during passage through the first rolling gap.

Structural analyses carried out in this thesis could be further enhanced by using temperature dependent material, instead of the effect of temperature being included in the flow curve. With correct data at disposal, parameters of Johnson–Cook plasticity with temperature dependency could be determined. Workpiece would be heated before the rolling process and structural–thermal analysis could be carried out. Effect of hardening associated with temperature decreasing throughout the process could be studied this way. Unfortunately, flow curves of ČSN 41 17246 stainless steel at various temperatures weren't available to the author and thermal properties of the roll passes were not specified in the original paper.

Another possible improvement would be to employ a damage criterion with more complex fracture envelope. Provided that required data would be available, more accurate prediction of ductile damage could be achieved this way. However, most of these criteria do not include temperature dependency and therefore are not suitable for this purpose.

95

Bibliography

[1] JANÍČEK, P.: *Systémová metodologie: brána do řešení problémů.* Brno: Akademické nakladatelství CERM, 374 p., 2014. ISBN 978-80-7204-887-8.

[2] MOTT, R. A.: *Henry Cort, The Great Finer: Creator of Puddled Iron.* The Metals Society, 108 p., 1983. ISBN 978-0904357554.

[3] *Design for rolling mill by Leonardo da Vinci* [Online]. Science & Society: Picture library [Acessed on 2020-04-08]. Available from: https://www.scienceandsociety.co.uk/results.asp?image=10328964&itemw=4&itemf=0003&itemstep=1&itemx=1Davinci.

[4] HUGHES, C.: Heavy industry on the River Meon: Iron [Online]. 2018 [Accessed 2020-02-12]. Available from: https://carolynhughesauthor.com/2018/05/10/heavy-industry-on-the-river-meon-iron/cort2.

[5] KOLLEROVÁ, M., ŽÍDEK, M., POČTA, B., DĚDEK, V.: *Valcovanie.* Vydavateľstvo Alfa, Bratislava, 569 p., 1991. ISBN 80-05-00729-9.

[6] FABÍK, R.:*Tváření kovů* [online]. VŠB TU Ostrava, 333 p., 2012 [Accessed 2020-02-20]. Available from: http://www.person.vsb.cz/archivcd/FMMI/TVKB/Tvareni%20kovu.pdf.

[7] DEGARMO, P. E., BLACK, J. T., KOHSER, R. A.:*Materials and Processes in Manufacturing.* Wiley, 9th ed., 2003. ISBN 978-0-471-65653-1.

[8] *Thread rolling* [online]. Horst engineering [Acessed on 2020-02-24]. Available from: http://horstengineering.com/threadrolling/process/thread-rolling/.

[9] MILLER, R.: *Making seamless tubing with a floating mandrel mill* [online]. The tube & pipe journal, 2001 [Acessed on 2020-02-24]. Available from: https://www.thefabricator.com/tubepipejournal/article/tubepipeproduction/making-seamless-tubing-with-a-floating-mandrel-mill.

[10] *Steel ball skew rolling production process* [online]. Huihuang heavy equipment [Acessed on 2020-02-24]. Available from: http://rollingmillchina.com/productintro.asp?id=207.

[11] BLAŠKOVIČ, P.: *Tribológia.* Bratislava: Alfa, 1990. ISBN 80-05-00633-0.

[12] HAJDUK, M., KONVIČNÝ, J.: Silové podmínky při válcování oceli za tepla. SNTL Praha, 264 p., 1983. DT 621.771.06-18:669.14:539.37l.

[13] SMIRNOV, V. S.: *Teorija prokatki.* Moskva, Metalurgija, 1967.

[14] BURŠA, J.: Prednášky z predmetu Konstitutivní vztahy materiálu [online]. Brno, Vysoké učení technické v Brně, Fakulta strojního inženýrství, Academic year 2019/2020 [Accessed 2020-04-21]. Available from: http://www.old.umt.fme.vutbr.cz/jbursa/Konstitutivni%20modely.7z.

[15] KUBÍK, P.: *Implementace, kalibrace a využití podmínek tvárného lomu v programech MKP.* Brno, 106 p., 2015. Vysoké učení technické v Brně, Fakulta strojního inženýrství. Vedoucí dizertační práce prof. Ing. Jindřich Petruška, CSc.

[16] PETRUŠKA, J.: *Prednášky z predmetu Nelineární úlohy mechaniky v MKP* [online]. Brno, Vysoké učení technické v Brně, Fakulta strojního inženýrství, Academic year 2019/2020 [Accessed 2020-04-20]. Available from: http://www.umt.fme.vutbr.cz/images/opory/Nelinearni20ulohy%20mechaniky %20v%20MKP/RNK.zip.

[17] *Mechanical APDL Theory Reference* [online]. Ansys Inc., 2018 [Accessed 2020-03-15]. Available from: https://www.mm.bme.hu/g̃yebro/files/ans_help_v182/ans_thry/ans_thry.html.

[18] OWEN, D. R. J., HINTON, E.: *Finite Elements in Plasticity.* 1st ed., Pineridge Press Ltd., 450 p., 1980. ISBN 978-0906674055.

[19] STN 41 7246. *Ocel 17 246 Cr-Ni-Ti.* Vydavatelství norem, Praha 10, 8 p., 1991. Triediaci znak: 41 7246.

[20] Murugesan, M., Jung, D. W.: *Johnson Cook Material and Failure Model Parameters Estimation of AISI-1045 Medium Carbon Steel for Metal Forming Applications* [online]. Materials, vol. 12 (4), 18 p. 2019 [Accessed 2020-02-17]. Available from: https://www.mdpi.com/1996-1944/12/4/609.

[21] *Abaqus 6.14 Documentation* [online]. Dassault systèmes, 2014 [Accessed 2020-03-17]. Available from: http://ivt-abaqusdoc.ivt.ntnu.no:2080/tex-is/search/?query=wetting&submit.x=0&submit.y=0&group=bk&CDB=v6.14.

[22] MACURA, P., PETRUŠKA, J.: *Numerical and experimental simulation of pass rolling.* Journal of Materials Processing Technology, vol. 60, pp. 55-60, 1996.

[23] WIERZBICKI T., BAO Y., LEE Y. W., BAI Y.: *Calibration and evaluation of seven fracture models* [online]. International Journal of Mechanical Sciences, pp. 719-743, vol. 47, 2005 [Accessed 2020-04-11]. Available from: https://kundoc.com/pdf-calibration-and-evaluation-of-seven-fracture-models-.html

[24] PETRUŠKA, J.: *MKP v inženýrských výpočtech* [online]. 2011 [Accessed 2020-03-04]. Available from: http://www.umt.fme.vutbr.cz/images/o-pory/MKP%20v%20inzenyrskych%20vypoctech/RIV.pdf.

[25] BOŘKOVEC, J.: *Výpočtová simulace procesu dělení materiálu.* Brno, 2008. 100 p., Vysoké učení technické v Brně, Fakulta strojního inženýrství. Vedoucí disertační práce prof. Ing. Jindřich Petruška, CSc.

[26] HACEK, S.*Využití škálování hmotnosti explicitního řešiče systému Abaqus.* Brno: Vysoké učení technické v Brně, Fakulta strojního inženýrství, 2018. 72 p. Vedoucí bakalářské práce Ing. František Šebek, Ph.D.

[27] SUN, E. Q.: *Shear Locking and Hourglassing in MSC Nastran, ABAQUS, and ANSYS* [online]. pp. 3-4, 2006 [Accessed 2020-03-21]. Available from: https://www.researchgate.net/publication/254384063_Shear_Locking_and_Hourglassing_in_MSC_Nastran_ABAQUS_and_ANSYS.

[28] MILBAUER, M., PERLA, M.:*Fotoelasticimetrie a její použití v praxi.* Prague, Státní nakladatelství technické literatury, 134 p., 1953.

[29] FROCHT, M. M.: Photoelasticity. J. Wiley and Sons, London, 492 p., 1965. ISBN 978-0-08-012998-3.

[30] Polarization [Online]. Baumer sensor technology [Accessed 2020-5-27]. Available from: https://www.baumer.com/ch/en/service-support/know-how/technology-highlights/polarization/a/Polarization.

[31] VASQUEZ–RODRIGUEZ, J. M., FLORES–JOHNSON, E., HERRERA-FRANCO, P., GONZALEZ-CHI, P. I.: *Photoelastic and numerical analyses of the stress distribution around a fiber in a pull-out test for a thermoplastic fiber/epoxy resin composite* [online]. Polymer composites, vol. 39, 2018 [Accessed 2020-05-28]. Available from: https://www.researchgate.net/publication/322129241_Photoelastic_and_numerical_analyses_of_the_stress_distribution_around_a_fiber_in_a_pullout_test_for_a_thermoplastic_fiberepoxy_resin_composite.

[32] DALLY, J.W., RILEY, W.F.: *Experimental Stress Analysis.* 3rd edition, McGraw-Hill Inc., 1991. ISBN 978-0070152182.

[33] MACURA, P.: *Metalurgia i odlevnictvo.* vol. 110, 1987.

List of abbreviations and symbols

Abbreviations

FEM   Finite element method

Symbols

μ_f friction coefficient

μ_b friction coefficient during bite

μ_r friction coefficient during stable rolling

μ_s friction coefficient during stable skidding

S_0 initial cross-sectional area of the workpiece

S_1 final cross-sectional area of the workpiece

v_0 initial velocity of the workpiece

v_1 final velocity of the workpiece

S_1^{gap} cross-sectional area of the workpiece during passage through first rolling gap

S_2^{gap} cross-sectional area of the workpiece during passage through second rolling gap

S_n^{gap} cross-sectional area of the workpiece during passage through n-th rolling gap

v_1^{gap} velocity of the workpiece during passage through first rolling gap

v_2^{gap} velocity of the workpiece during passage through second rolling gap

v_n^{gap} velocity of the workpiece during passage through n-th rolling gap

i forward slip

v_c circumferential velocity of the rolls

$v_{c_1}^{gap}$ circumferential velocity of the rolls during passage through first rolling gap

$v_{c_2}^{gap}$ circumferential velocity of the rolls during passage through second rolling gap

i_1^{gap} orward slip during passage through first rolling gap

i_1^{gap}	orward slip during passage through second rolling gap
L_r	geometric ratio of the deformation zone
l_s	horizontal projection of contact length of the rolls and the workpiece
h_m	mean height of the workpiece in the rolling gap
R_m	effective roll radius
$w_{0_{max}}$	initial height of the workpiece
$w_{1_{max}}$	final height of the workpiece
l_d	deformation zone length
α_0	bite angle
v_m	mean velocity of the workpiece
α_n	neutral angle
l_d^{ext}	extended deformation zone length
Δh	height reduction of the workpiece
dh_0	initial height of elementary layer of material in the deformation zone
dh_1	final height of elementary layer of material in the deformation zone
h_0	initial height of the workpiece
h_1	final height of the workpiece
D_m	effective working diameter
r	radius of roll pass groove
R_k	minimum roll radius
φ_0	angle of oval roll pass groove
α_{0_m}	mean bite angle
F_n	normal force
F_f	frictional force
F_{f_z}	horizontal component of frictional force
F_{n_z}	horizontal component of normal force
F_{n_r}	radial component of normal force

α_{0c}	bite angle at initial point of contact
D	distance between axes of the rolls
R_{c_0}	roll radius at initial point of contact
$\bar{r}$	radius of rounded corner of the workpiece
$\bar{\kappa}$	half of straight workpiece height
$\bar{\xi}$	half of straight workpiece width
z_c	position of initial point of contact in rolling direction
F_w	total force acting on the workpiece in rolling direction
n_c	number of points of contact on both rolls
β	friction angle
$\alpha_{0_{max}}$	maximum bite angle
Δh_{max}	maximum height reduction of the workpiece
R	roll diameter at position of maximum height reduction
F_{roll}	rolling force
q_{lag}	vertical component of deformation resistance on the contact surface of lagging zone
q_{lead}	vertical component of deformation resistance on the contact surface of leading zone
S_{lag}	area of horizontal projections contact surface of lagging zone
S_{lead}	area of horizontal projections of contact surface of leading zone
σ_{nm}	mean natural deformation resistance
$Q_{F_{roll}}$	mean forming factor
S_h	area of horizontal projection of contact surface
T_r	roling temperature
ε	strain
$\dot{\varepsilon}$	strain rate
σ_n	natural deformation resistance
$\bar{\sigma}$	equivalent stress
$K_Q,\ A_Q,\ B_Q,\ C_Q$	empirical correction coefficients of forming factor

101

G	geometric correction coefficient
$\bar{\sigma}$, q_σ	equivalent stress
$\mathbf{S}$	deviatoric stress tensor
S_{ij}	components of deviatoric stress tensor
$\boldsymbol{\sigma}$	stress tensor
σ_{ij}, σ_{11} to σ_{33}	components of stress tensor
σ_h	hydrostatic stress
$\mathbf{I}$	unit matrix
p_σ	pressure
$\sigma_1 \geq \sigma_2 \geq \sigma_3$	principal stresses
r_σ	third invariant of stress tensor
σ_y	yield stress
$\mathrm{d}\varepsilon_{p_{ij}}$	increment of plastic strain
$\mathrm{d}\lambda$	plastic multiplier
Q	plastic potential
E	Young's modulus
ν	Poisson's ratio
σ_{true}	true stress
ε_{true}	true strain
σ_{eng}	engineering stress
ε_{eng}	engineering strain
$\dot{\varepsilon}_p^*$	dimensionless plastic strain rate
T^*	homologous temperature
K^{JC}, C^{JC}, n^{JC}, m^{JC}	Johnson–Cook plasticity parameters
T_{ref}	reference temperature
T_m	melting temperature
$\dot{\bar{\varepsilon}}_p$	equivalent plastic strain rate
$\dot{\bar{\varepsilon}}_{p0}$	reference equivalent plastic strain rate

$\bar{\varepsilon}_p^f$	equivalent plastic strain at fracture
$\bar{\varepsilon}_p$	equivalent plastic strain
$\bar{\varepsilon}_p^{act}$	actual equivalent plastic strain
$\boldsymbol{\varepsilon}_p$	plastic strain tensor
ε_{pij}, ε_{p11} to ε_{p33}	components of plastic strain tensor
$\varepsilon_1 \geq \varepsilon_2 \geq \varepsilon_3$	principal strain
$\bar{\varepsilon}_p^{cum}$	cumulative equivalent plastic strain
$\dot{\boldsymbol{\varepsilon}}_p$	plastic strain rate tensor
t_a	duration of analysis
η	stress triaxiality factor
θ	Lode angle
μ	Lode parameter
ξ	normalized third invariant of stress tensor
$\bar{\theta}$	normalized Lode angle
ω_D	value of damage criterion
$\Delta\omega_D$	incremental increase of value of damage criterion
$\Delta\bar{\varepsilon}_p$	incremental increase of equivalent plastic strain
$\bar{\varepsilon}_f^{pD}$	equivalent plastic strain at fracture for ductile criterion
K_1, K_2	formability coefficients for specific thermodynamical conditions
$\bar{\varepsilon}_f^{pJC}$	equivalent plastic strain at fracture for Johnson–Cook criterion
d_1^{JC} to d_5^{JC}	Johnson–Cook damage parameters
$\bar{\varepsilon}_f^{pXW}$	equivalent plastic strain at fracture for Xue–Wierzbicki criterion
d_1^{XW} to d_5^{XW}	Xue–Wierzbicki damage parameters
Π	potential energy
W	strain energy
$\boldsymbol{\sigma}^{\mathrm{T}}$	stress vector
$\boldsymbol{\varepsilon}^{\mathrm{T}}$	strain vector
P	external load potential

$\mathbf{u}^{\mathrm{T}}$	displacement vector
$\mathbf{o}^{\mathrm{T}}$	body force vector
$\mathbf{p}^{\mathrm{T}}$	surface force vector
$\mathbf{M}$	global mass matrix
$\ddot{\mathbf{U}}$	nodal acceleration matrix
$\mathbf{B}$	global damping matrix
$\dot{\mathbf{U}}$	nodal velocity matrix
$\mathbf{F}_t^{int}$	internal forces matrix
$\mathbf{F}_t^{ext}$	external forces matrix
$\dot{\mathbf{U}}_{t+\frac{\Delta t}{2}}$	nodal velocity matrix at $t + \frac{\Delta t}{2}$
$\dot{\mathbf{U}}_{t-\frac{\Delta t}{2}}$	nodal velocity matrix at $t - \frac{\Delta t}{2}$
$\ddot{\mathbf{U}}_t$	nodal acceleration matrix at t
$\mathbf{U}_{t+\Delta t}$	nodal displacement matrix at $t + \Delta t$
$\mathbf{U}_t$	nodal displacement matrix at t
$\mathbf{U}_{t+\frac{\Delta t}{2}}$	nodal displacement matrix at $t + \frac{\Delta t}{2}$
$X_{t+\Delta t}$	geometry at $t + \Delta t$
X_t	geometry at t
Δt	time step length
Δt^{crit}	critical time step length
ω_{max}	maximum eigenfrequency of the smallest element of the model
l_{char}	characteristic dimension of the smallest element of the model
c_v	velocity of stress wave propagation throughout the material
l_e	average element length in rolling direction
R_{feed}	feed rate
n_n	umber of nodes in cross section of the workpiece
Δ	relative phase retardation
t_{spec}	thickness of the specimen
λ	vacuum wavelength

C_{opt}	stress–optic coefficient
n_1	RPM of first roll pass
ω_1	angular velocity of first roll pass
ω_2	angular velocity of second roll pass
$R_{p0,2}$	proof strength at 0,2 % of plastic strain
ε_t	total strain
ε_e	elastic strain
u_1	displacement of first roll pass
u_2	displacement of second roll pass

List of attachments

A Finite element models used in the thesis

Following computational models may be found in the attachments:

- DP_full_model.cae - full model.

- DP_sequential_model.cae - sequential simplified model.

- DP_separate_model.cae - separate simplified model. Only contains analysis of passage through the second roll pass, as the first is the same as the one included in previous model.

These models were created in Abaqus/CAE 2019, which is also required in order to run them. Result files are not included due to excessive size, but may be obtained by running the analyses with enclosed models.